Frank Ellinghaus

# Beam–Charge and Beam–Spin Azimuthal Asymmetries in Deeply–Virtual Compton Scattering

– November 2003 –

# Beam–Charge and Beam–Spin Azimuthal Asymmetries in Deeply–Virtual Compton Scattering

**D I S S E R T A T I O N**

zur Erlangung des akademischen Grades

**d o c t o r  r e r u m  n a t u r a l i u m**

**(Dr. rer. nat.)**

im Fach Physik

eingereicht an der

**Mathematisch-Naturwissenschaftlichen Fakultät I**

**der Humboldt-Universität zu Berlin**

von


Diplom–Physiker

**Frank Ellinghaus**

geboren am 15. Juni 1973 in Borghorst


**Präsident der Humboldt-Universität zu Berlin**
**Prof. Dr. Jürgen Mlynek**

**Dekan der Mathematisch-Naturwissenschaftlichen Fakultät I**
**Prof. Dr. Michael W. Linscheid**

Gutachter:

1. Prof. Dr. Thomas Lohse
2. Prof. Dr. Hermann Kolanoski
3. Prof. Dr. Dirk Ryckbosch

Tag der mündlichen Prüfung:

22. Januar 2004

# Kurzfassung

Die Untersuchung der Spinstruktur des Nukleons ist das wesentliche Anliegen der HERMES Kollaboration. Der Spin des Nukleons sollte sich aus den Beiträgen seiner Konstituenten, der Quarks und der Gluonen, ergeben. Die bisherigen Messungen zeigen, daß der Spin der Valenz– und Seequarks höchstens 30% des Spins des Nukleons ausmacht. Demnach sollte der Bahndrehimpuls der Quarks und der Gesamtdrehimpuls der Gluonen für den fehlenden Anteil verantwortlich sein. Die einzige bekannte Möglichkeit zur Bestimmung der Einzelbeiträge beruht auf den sogenannten generalisierten Partonverteilungen, einem neuen Formalismus zur Beschreibung der Struktur des Nukleons. Vom theoretischen Standpunkt aus können diese am einfachsten durch die tief–virtuelle Comptonstreuung, d.h. durch die Messung der harten exklusiven Produktion von Photonen mittels eines Leptonenstrahls, zugänglich gemacht werden. Dieser Prozeß hat den gleichen Endzustand wie der Bethe–Heitler Prozeß, in dem ein hartes Bremsstrahlungsphoton vom Elektron emittiert wird. Der durch die quantenmechanische Interferenz dieser Prozesse auftretende Anteil am Wirkungsquerschnitt der Photonenproduktion ermöglicht die Messung der Streuamplituden der tief–virtuellen Comptonstreuung. Azimutale Asymmetrien, die aus Messungen mit unterschiedlicher Ladung bzw. mit unterschiedlichem Spin des Leptons gebildet werden können, sind in der Lage diesen Interferenzanteil herauszufiltern und somit die realen und imaginären Anteile der Streuamplituden zu ermitteln.

Die vorliegende Arbeit beschreibt die Messung dieser azimutalen Ladungs– und Strahlspinasymmetrien in der tief–virtuellen Comptonstreuung am Proton. Die Daten wurden mit dem HERMES Experiment bei HERA durch Streuung eines longitudinal polarisierten Positronen– bzw. Elektronenstrahls mit einer Energie von 27.6 GeV an einem unpolarisierten Wasserstoff–Gastarget genommen. Erstmalig wurden alle relevanten Momente der azimutalen Abhängigkeiten beider Asymmetrien, inklusive Beiträgen von höherem Twist, als Funktion der kinematischen Variablen $x_B$, $Q^2$ und $t$ extrahiert. Das führende Moment der Strahlspinasymmetrie, integriert über den gesamten kinematischen Bereich, stimmt gut mit zwei früheren Messungen bei HERMES und bei CLAS am Jefferson Lab überein. Die Messung der Ladungsasymmetrie ist weltweit einzigartig. Der Vergleich der extrahierten Momente mit den Vorhersagen theoretischer Modelle für die generalisierten Partonverteilungen zeigt, daß die Modelle das Vorzeichen, die Größe und das Verhalten der Asymmetrien bezüglich der kinematischen Variablen gut beschreiben. Es ist zudem möglich, erste Bereiche für die Modellparameter zu favorisieren.

# Contents

# Chapter 1

# Introduction

Since more than 40 years the structure of the nucleon is being studied by means of electron scattering experiments. Elastic scattering off protons by Hofstadter and McAllister [Hof55] revealed the extended structure of the proton that is described by form factors. Deeply–inelastic scattering provided the first indication of the point–like constituents in the nucleon. The longitudinal momentum distribution of these constituents (partons) is encoded in phenomenological parton distribution functions. Hard exclusive scattering is described by the concept of generalized parton distributions that combines and generalizes the concepts of form factors and ordinary parton distributions. It simultaneously describes (transverse) position distributions and (longitudinal) momentum distributions of partons.

The motivation to study generalized parton distributions [Dit88, Mül94] was strongly enhanced by the finding that they offer, for the first time, a possibility to determine the total angular momentum of quarks $J^Q$ in the nucleon [Ji97a]. The total angular momentum of the nucleon can be decomposed as

$$\frac{1}{2} = \underbrace{\frac{1}{2}\,\Delta\Sigma + L^Q}_{J^Q} + J^G,$$

whereby the HERMES experiment at DESY was designed to study the contributions of the different valence and sea quark flavors [Air03a, Air03b] to the spin contribution from the quarks $\Delta\Sigma$. Since the results from the European Muon Collaboration [Ash88] implied that the latter is smaller than about 30%, one of the most exciting quests in hadronic physics is to understand how the remaining contribution is distributed among the orbital angular momentum of the quarks $L^Q$ and the total angular momentum of the gluons $J^G$. The only known way to answer this is to use the knowledge on $\Delta\Sigma$ and to determine $J^Q$ in the framework of generalized parton distributions.

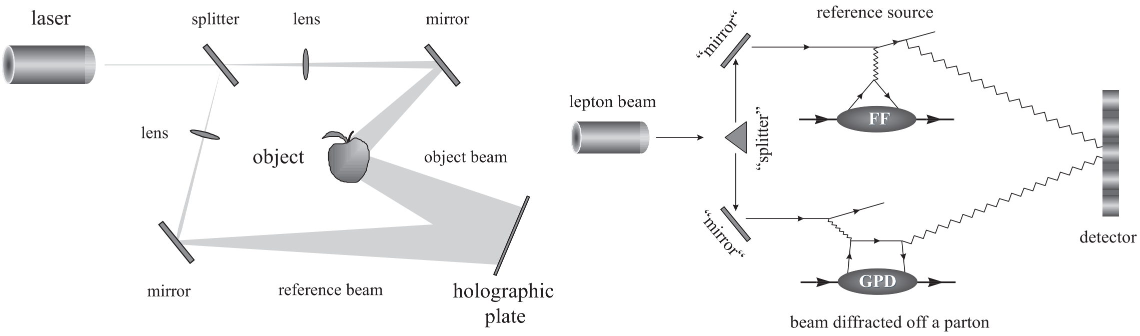


**Figure 1.1:** Left panel: Conventional holography. Right panel: "Nucleon holography" via the interference of the deeply–virtual Compton scattering (lower graph) and the Bethe–Heitler process (upper graph). Figure taken from reference [Bel02b].

---

The theoretically cleanest way to access generalized parton distributions appears to be the **D**eeply–**V**irtual **C**ompton **S**cattering (DVCS) process, i.e., the hard exclusive leptoproduction of real photons. Since generalized parton distributions carry information about longitudinal and transverse degrees of freedom, the DVCS amplitudes need to be known completely, i.e., by magnitude and phase. This is possible through a measurement of the interference between the DVCS and the Bethe–Heitler process as sketched in the right panel of figure 1.1. The photon is radiated from a parton in the former and from the electron in the latter process. The Bethe–Heitler amplitude is exactly calculable using the knowledge of the proton form factors measured in elastic scattering. It acts as a reference, analogous to the reference laser beam in the process of taking a holographic picture, as shown in the left panel of the figure. The laser beam is split into the reference beam and the one that scatters from the object. Similarly, the lepton beam inherently "splits up" into two "beams" of photons corresponding to the two contributions to the exclusive production of a real photon. Their interference has the potential to reveal the three–dimensional structure of the nucleon at the parton level.

In order to isolate the real part of the interference term in a measurement, lepton beams of both charges are needed [Bro72]. The imaginary part can be accessed by measuring the angular dependence of the produced photon if polarized lepton beams are available [Kro96]. A determination of all relevant moments of the angular dependence in beam–charge and beam–spin asymmetry measurements allows to access leading and non–leading DVCS amplitudes and consequently leading and non–leading GPDs.

The HERA electron/positron–proton collider at DESY offers polarized lepton beams of both charges. The analysis described in detail in this thesis is based on data taken by the HERMES Collaboration. A polarized electron beam in 1998 and a polarized positron beam in 2000 were scattered off an unpolarized gaseous hydrogen target. The results represent the first extraction of all relevant moments of beam–charge and beam–spin asymmetries in dependence on their kinematic variables.

The outline is as follows. The theoretical framework of generalized parton distributions and the way to access them via DVCS is given in the next two chapters. Chapter 4 describes the HERMES experiment, focusing on the parts needed for this analysis. The selection criteria and corrections applied to the HERMES data taken in 1998 and 2000 are explained in chapter 5, followed by the Monte–Carlo studies concerning resolution and background in chapter 6. The extraction of the azimuthal asymmetries and the determination of the corresponding uncertainties is described in chapter 7, the results are shown in chapter 8. Model calculations based on a model described in chapter 2 were carried out and used to interpret the results in chapter 9. The thesis is concluded by a summary and an outlook.

# Chapter 2

# Generalized Parton Distributions

Hard scattering processes, such as inclusive **D**eeply–**I**nelastic **S**cattering (DIS), semi-inclusive DIS and hard exclusive scattering have an important property in common, namely the possibility to separate the hard scattering parts, which are exactly calculable in **p**erturbative **Q**uantum **C**hromo**d**ynamics (pQCD), from the non–perturbative soft parts. This factorization property is well established in the case of inclusive and semi-inclusive DIS and has been extensively used to investigate the structure of the nucleon. Only a few years ago, factorization theorems for exclusive reactions

$$\gamma^*(q) + T(p) \to C(q') + T'(p'), \tag{2.1}$$

in which a virtual photon $\gamma^*$ with four–momentum $q$ scatters off the hadronic target $T$ with four–momentum $p$, have been proven in the case of the produced particle $C$ being a meson [Col97] or a real or timelike photon [Rad97, Ji98a, Col99]. Note that the proofs are valid only for large photon virtualities $Q^2 \equiv -q^2$ compared to the mass of the final hadronic state $T'$ and for longitudinal virtual photons in the case of meson production. Similar to the case of inclusive and semi-inclusive DIS, where the nucleon structure is encoded in the **P**arton **D**istribution **F**unctions (PDFs), hard exclusive reactions can be described in terms of **G**eneralized **P**arton **D**istributions (GPDs). The ordinary PDFs and nucleon form factors turn out to be the limiting cases and moments of GPDs, respectively. Although GPDs have been known for a while [Dit88, Mül94], strong interest was created only after the finding by Ji [Ji97a] that the GPDs offer for the first time a possibility to determine the total angular momentum carried by the quarks in the nucleon. In addition, information about the distribution of energy, momentum and pressure in nucleons and nuclei becomes accessible [Pol03]. Details on the aforementioned properties of GPDs are given in the next section. The recent theoretical ideas about the potential of GPDs to study the three–dimensional structure of hadrons were already sketched in the

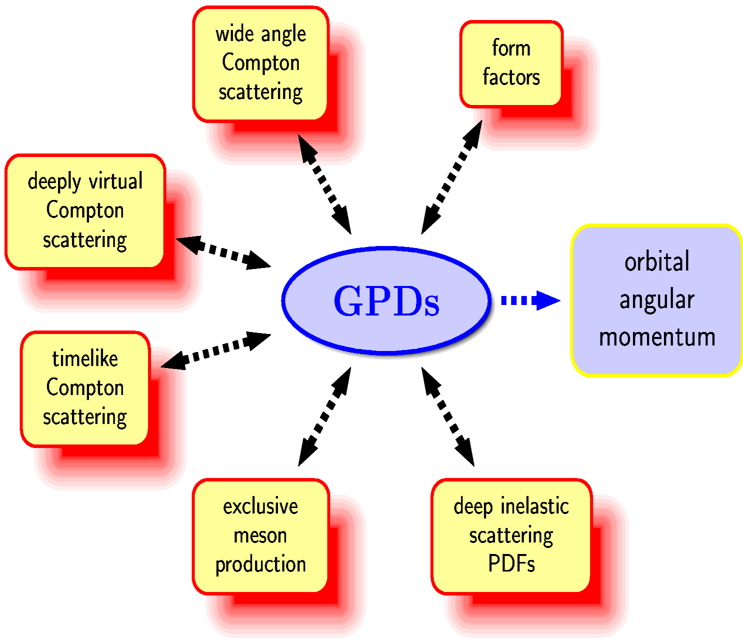


**Figure 2.1:** Schematic overview of some reactions and nucleon properties related to GPDs. Figure taken from reference [GPD01].

---

introduction. More information can be obtained from the initial work [Bur00] and references [Die02, Ral02, Bur03].

Although not complete, the schematic overview in figure 2.1 visualizes the central role GPDs are playing in nucleon structure studies and it shows the exclusive processes which can be described in terms of GPDs. Measurements of these processes will facilitate to access them. The process of **D**eeply–**V**irtual **C**ompton **S**cattering (DVCS), where the produced particle is a real photon (see left panel of figure 2.2), appears to be the theoretically cleanest process to be interpreted in terms of GPDs since it involves only a single hadron. In contrast, exclusive meson production (right panel of figure 2.2) needs further non–perturbative information due to the involved distribution amplitude $\Phi(z)$. The process of timelike Compton scattering [Ber02], i.e., the production of a virtual photon which eventually converts into a lepton–antilepton pair, is suppressed by $\alpha_{em}^2$ compared to the DVCS process. It is therefore experimentally difficult to access. Wide–Angle Compton Scattering is a process where the initial and final photons are real and the involved momentum transfer is large [Rad98].

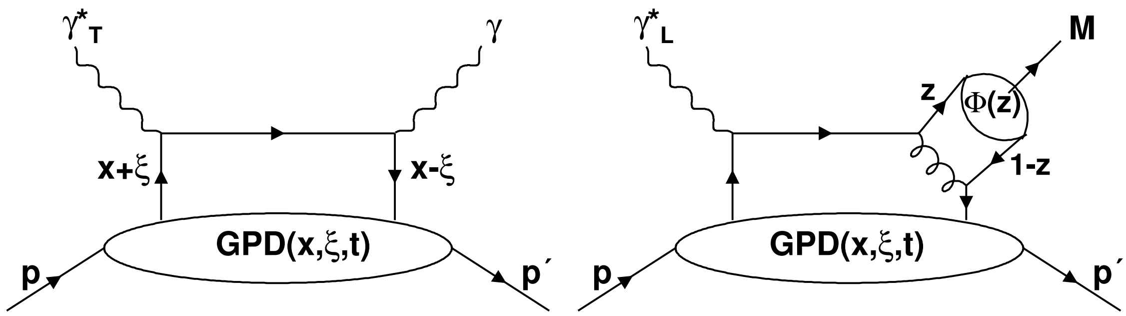


**Figure 2.2:** Leading diagrams for DVCS (left panel) and for meson production (right panel). The variables are explained in section 2.1.

## 2.1 Properties of Generalized Parton Distributions

After the first investigation of GPDs [Dit88, Mül94], they were introduced in two slightly different versions as **O**ff–**F**orward **P**arton **D**istributions (OFPDs) by Ji [Ji97a, Ji97b] and **N**on–**F**orward **P**arton **D**istributions (NFPDs) by Radyushkin [Rad96b, Rad97]. The names OFPDs and NFPDs highlight the main difference between the ordinary PDFs describing expectation values of quark or gluon operators for a hadron state in forward kinematics and the OFPDs and NFPDs describing the extension to off–forward or non–forward kinematics. The term forward (off–forward or non–forward) refers to the diagonal (off–diagonal or non–diagonal) matrix elements in the transition matrix between the initial and the final hadronic state. As an example the leading diagram for the DVCS process, the so–called handbag diagram, is sketched in the left panel of figure 2.2. The initial and final proton have different momenta and thus the lower blob, representing the structure of the nucleon, can be described in off-forward/non–forward kinematics only. On the other hand, the more recent name GPDs takes into account that in the limit of vanishing momentum difference between the initial and final proton the GPDs reduce to the usual PDFs and therefore they are a generalization of PDFs.

For OFPDs (NFPDs) different nomenclatures are used, whereby both depend on the longitudinal momentum fractions $x$ $(X)$ and $\xi$ $(\zeta)$ in a frame where the initial and final proton move fast, and on the Mandelstam variable $t = (p - p')^2$. The latter is also related to the transverse momentum transfer. In addition, GPDs are, just like PDFs, subject to QCD evolution and thus depend on $Q^2$. Since the evolution has been calculated perturbatively in leading order [Mül94, Ji97b, Rad97, Blü99] and next–to leading order [Bel99, Bel00a, Bel00b] in the strong coupling constant $\alpha_s$, the explicit $Q^2$ dependence will be omitted in the following.

In a partonic interpretation of OFPDs (see left panel of figure 2.2), a parton with longitudinal momentum fraction $x+\xi$ is removed from the proton and is put back with a longitudinal momentum fraction $x-\xi$. Note that with $x$ defined in the range $[-1,1]$, the longitudinal momentum fractions $x+\xi$ and $x-\xi$ can be either positive or negative corresponding to the active parton being particle or antiparticle, respectively. In the NFPD definition a parton with longitudinal momentum fraction $X$ is removed from the proton and is put back with a longitudinal momentum fraction $X-\zeta$. In other words, in the OFPD (NFPD) definition $x$ ($X$) is the average (initial) longitudinal momentum fraction of the involved parton. In the OFPD definition the so–called skewedness parameter $\xi$ is related to $x_B$, the momentum fraction of the proton carried by the struck quark, as

$$\xi \approx \frac{x_B}{2-x_B} \tag{2.2}$$

in the kinematic limit (Bjorken limit) of large photon virtuality and energy with $x_B$ (see equation 3.3) being fixed. The OFPD definition will be used in the following under the common name GPDs. Note that the term **S**kewed **P**arton **D**istributions (SPDs) instead of GPDs appears in the literature as well.

At leading twist[1] (twist–2), the quark and gluon structure of the nucleon can be parametrized in terms of eight quark GPDs for each quark flavor $q$ and eight gluon GPDs, respectively. Four of the eight conserve parton helicity and four do not (helicity–flip). The parton helicity conserving ones are the unpolarized GPDs $H(x,\xi,t)$ and $E(x,\xi,t)$ and the polarized GPDs $\tilde{H}(x,\xi,t)$ and $\tilde{E}(x,\xi,t)$. The GPDs $H(x,\xi,t)$ and $\tilde{H}(x,\xi,t)$ conserve nucleon helicity while $E(x,\xi,t)$ and $\tilde{E}(x,\xi,t)$ do not. The four parton helicity–flip GPDs are denoted by $H_T(x,\xi,t)$, $E_T(x,\xi,t)$, $\tilde{H}_T(x,\xi,t)$ and $\tilde{E}_T(x,\xi,t)$. The latter two do not vanish due to time reversal invariance [Die01] as previously assumed [Hoo98].

### 2.1.1 Limits and Moments of Generalized Parton Distributions

In the limit of vanishing four–momentum transfer squared ($t\to 0$) between initial and final hadronic state (forward limit), the quark helicity conserving GPDs

[1] An exact definition of twist can be found in reference [Jaf96]. For practical use it is sufficient to say that effects labeled with twist–$h$ never enter hard processes with suppression less than $(M/Q)^{h-2}$, with $M$ being the hadronic mass.

$H^q(x,\xi,t)$ and $\tilde{H}^q(x,\xi,t)$ reduce to the well–known quark distributions $q(x)$ and helicity distributions $\Delta q(x)$:

$$H^q(x,0,0) = q(x), \quad \tilde{H}^q(x,0,0) = \Delta q(x). \tag{2.3}$$

Note that in the limit $t \to 0$ also $\xi$ goes to zero. The GPDs $E^q(x,\xi,t)$ and $\tilde{E}^q(x,\xi,t)$, which do not conserve nucleon helicity, are inaccessible in the forward limit and thus are not related to ordinary PDFs. Among the four helicity–flip quark GPDs only $H_T^q(x,\xi,t)$ is measurable in the forward limit. It reduces to the quark transversity distribution $\delta q(x)$. Besides for this special case, no process is known to date to access the helicity–flip quark GPDs and therefore they will not be discussed further.

In analogy to the helicity conserving quark GPDs, the helicity conserving gluon GPDs $E^g(x,\xi,t)$ and $\tilde{E}^g(x,\xi,t)$ are inaccessible in the forward limit while $H^g(x,\xi,t)$ and $\tilde{H}^g(x,\xi,t)$ reduce to the unpolarized and polarized gluon distributions $G(x)$ and $\Delta G(x)$, respectively. None of the helicity–flip gluon GPDs can be measured in the forward limit. This offers a unique opportunity to investigate the helicity–flip gluon distribution in a nucleon, i.e., in a spin 1/2 target, since in ordinary PDFs a gluon helicity–flip can only occur if the target can compensate the helicity change of two units, i.e., the target has a spin of at least one. In the case of GPDs the target can have less than spin one since transfer of transverse momentum and thus of orbital angular momentum is permitted.

The first moments of the helicity conserving quark GPDs are related to the elastic form factors of the nucleon through the sum rules [Ji97a]

$$\begin{aligned}
\int_{-1}^{1} dx\, H^q(x,\xi,t) &= F_1^q(t), & \int_{-1}^{1} dx\, E^q(x,\xi,t) &= F_2^q(t), \\
\int_{-1}^{1} dx\, \tilde{H}^q(x,\xi,t) &= G_A^q(t), & \int_{-1}^{1} dx\, \tilde{E}^q(x,\xi,t) &= G_P^q(t),
\end{aligned} \tag{2.4}$$

where $F_1^q(t)$ and $F_2^q(t)$ are the elastic Dirac and Pauli form factors and $G_A^q(t)$ and $G_P^q(t)$ are the axial–vector and pseudo–scalar form factors for the quark flavor $q$ in the nucleon.

While form factors and PDFs can be measured in non–exclusive reactions, no possibility was known until recently to access the total angular momentum $J^Q$ carried by the quarks in the nucleon. Ji's relation [Ji97a] connects the second moment of the sum of the unpolarized quark GPDs $H^q(x,\xi,t)$ and $E^q(x,\xi,t)$ in the limit of vanishing four–momentum transfer to the angular momentum $J^q$ of the quark species $q$:

$$J^q = \lim_{t\to 0} \frac{1}{2} \int_{-1}^{1} dx\, x\, [H^q(x,\xi,t) + E^q(x,\xi,t)]. \tag{2.5}$$

Note that the dependence on $\xi$ disappears in the limit $t \to 0$. The sum of the contributions $J^q$ from all quark flavors gives the total quark angular momentum $J^Q = \sum_q J^q$ which decomposes as

$$J^Q = \frac{1}{2}\,\Delta\Sigma + L^Q, \tag{2.6}$$

where $\Delta\Sigma/2$ and $L^Q$ are the quark spin and orbital angular momentum contributions, respectively. Using the information on $\Delta\Sigma$ available from inclusive and semi–inclusive polarized DIS, the contribution $L^Q$ can be derived, in principle. Since no other way is known at present to determine $L^Q$, it is the main driving force for studying GPDs and therefore highlighted in figure 2.1.

Ji's relation is valid for gluons as well. With the total angular momentum of the gluons

$$J^G = \lim_{t\to 0} \frac{1}{2} \int_{-1}^{1} dx\, x\, [H^g(x,\xi,t) + E^g(x,\xi,t)], \tag{2.7}$$

the spin of the nucleon is given by the gauge invariant sum

$$\frac{1}{2} = J^Q + J^G. \tag{2.8}$$

This, on the other hand, implies that a measurement of the total angular momentum of the quarks also reveals the total angular momentum of the gluons.

### 2.1.2 The D–Term

An important property of the $t$–independent part of GPDs is the polynomiality condition of their Mellin moments following from Lorentz invariance [Ji97a, Ji97b]

$$\int_{-1}^{1} dx\, x^N\, H^q(x,\xi) = h_0^{q(N)} + h_2^{q(N)}\,\xi^2 + \cdots + h_{N+1}^{q(N)}\,\xi^{N+1}, \tag{2.9}$$

$$\int_{-1}^{1} dx\, x^N\, E^q(x,\xi) = e_0^{q(N)} + e_2^{q(N)}\,\xi^2 + \cdots + e_{N+1}^{q(N)}\,\xi^{N+1}, \tag{2.10}$$

where the corresponding polynomials contain only even powers of the parameter $\xi$ due to time reversal invariance [Man98a, Ji98b]. This implies that for even $N$ the highest power of $\xi$ is still $N$ and not $N+1$ as in the case of $N$ being odd. For the latter case, the coefficients in front of the highest power of $\xi$ are related to each other [Ji98b]

$$e^{q(N)}_{N+1} = -h^{q(N)}_{N+1}, \tag{2.11}$$

i.e., the functional relations between $H^q(x,\xi)$ and $E^q(x,\xi)$ are non–trivial. A way to parametrize GPDs whereby satisfying the polynomiality condition is to use the so–called **D**ouble **D**istribution (DD) formalism [Rad96a]. The $t$–independent part of the GPDs is then given as

$$H^q_{DD}(x,\xi) = \int\limits_{-1}^{1} d\beta \int\limits_{-1+|\beta|}^{1-|\beta|} d\alpha\, \delta(x-\beta-\alpha\,\xi)\, F^q(\beta,\alpha), \tag{2.12}$$

$$E^q_{DD}(x,\xi) = \int\limits_{-1}^{1} d\beta \int\limits_{-1+|\beta|}^{1-|\beta|} d\alpha\, \delta(x-\beta-\alpha\,\xi)\, K^q(\beta,\alpha), \tag{2.13}$$

with $F^q(\beta,\alpha)$ and $K^q(\beta,\alpha)$ being the actual double distributions discussed further in section 2.2.1. It was recognized that this parametrization was not complete, since the polynomiality condition was satisfied but always lead to $h^{q(N)}_{N+1} = e^{q(N)}_{N+1} = 0$, i.e., the highest power of $\xi$ was absent for odd $N$. Thus the parametrization was completed by adding the so–called D-term introduced by Polyakov and Weiss [Pol99]:

$$H^q(x,\xi) = H^q_{DD}(x,\xi) + \theta[1-\frac{x^2}{\xi^2}]\, D^q(\frac{x}{\xi}), \tag{2.14}$$

$$E^q(x,\xi) = E^q_{DD}(x,\xi) - \theta[1-\frac{x^2}{\xi^2}]\, D^q(\frac{x}{\xi}). \tag{2.15}$$

The D-term now generates the highest power of $\xi$:

$$\int\limits_{-1}^{1} dz\, z^N\, D^q(z) = h^{q(N)}_{N+1} = -e^{q(N)}_{N+1}. \tag{2.16}$$

Note that for the polarized GPDs $\tilde{H}^q(x,\xi)$ and $\tilde{E}^q(x,\xi)$ the polynomiality conditions are similar to those for the unpolarized ones $H^q(x,\xi)$ and $E^q(x,\xi)$. The difference is that the highest power of the polynomial in $\xi$ for odd $N$ (even $N$) is $N-1$ ($N$). Therefore the D-term is not required for the polarized GPDs.

Although at first glance the D-term looks like an additional term to just complete the parametrization, it seems to have its own physics meaning and relations to fundamental observables. Since the absolute value of the D-term is the same for both unpolarized GPDs, but contributing with opposite signs, it drops out of Ji's relation given in equation 2.5. However, rewriting the relation in an equivalent way and again going to the limit $t \to 0$ leads to [Ji97c]:

$$\int_{-1}^{1} dx\, x \sum_q H^q(x,\xi,t) = M_2^Q + \frac{4}{5}\, d_1^Q\, \xi^2, \tag{2.17}$$

$$\int_{-1}^{1} dx\, x \sum_q E^q(x,\xi,t) = (2J^Q - M_2^Q) - \frac{4}{5}\, d_1^Q\, \xi^2. \tag{2.18}$$

Here $d_1^Q$ is the first coefficient in an expansion of the D-term shown later in equation 2.32 and $M_2^Q$ is the momentum fraction carried by all quarks and antiquarks in the nucleon:

$$M_2^Q = \sum_q \int_0^1 dx\, x\, (q(x) + \overline{q}(x)). \tag{2.19}$$

Analogous expressions are valid for the gluon GPDs as well. With $M_2^Q$ ($M_2^G$) and $J^Q$ ($J^G$) being the total momentum and total angular momentum of the quarks (gluons) in the nucleon, respectively, the gauge invariant sum $M_2^Q + M_2^G = 1$ exists in addition to equation 2.8. Moreover, with the first coefficient of the gluon D-term $d_1^G$ the sum $d_1^Q + d_1^G = d$ is scale independent. The constant d can be represented in the form [Pol02]

$$d = \frac{5}{9}\, m_N \int d^3r\, r^2\, p(r), \tag{2.20}$$

with the nucleon mass $m_N$. The function $p(r)$ can be interpreted as the radial distribution of pressure inside the nucleon. In other words, the spatial distribution of forces experienced by a parton inside the nucleon can be studied for the first time. The constant $d$ is as fundamental as other conserved characteristics of the nucleon, such as the total momentum or total angular momentum, but it is inaccessible in usual DIS. Thus, in the limit of zero momentum transfer, three basic static mechanical properties of a composite system, the nucleon, can in principle be studied via exclusive reactions. A first approach to extend this picture to the case of nuclei, i.e., access to the $A$–dependence of the forces experienced by quarks and gluons, is described in reference [Pol03].

## 2.2 Parametrization of Generalized Parton Distributions

In order to use the GPD formalism to predict the size of observables measurable in hard exclusive reactions, GPDs have to be modeled ensuring the relations to the

PDFs and the form factors as described in section 2.1.1. One way GPDs have been modeled is a direct calculation based on specific dynamic models, e.g., the MIT–Bag model [Ji97c] and the chiral quark–soliton model [Pet98]. The other approach is a direct phenomenological parametrization without or with only little underlying theory of the structure of the nucleon. Recent parametrizations are usually done the latter way. The description of one of these will be given here, following the model developed in references [Van99, Kiv01a, Goe01] unless otherwise noted. The underlying computer code was made available [Van01] and is used for a comparison between model calculations and the results of this analysis in chapter 9. Only the parametrization of the GPD $H^q(x,\xi,t)$ and the D–term will be described since it will be shown in section 3.3.4 that the main contribution to the observables this analysis is focused on stems from the GPD $H^q(x,\xi,t)$.

### 2.2.1 Parametrization of the GPD $H^q(x,\xi,t)$

It has been shown (see equation 2.14) that the $t$–independent part of the GPD $H^q(x,\xi,t)$ can be parametrized using the double distribution formalism completed by the D-term. The parametrization of the double distribution part of the GPD $H^q(x,\xi,t)$ is given in equation 2.12, whereby a model for the double distribution $F^q(\beta,\alpha)$ is proposed in references [Rad99a, Rad99b]:

$$F^q(\beta,\alpha) = h(\beta,\alpha)\, q(\beta). \tag{2.21}$$

Here $q(\beta)$ is the forward quark distribution for the flavor $q$ and $h(\beta,\alpha)$ is the so–called profile function. A general ansatz for the profile function is given through [Rad01]

$$h(\beta,\alpha) = \frac{\Gamma(2\,b+2)}{2^{2\,b+1}\,\Gamma^2(b+1)} \frac{[(1-|\beta|)^2-\alpha^2]^b}{(1-|\beta|)^{2\,b+1}}. \tag{2.22}$$

The parameter $b$ characterizes how strong the GPD depends on the skewedness $\xi$. In the limit $b\to\infty$ the GPD is independent of $\xi$, i.e., $H(x,\xi)=q(x)$. Note that $b$ is a free parameter for the valence quarks ($b_{val}$) or the sea quarks ($b_{sea}$) and thus can be used as a fit parameter in the extraction of GPDs from hard electroproduction data.

The double distribution part of the $u$–quark GPD $H^u$ is shown in figure 2.3 for different values of $\xi$. The parameter $b$ is set to $b_{val}=b_{sea}=1$. To ensure the correct forward limit, the forward quark distribution $q(\beta)$ in equation 2.21 was chosen according to the next–to leading order quark distributions of Martin et al. [Mar98] (MRST98 parametrization). As negative values of $x$ at $\xi=0$ correspond to antiquarks, the thin solid lines in figure 2.3 show the forward $u$–quark distributions

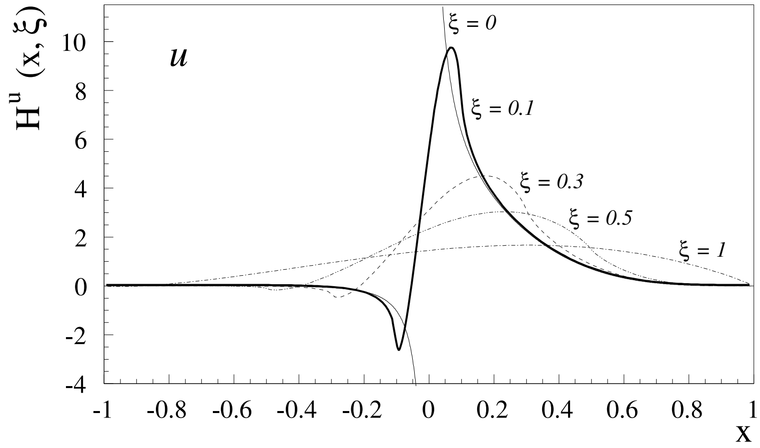


**Figure 2.3:** Double distribution part to the $u$–quark GPD $H^u(x,\xi)$ for different values of $\xi$ and $b_{val} = b_{sea} = 1$. The thin solid lines ($\xi = 0$) show the ordinary forward $u$–quark distributions (MRST98 parametrization at $Q^2 = 2$ GeV$^2$). Figure taken from reference [Goe01].

---

for quarks ($x > 0$) and antiquarks ($x < 0$). Figure 2.4 shows, at a fixed value of $\xi$, the dependence of the double distribution part to the GPD $H^u$ on the parameters $b_{val}$ and $b_{sea}$. In the limit $b_{val} = b_{sea} = \infty$ one finds back the forward $u$–quark distribution.

The $t$–dependence of the GPD $H^q$ is mainly constrained by its relation to the Dirac form factor $F_1^q$ according to the first sum rule in equation 2.4. Note that the form factor in this sum rule is understood to be the one of the proton, e.g., $F_1^u(t) \equiv F_1^{u/p}(t)$. In this notation, the $u$–quark ($d$-quark) form factor is normalized at $t = 0$ as $F_1^u(0) = 2$ ($F_1^d(0) = 1$) in order to yield the normalization of 2 (1) for the respective quark distribution in the nucleon. The elastic form factor for a particular quark is then related to the nucleon form factors as:

$$F_1^{u/p} = 2\,F_1^p + F_1^n + F_1^s, \tag{2.23}$$
$$F_1^{d/p} = 2\,F_1^n + F_1^p + F_1^s, \tag{2.24}$$

where $F_1^p$ and $F_1^n$ are the proton and neutron electromagnetic form factors, respectively, with $F_1^p(0) = 1$ and $F_1^n(0) = 0$. The strangeness form factor of the nucleon $F_1^s$ is set to zero since it is not well known but expected to be small. The simplest parametrization for the $t$–dependence of the quark GPDs which satisfies the sum rules and yields the correct forward limit is therefore the factorized ansatz for the

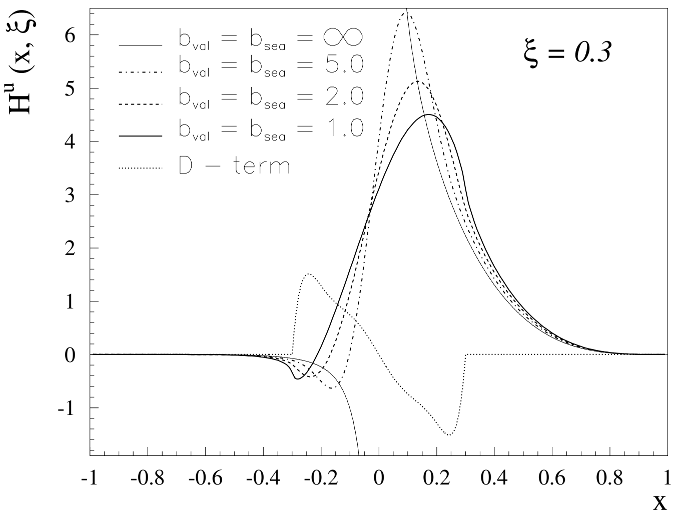


**Figure 2.4:** Double distribution part to the GPD $H^u(x, \xi)$ at $\xi = 0.3$ for different values of the parameters $b_{val}$ and $b_{sea}$. In the limit $b_{val} = b_{sea} = \infty$ (thin solid lines) one finds back the forward $u$–quark distribution. The D–term contribution to $H^u(x, \xi)$ is shown by the dotted curve and must be added to the double distribution part to obtain the total GPD $H^u(x, \xi)$. Figure taken from reference [Goe01].

---

$t$–dependence

$$H^u(x, \xi, t) = H^u(x, \xi)\, F_1^u(t)/2, \tag{2.25}$$
$$H^d(x, \xi, t) = H^d(x, \xi)\, F_1^d(t), \tag{2.26}$$
$$H^s(x, \xi, t) = 0. \tag{2.27}$$

The sum rules in equation 2.4 constrain only the valence quarks and thus a different $t$–dependence for the sea quark contributions could be used. However, since other information is absent, the same ansatz is used for sea quarks.

A more sophisticated ansatz is the Regge–motivated one

$$H^q(x, \xi = 0, t) = \frac{1}{x^{\alpha' t}}\, q(x), \tag{2.28}$$

which yields the correct forward limit as well. Here $\alpha'$ can be interpreted as the slope of a Regge trajectory. In addition, it was shown that using the above ansatz in the first sum rule of equation 2.4,

$$F_1^q(t) = \int_0^1 dx\, \frac{1}{x^{\alpha' t}}\, q_{val}(x), \tag{2.29}$$

a satisfactory description of the proton Dirac form factor is achieved over the range of interest ($0 < -t < 1$ GeV$^2$) with $\alpha' = 0.8$ GeV$^{-2}$. To incorporate a $\xi$–dependence in the Regge ansatz of equation 2.28, the model for the double distribution in equation 2.21 can be modified in the following way:

$$F^q(\beta, \alpha, t) = h(\beta, \alpha)\, q(\beta)\, \frac{1}{|\beta|^{\alpha' t}}. \tag{2.30}$$

### 2.2.2 Parametrization of the D–Term

In order to complete the parametrization of the GPD $H^q(x, \xi, t)$ the D–term has to be specified. Calculations in the chiral quark–soliton model show that $D^u(z) \approx D^d(z)$. Therefore it is assumed that

$$D(z) = \frac{1}{N_f} \sum_q D^q(z) = \frac{1}{N_f}\, D^Q(z), \tag{2.31}$$

where $N_f$ is the number of active flavors and $D(z)$ yields the same contribution for each quark flavor. The D–term can then be expanded in a Gegenbauer polynomial

$$D^Q(z) = (1 - z^2)\, [d_1^Q\, C_1^{3/2}(z) + d_3^Q\, C_3^{3/2}(z) + d_5^Q\, C_5^{3/2}(z) + \ldots], \tag{2.32}$$

where the possible physics meaning of the first coefficient $d_1^Q$ was already discussed in section 2.1.2. Based on the calculation of GPDs in the chiral quark–soliton model [Pet98] the values of the first few coefficients have been calculated. They all came out negative with the coefficient $d_1^Q \approx -4.0$ giving the largest contribution. The resulting D–term is represented in figure 2.4 for one quark flavor, i.e, by dividing equation 2.32 by $N_f = 3$ according to equation 2.31. The effect of the negative sign obtained for the coefficients is that the D–term in figure 2.4 gives a contribution opposite to the double distribution part. Therefore they counteract each other since they are added in the parametrization of the GPD $H^u$. Note that the D–term contributes only in the region $-\xi \leq x \leq \xi$ and therefore is not accessible in the forward limit. The resulting parametrization of the GPD $H^u$ including the double distribution and the D–term is shown in figure 2.5. Moving along lines of constant $x$ and increasing the skewedness $\xi$, the sensitivity of the GPD to the D–term part increases relative to the double distribution part. In the limit $\xi = 1$ the D–term contribution dominates the GPD $H$. Note that due to a lack of information the $t$–dependence of the D–term is assumed to be the same as for the double distribution contribution.

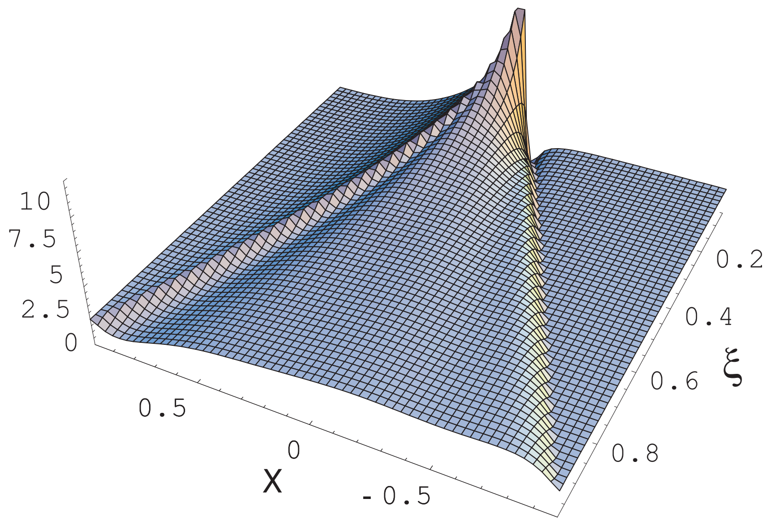


**Figure 2.5:** The $x$ and $\xi$ dependence of the GPD $H^u$ including the double distribution part for $b_{val} = b_{sea} = 1$ and the D–term [Goe01].

# Chapter 3

# Deeply–Virtual Compton Scattering

The scattering of photons off charged particles is called Compton scattering, first measured in photon–electron scattering by A.H. Compton [Com23]. The **D**eeply–**V**irtual **C**ompton **S**cattering (DVCS) process denotes the process of Compton scattering of a virtual photon, generated by inelastic lepton scattering in the Bjorken limit, with a real photon in the final state. Utilizing the DVCS process to access GPDs was first proposed by Ji [Ji97a].

## 3.1 Kinematics

The exclusive leptoproduction of a photon off a proton

$$e(k) + P(p) \rightarrow e(k') + P(p') + \gamma(q') \tag{3.1}$$

is described in terms of the four–momenta $k$ ($k'$) and $p$ ($p'$) of the incoming (outgoing) lepton and the initial (final) proton, respectively. The four–momentum of the exchanged virtual photon is given by $q \equiv k - k'$ and the photon virtuality is defined as

$$Q^2 \equiv -q^2 = -(k-k')^2 \overset{\text{lab}}{\approx} 4\,E\,E'\,\sin^2(\frac{\theta}{2}). \tag{3.2}$$

The calculation of $Q^2$ in the laboratory (lab) frame of a fixed–target experiment uses the scattering angle $\theta$ defined between the initial and final lepton trajectories and the corresponding lepton energies $E$ and $E'$, respectively. The momentum fraction of the proton carried by the struck quark is denoted by the Bjorken variable

$$x_B \equiv \frac{Q^2}{2\,p\,q} = \frac{Q^2}{2\,M_p\,\nu}, \tag{3.3}$$

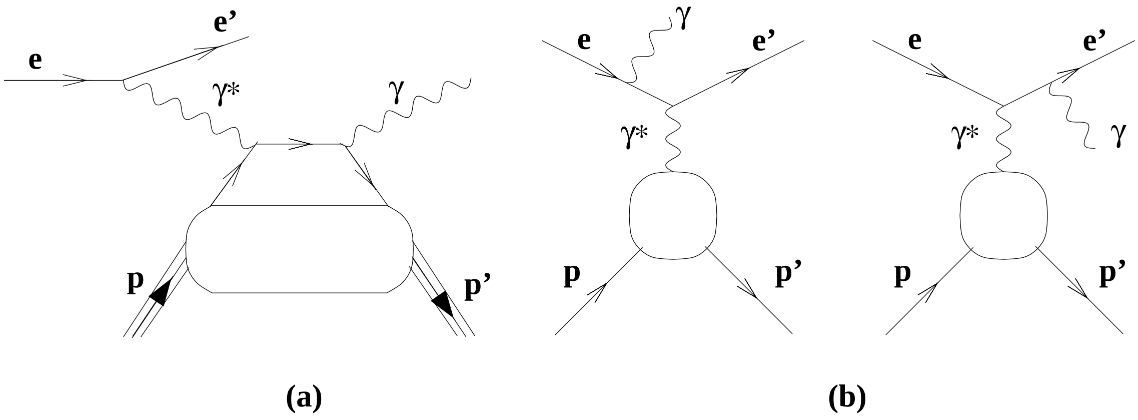


**Figure 3.1:** Diagrams for deeply–virtual Compton scattering (a) and for the radiation of a photon from the incoming or outgoing electron in the Bethe–Heitler process (b).

---

with the mass of the proton $M_p$ and the energy of the virtual photon

$$\nu \equiv \frac{p\,q}{M_p} \stackrel{\text{lab}}{=} E - E'. \tag{3.4}$$

The variable

$$y \equiv \frac{p\,q}{p\,k} \stackrel{\text{lab}}{=} \frac{\nu}{E} \tag{3.5}$$

represents the fractional energy of the virtual photon with respect to the beam energy. The squared energy in the photon–proton center of mass-system is given by

$$W^2 = (q+p)^2 = M_p^2 + 2\,M_p\,\nu - Q^2. \tag{3.6}$$

The Mandelstam invariant

$$t = (p-p')^2 = (q-q')^2 \tag{3.7}$$

can be calculated using the four–momenta of either the protons or the photons.

## 3.2 Cross Section

Expression 3.1 describes not only the DVCS process displayed in figure 3.1(a) but also the **B**ethe–**H**eitler (BH) process shown in figure 3.1(b), where the produced real photon is emitted by the electron. Note that the kinematic variables defined above are calculated for the DVCS and BH processes, although the physics meaning of these variables, motivated by the elastic and the deeply–inelastic scattering

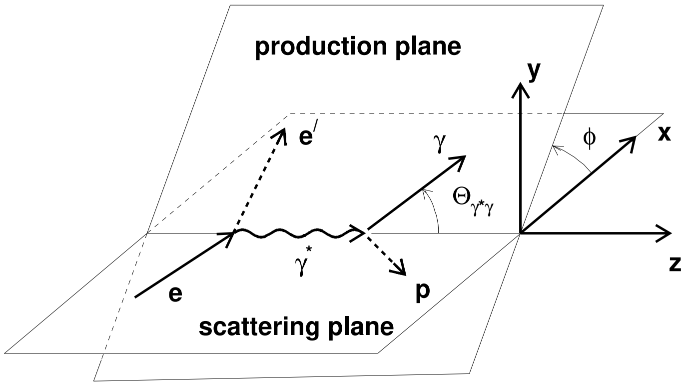


**Figure 3.2:** Schematic view of the azimuthal angle $\phi$ defined between the lepton scattering plane and the photon production plane and of the polar angle $\theta_{\gamma^*\gamma}$ defined between the virtual and the real photon.

processes, is restricted to the DVCS process. Both processes have an identical final state, i.e., they are indistinguishable and thus their scattering amplitudes add coherently. The photon production amplitude $\tau$ is then given as the sum of the amplitudes of the DVCS ($\tau_{DVCS}$) and BH ($\tau_{BH}$) processes. The squared photon production amplitude reads

$$|\tau|^2 = |\tau_{BH} + \tau_{DVCS}|^2 = |\tau_{BH}|^2 + |\tau_{DVCS}|^2 + \underbrace{\tau_{DVCS}\,\tau_{BH}^* + \tau_{DVCS}^*\,\tau_{BH}}_{I}, \tag{3.8}$$

where $I$ denotes the BH–DVCS interference term. For an unpolarized proton target, the four–fold cross section for the process denoted in equation 3.1 is given by [Bel02a]

$$\frac{d\sigma}{dx_B\,dy\,d|t|\,d\phi} = \frac{\alpha_{em}^3\,x_B\,y}{8\,\pi\,Q^2\sqrt{1+4\,x_B^2\,M_p^2/Q^2}}\left|\frac{\tau}{e^3}\right|^2, \tag{3.9}$$

with the fine–structure constant $\alpha_{em}$ and the charge of the lepton $e$. The azimuthal angle $\phi$ is defined as the angle between the lepton scattering plane, i.e., the plane defined by the incoming and the outgoing lepton trajectories, and the photon production plane made up correspondingly by the virtual and the real photon, as shown in figure 3.2. Measurements integrating over the angle $\phi$ receive no leading twist contribution from the interference term to the cross section, as will be explained in more detail in section 3.4.1. In leading twist, the DVCS cross section can then be obtained through a measurement of the photon production cross section when subtracting the BH cross section. This is possible since the latter is exactly calculable in **Q**uantum **E**lectro**d**ynamics (QED) with the knowledge of the Dirac and Pauli

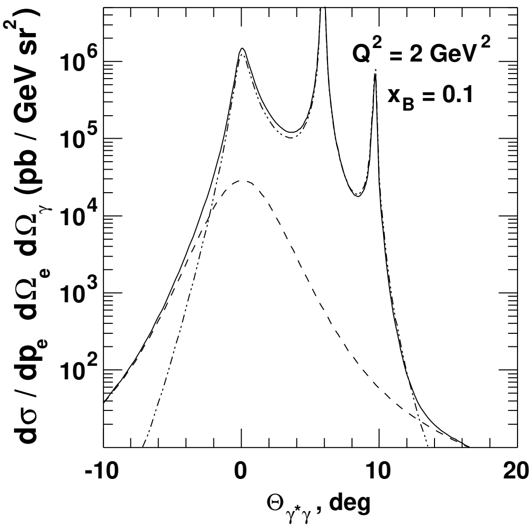


**Figure 3.3:** Differential in–plane cross section as a function of the angle $\theta_{\gamma^*\gamma}$ between the virtual and the real photon for DVCS (dashed line), BH (dashed–dotted line) and total $\gamma$ production (solid line) in ep interactions at the HERMES beam energy $E = 27.5$ GeV and at fixed values of $x_B$ and $Q^2$. Positive values of $\theta_{\gamma^*\gamma}$ correspond to $\phi = 0$, negative ones to $\phi = \pi$. Figure taken from reference [Kor02a]. Note that the range used in this analysis corresponds to $|\theta_{\gamma^*\gamma}| < 45$ mrad ($\approx 2.5°$).

---

form factors $F_1$ and $F_2$, respectively. However, a cross section measurement with sufficient precision can be carried out only if the BH cross section is not strongly dominating the DVCS cross section. This is the case at the collider experiments H1 and ZEUS at DESY where the first DVCS cross section measurements have been performed recently (see section 3.4.1). The situation for the kinematic regime of the HERMES experiment is shown in figure 3.3 for the specific case that the produced photon is in the same plane as the incoming and outgoing electron, i.e., $\phi = 0$ or $\phi = \pi$. The differential cross sections for the DVCS, BH and total photon production processes are displayed as a function of the angle $\theta_{\gamma^*\gamma}$ which is the polar angle between the virtual and the real photon, as shown in figure 3.2. Note that contrary to its usual definition the polar angle $\theta_{\gamma^*\gamma}$ in figure 3.3 can become negative. Positive values of $\theta_{\gamma^*\gamma}$ correspond to $\phi = 0$, negative ones to $\phi = \pi$. The DVCS cross section has its maximum at $\theta_{\gamma^*\gamma} = 0$, while the BH cross section has a three peak structure corresponding to the real photon being essentially collinear to the virtual photon or the incoming or outgoing electron, commonly referred to as Compton peak, **I**nitial **S**tate **R**adiation (ISR) and **F**inal **S**tate **R**adiation (FSR), respectively. Since at HERMES kinematics the DVCS cross section is at least an order of magnitude smaller than the BH cross section, the subtraction of the calculated BH cross section from a measured total photon production cross section would lead to large uncertainties. In addition, since at HERMES the full final state of the reaction cannot be detected unambiguously, the contribution from other processes might be significant. It is thus not yet feasible to measure the DVCS cross section at HERMES with sufficient precision.

## 3.3 Azimuthal Asymmetries

Although the DVCS cross section is difficult to access at HERMES, the BH–DVCS interference term offers the possibility to directly access the DVCS amplitudes which eventually can be expressed in terms of GPDs. The three parts that make up the photon production cross section (see equation 3.8) can be expanded in Fourier series. For an unpolarized proton target they read [Bel02a]

$$\begin{aligned} |\tau_{BH}|^2 &= \frac{e^6}{x_B^2\, y^2\, t\, (1 + 4\, x_B^2\, M_p^2/Q^2)^2\, P_1(\phi)\, P_2(\phi)} \\ &\qquad \times \left\{ c_0^{BH} + \sum_{n=1}^{2} c_n^{BH} \cos(n\phi) \right\}, \quad (3.10) \\ |\tau_{DVCS}|^2 &= \frac{e^6}{y^2\, Q^2} \left\{ c_0^{DVCS} + \sum_{n=1}^{2} c_n^{DVCS} \cos(n\phi) + \lambda\, s_1^{DVCS} \sin(\phi) \right\}, \quad (3.11) \\ I &= \frac{\pm e^6}{x_B\, y^3\, t\, P_1(\phi)\, P_2(\phi)} \left\{ c_0^I + \sum_{n=1}^{3} c_n^I \cos(n\phi) + \sum_{n=1}^{2} \lambda\, s_n^I \sin(n\phi) \right\}, \quad (3.12) \end{aligned}$$

where the + (-) sign in the interference term $I$ stands for a negatively (positively) charged lepton beam. The Fourier coefficients $c_n$ and $s_n$ depend on the kinematic variables $x_B$, $y$, $Q^2$ and $t$ and on the beam as well as on the target polarization. Note that the BH propagators $P_1(\phi)$ and $P_2(\phi)$ in the squared BH and in the interference term have an additional dependence on the azimuthal angle $\phi$. They are approximately given by $P_i(\phi) = A_i + B_i \cos(\phi)$, whereby $B_i$ is suppressed by at least $\mathcal{O}(1/Q)$. The exact expressions for the Fourier coefficients for an unpolarized target and for the BH propagators are lengthy and therefore not shown here, but can be found in reference [Bel02a]. Note that the dependence of the Fourier coefficients on the beam polarization $\lambda$ has been taken out of the expressions given in reference [Bel02a] and put into the equations 3.11 and 3.12 for later convenience.

The Fourier coefficients of the interference term ($c_n^I$ and $s_n^I$) are proportional to the DVCS amplitudes. Appropriate asymmetries are needed to disentangle the different contributions in order to extract them. The beam–spin and the beam–charge asymmetry are suitable for this purpose. They are described in the next two sections, based on reference [Bel02a], followed by the explanation on how the Fourier coefficients are related to the DVCS amplitudes (see section 3.3.3) and to the GPDs (see section 3.3.4).

### 3.3.1 Beam–Spin Asymmetry

The beam–spin asymmetry

$$A_{LU}(\phi) = \frac{d\overrightarrow{\sigma} - d\overleftarrow{\sigma}}{d\overrightarrow{\sigma} + d\overleftarrow{\sigma}}, \tag{3.13}$$

where $A_{LU}$ denotes the asymmetry (A) using a longitudinally (L) polarized beam and an unpolarized (U) target, is a cross section asymmetry built from two measurements with opposite beam helicity denoted by arrows with opposite orientation. Assuming that the magnitude of the polarization is the same in both helicity states, only those Fourier coefficients in the equations 3.10 – 3.12 that depend on $\lambda$ ($s_1^I$, $s_2^I$, and $s_1^{DVCS}$) are left in the numerator and only those independent of $\lambda$ (all others) contribute to the denominator. Among the three Fourier coefficients in the numerator only $s_1^I$ is related to the leading twist–2 quark GPDs, while $s_2^I$ and $s_1^{DVCS}$ are twist–3 contributions and therefore suppressed. The assumption that the denominator should be dominated by the $|\tau_{BH}|^2$ contribution is supported by figure 3.3 where the DVCS cross section at HERMES kinematics is shown to be about an order of magnitude smaller than the BH one in the $\theta_{\gamma^*\gamma}$ range used in this analysis. The dominant contribution in the BH cross section itself originates from the $c_0^{BH}$ term. Assuming that the BH propagators $P_1(\phi)$ and $P_2(\phi)$ in the numerator and in the denominator largely cancel each other, the beam–spin asymmetry $A_{LU}$ can be approximated at leading twist as

$$A_{LU}(\phi) \approx \pm \frac{x_B}{y} \frac{s_1^I}{c_0^{BH}} \sin(\phi). \tag{3.14}$$

Hence, if the above assumptions hold, the beam–spin asymmetry should predominantly show a $\sin\phi$ modulation which changes its sign depending on the beam charge. First measurements carried out recently at HERMES and CLAS will be described in section 3.4.2. The observation of an additional $\sin 2\phi$ dependence would probably allow access to the higher twist coefficient $s_2^I$ (see section 3.3.3).

### 3.3.2 Beam–Charge Asymmetry

The focus of this work will be on the hitherto unmeasured beam–charge asymmetry

$$A_C(\phi) = \frac{d\sigma^+ - d\sigma^-}{d\sigma^+ + d\sigma^-}, \tag{3.15}$$

where $d\sigma^+$ and $d\sigma^-$ denote the cross section measurement with a positron and an electron beam, respectively. The cross section difference in the numerator directly projects out the interference term $I$ since it is the only term that depends on the charge (see equations 3.10 – 3.12), the denominator gets contributions only from the charge independent squared BH and squared DVCS term. Assuming unpolarized beam ($\lambda = 0$), only the Fourier coefficients $c_n^I$ contribute to the numerator. Among these, the coefficients $c_0^I$ and $c_1^I$ are related to the same leading twist quark GPDs, but $c_0^I$ is kinematically suppressed by $\mathcal{O}(1/Q)$ compared to $c_1^I$. The coefficient $c_2^I$ arises at twist–3 level and the Fourier coefficient $c_3^I$ originates from the twist–2 helicity–flip gluon GPDs, suppressed by $\alpha_s/\pi$, or from twist–4 quark GPDs. Further details are given in the next section. Thus the leading term in the numerator is $c_1^I$. As for the beam–spin asymmetry, the denominator should be dominated by the BH squared term at HERMES kinematics (see figure 3.3), whereby the $c_0^{BH}$ term gives the largest contribution to the BH squared term. Under the assumption that the BH propagators from the BH squared and from the interference term largely cancel each other, the beam–charge asymmetry at leading twist is approximately given as

$$A_C(\phi) \approx -\frac{x_B}{y}\frac{c_1^I}{c_0^{BH}}\cos(\phi). \tag{3.16}$$

Consequently, a measurement of the beam–charge asymmetry should predominantly reveal a $\cos\phi$ dependence, probably accompanied by an offset and by $\cos 2\phi$ and $\cos 3\phi$ modulations.

### 3.3.3 From Azimuthal Asymmetries to DVCS Amplitudes

In terms of DVCS amplitudes, the leading Fourier coefficients accessible via the beam–spin asymmetry ($s_1^I$) and via the beam–charge asymmetry ($c_1^I$) are proportional to the imaginary and the real part of the photon helicity conserving amplitudes $M^{1,1}$,respectively. Here $M^{\mu,\mu'}$ denotes the helicity amplitudes with an initial (final) state photon helicity $\mu$ ($\mu'$), following the notation in reference [Die97]. In this case the helicity of the virtual and the real photon is the same. The helicity conserving amplitude $M^{1,1}$ appears at leading twist–2 and is related to twist–2 GPDs only, as explained in the next section. The Fourier coefficient $c_0^I$ is related to the same amplitude, but it is kinematically suppressed by $\mathcal{O}(1/Q)$.

Beyond leading twist, the coefficient $s_2^I$ ($c_2^I$), accompanied by a $\sin 2\phi$ ($\cos 2\phi$) modulation, is related to the imaginary (real) part of the helicity non–conserving amplitudes $M^{0,1}$ and $M^{0,-1}$, corresponding to the virtual photon being longitudinal. The conservation of angular momentum is assured by either the exchange of an additional gluon (genuine or dynamic twist–3) or by the fact that quarks can carry

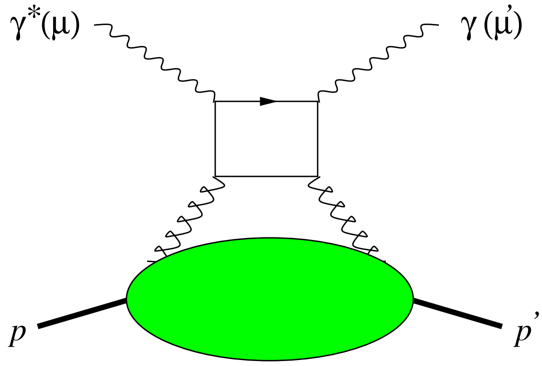


**Figure 3.4:** Feynman diagram for the photon helicity–flip amplitude. The relevant helicity combinations are $(\mu, \mu') = (1, -1)$ and $(\mu, \mu') = (-1, 1)$. Figure taken from reference [Die01].

non–zero orbital angular momentum along the collision axis (kinematic twist–3). Note that the latter contribution can be related to the twist–2 GPDs using the **W**andzura–**W**ilczek (WW) approximation and thus is also referred to as WW part of the twist–3 contribution. In addition, the interplay between the BH propagators ($P_1(\phi)$, $P_2(\phi)$) and other azimuthal dependences, e.g., the $\sin\phi$ dependence of the interference term, can give rise to $\sin 2\phi$ modulations as well. Note that also other modulations can be generated in a similar way, as will be discussed in section 9.2.

The Fourier coefficient $c_3^I$ is accessible through $\cos 3\phi$ modulations and proportional to the real part of the photon helicity non–conserving amplitudes $M^{1,-1}$ and $M^{-1,1}$. The amplitudes $M^{1,-1}$ and $M^{-1,1}$ are the photon helicity–flip amplitudes (see figure 3.4), i.e., also the virtual photon is transverse but both photons have opposite helicity. Gluon helicity–flip GPDs are able to compensate the two units of angular momentum. They appear at leading twist, but are suppressed by a factor $\alpha_s/\pi$. In addition, as in the case of the kinematic twist–3 contribution, it is possible that the two participating quarks accomplish the conservation of angular momentum if they carry orbital angular momentum. Since they have to account for two units of angular momentum instead of one as above, this process appears at twist–4. Also this kinematic twist–4 contribution has been found to be calculable in terms of twist–2 quark GPDs using the WW approximation [Kiv01b].

### 3.3.4 From DVCS Amplitudes to GPDs

In the following, the relation between the DVCS amplitudes and the GPDs is shown for the leading contributions only. Summarizing the leading twist (handbag) approximation, the beam–spin and the beam–charge asymmetry

$$\begin{aligned} A_{LU} &\sim s_1^I \sin(\phi) \sim Im(M^{1,1}) \sin(\phi), \quad (3.17)\\ A_C &\sim c_1^I \cos(\phi) \sim Re(M^{1,1}) \cos(\phi), \quad (3.18)\end{aligned}$$

give access to the imaginary and real part of the photon–helicity conserving DVCS amplitude $M^{1,1}$, respectively. The DVCS amplitude

$$M^{1,1} = F_1(t)\, H_1(\xi,t) + \frac{x_B}{2-x_B}(F_1(t)+F_2(t))\, \tilde{H}_1(\xi,t) - \frac{t}{4M^2}F_2(t)\, E_1(\xi,t) \quad (3.19)$$

is given by a linear combination of the so–called Compton form factors (CFFs) $H_1$, $\tilde{H}_1$ and $E_1$, together with the Dirac and Pauli form factors $F_1$ and $F_2$, respectively. The involved CFFs entirely appear at twist–2 and in fact are convolutions of the hard scattering amplitude and the twist–2 GPDs $H$, $\tilde{H}$ and $E$. The hard scattering parts are exactly calculable in pQCD. For the DVCS process next–to leading order calculations have been carried out [Bel98, Ji98a, Man98b].

At small values of $x_B$ ($t$) the contribution from the CFFs $\tilde{H}_1$ ($E_1$) to the amplitude $M^{1,1}$ is suppressed (see equation 3.19). Therefore the main contribution to the asymmetries in the kinematic region of this analysis originates from the CFF $H_1$, as will be discussed in section 9.1, and with

$$\begin{aligned} Im\, H_1(\xi,t) &= -\pi \sum_q e_q^2 \left(H^q(\xi,\xi,t) - H^q(-\xi,\xi,t)\right), \quad (3.20)\\ Re\, H_1(\xi,t) &= \sum_q e_q^2 \left[ P \int_{-1}^{1} H^q(x,\xi,t) \left(\frac{1}{x-\xi} + \frac{1}{x+\xi}\right) dx \right], \quad (3.21)\end{aligned}$$

it originates from the GPD $H^q(x,\xi,t)$. Here, P denotes Cauchy's principal value. Analogous expressions are valid for the other CFFs $\tilde{H}_1$, $E_1$ and $\tilde{E}_1$ which in principle can be accessed through other asymmetries measurable on longitudinally or transversely polarized targets. Note that the imaginary part of the CFFs is directly proportional to the GPDs at $x = \pm\,\xi$, i.e., the GPD $H$ in figure 2.5 is only accessible along a line $x = \pm\,\xi$. Consequently, beam–spin asymmetries are insensitive to the D–term contribution since the latter contributes only in the region $-\xi \leq x \leq \xi$ as seen in figure 2.4. The $x$–dependence of the GPDs away from the line $x = \pm\,\xi$ is only accessible via the real part, i.e., through a measurement of the beam–charge asymmetry.

## 3.4 Measurements of Deeply–Virtual Compton Scattering

The already performed DVCS measurements of cross sections and beam–spin asymmetries will be described in the following.

### 3.4.1 Measurements of Cross Sections

Recently, the first DVCS cross section measurements have been reported by the H1 [Adl01] and ZEUS [Sau01] collaborations at DESY. The data was collected in 1996 and 1997 using the colliding 27.5 GeV positron and 820 GeV proton beams[1] at HERA. Since both experiments have similar experimental setups they employ a similar method for their analysis. Around the interaction region they are equipped with tracking devices surrounded by calorimeters. The scattered proton escapes detection since it travels down the beam pipe, therefore only the scattered positron and the photon are measured. For DVCS events the scattered positron usually is not within the acceptance of the tracking devices and thus only gives a signal in the calorimeter. Because of this, no vertex reconstruction is possible and the kinematics are poorly reconstructed. The event selection is therefore based on the detection of two electromagnetic clusters and at most one reconstructed track. With the incoming proton defining the forward direction of the detectors, one of the clusters is in addition required to be in the rear part of the detector, the other one in the central or forward part. If a track can be reconstructed it has to be associated to one of the clusters and determines the positron candidate. If no track was reconstructed, the cluster in the rear part is assumed to be the positron. These events are then subdivided into two samples where the positron is either in the forward/central region (control sample), corresponding to larger values of $Q^2$, or in the rear region (enriched sample), corresponding to smaller values of $Q^2$. The control sample is dominated by BH events with some additional background since the DVCS cross section is kinematically suppressed by $1/Q^2$ compared to the BH cross section (see equations 3.10 and 3.11). The enriched sample, on the other hand, contains DVCS events as well as BH events plus additional background. A simulation of the BH contribution that describes the control sample can then be used to subtract the BH contribution from the enriched sample. This directly leads to the DVCS cross section if the contribution of the interference term given in equation 3.12 is zero. This holds true in the leading–twist approximation since $c_0^I$ is suppressed by $\mathcal{O}(1/Q)$ with respect to the leading-twist contribution and the $\phi$–dependent terms

[1] The energy of the proton beam was increased to 920 GeV in the beginning of 1998.

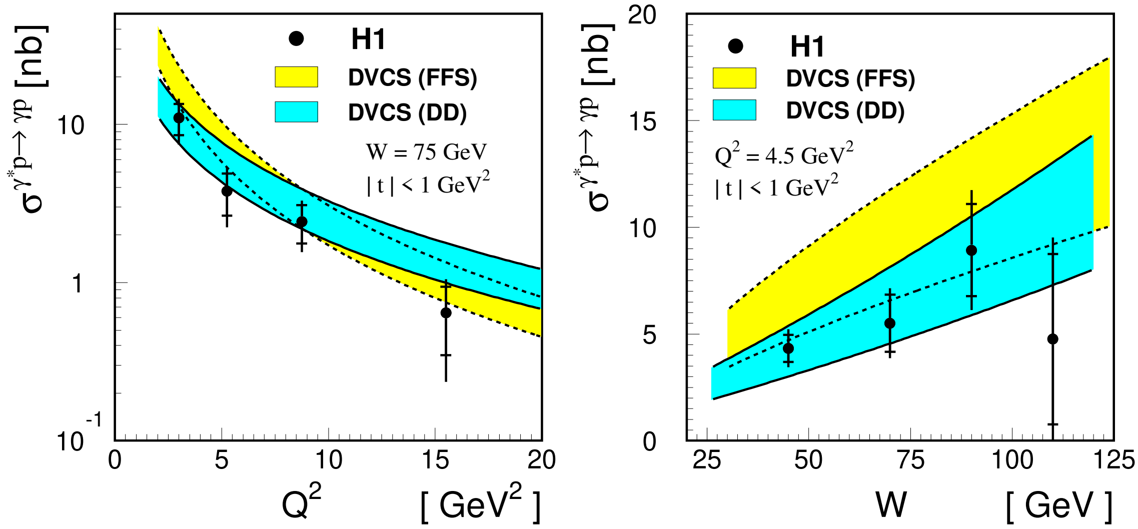


**Figure 3.5:** H1 results [Adl01] on the $\gamma^* p \to \gamma p$ cross section for the DVCS process as a function of $Q^2$ (left panel) and $W$ (right panel), where the data have been scaled to central values of $W = 75$ GeV and $Q^2 = 4.5$ GeV$^2$, respectively. The data are compared to the theoretical predictions of FFS [Fra98] and DD [Don01]. The uncertainty in the predictions (shaded bands) is due to the unknown $t$–slope which is assumed to be between 5 GeV$^{-2}$ (upper bound) and 9 GeV$^{-2}$ (lower bound).

---

in the interference term vanish as the measurement is integrating over the azimuthal angle. Note that at the same time the DVCS amplitude squared in equation 3.11 is non–zero since the Fourier coefficient $c_0^{DVCS}$ arises at twist–2.

The $\gamma^* p$ cross section for the DVCS process, as obtained by H1, is shown in figure 3.5 as a function of $Q^2$ for $W = 75$ GeV, and as a function of $W$ for $Q^2 = 4.5$ GeV$^2$. The data cover the kinematic range $2 < Q^2 < 20$ GeV$^2$, $30 < W < 120$ GeV and $-t < 1$ GeV$^2$. It is compared to a model calculation by Frankfurt, Freund and Strikmann (FFS) [Fra98] and to another one by Donnachie and Dosch (DD) [Don01]. The data agrees with both models within the theoretical uncertainties, which are due to the up to now unmeasured $t$–dependence of the cross section. Since theoretical predictions are absent as well, an exponential ansatz for the $t$–dependence is assumed ($e^{-b|t|}$) with 5 GeV$^{-2}$ $< b <$ 9 GeV$^{-2}$. The range for the $t$-slope covers the measured range for light vector meson production, i.e., it was chosen under the assumption that the production of real photons and light vector mesons have a similar $t$-slope.

The preliminary result from ZEUS is shown in figure 3.6 for $Q^2 > 5$ GeV$^2$ and $40 < W < 140$ GeV. Noting that a contribution of about 20% from processes where

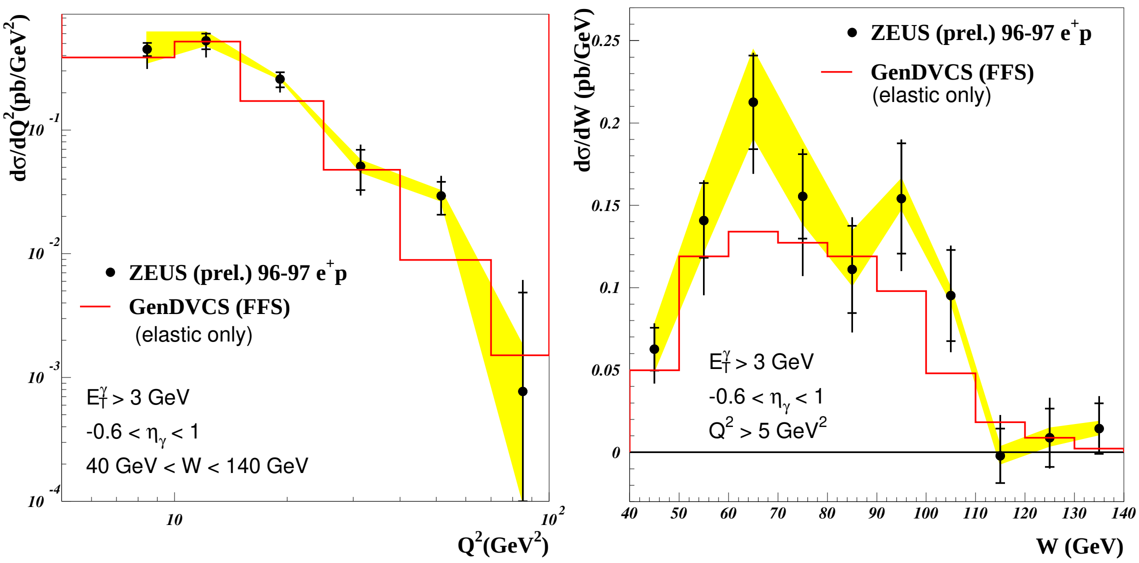


**Figure 3.6:** Preliminary ZEUS result [Sau01] on the $ep \rightarrow ep\gamma$ cross section for the DVCS process as a function of $Q^2$ (left panel) and $W$ (right panel). The data are compared to the theoretical predictions of FFS [Fra98] using a $t$–slope of 4.5 GeV$^{-2}$. The shaded bands represent the uncertainty in the energy scale of the calorimeter.

the proton does not stay intact has not been subtracted, the prediction by FFS [Fra98] reproduces the data when setting $b = 4.5$ GeV$^{-2}$.

### 3.4.2 Measurements of the Beam–Spin Asymmetry

Recent measurements of the beam–spin asymmetry carried out by HERMES [Air01] and CLAS [Ste01] indeed exhibit the expected $\sin\phi$ dependence (see equation 3.14) as shown in figure 3.7. The HERMES (CLAS) collaboration employed a polarized positron (electron) beam with an energy of 27.6 (4.25) GeV scattered off gaseous (liquid) hydrogen. The beam polarization had an average value of 55% and 70% for HERMES and CLAS, respectively. Since both experiments are not able to unambiguously detect the full final state of the reaction missing mass techniques are employed.

Since at HERMES the recoiling proton cannot be detected, events containing exactly one positron and one photon were selected. The missing mass of the reaction $\vec{e}^{\,+} p \rightarrow e^+ \gamma X$ was required to be between -1.5 and 1.7 GeV, i.e., $-3\sigma$ below and $1\sigma$ above the proton mass $M_p$. Negative missing mass values arise due to the finite resolution of the HERMES spectrometer, as will be explained in section 5.4.3

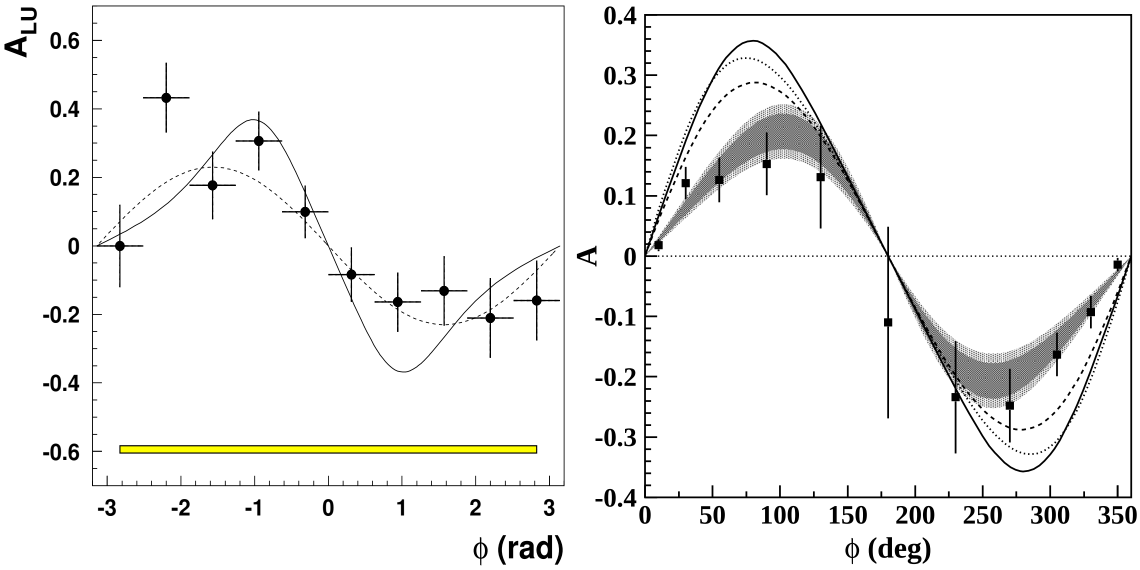


**Figure 3.7:** Beam–spin asymmetries $A_{LU}$ for the hard electroproduction of photons off the proton as a function of the azimuthal angle $\phi$ as obtained by HERMES [Air01] (left panel) and CLAS [Ste01] (right panel). Left panel: The curves represent a $\sin\phi$ dependence with an amplitude of 0.23 (dashed) and a model calculation [Kiv01a] (solid). The error band below shows the systematic uncertainty. Right panel: The dark shaded region corresponds to the statistical error of the fit to the function $A(\phi) = \alpha \sin\phi + \beta \sin 2\phi$. The light shaded region includes systematic uncertainties. The curves are model calculations [Van99, Goe01].

in more detail. The positron kinematics were required to satisfy $Q^2 > 1$ GeV$^2$, $W^2 > 4$ GeV$^2$ and $\nu < 24$ GeV. In order to have an almost full $\phi$–coverage the angle $\theta_{\gamma^*\gamma}$ was restricted to be smaller than 70 mrad. Due to insufficient position resolution of the reconstructed photon, the angle $\theta_{\gamma^*\gamma}$ had to be larger than 15 mrad to ensure a reliable determination of the angle $\phi$.

At CLAS, the reaction $\vec{e}^{\,-} p \to e^- p \gamma$ is identified by analyzing the missing mass squared distribution in the reaction $\vec{e}^{\,-} p \to e^- p X$. In contrast to HERMES, the recoiling proton can be detected, but the missing mass resolution at CLAS is not sufficient to separate the single photon production events from events where a $\pi^0$ is produced. Therefore the number of single photon events per bin in $\phi$ was determined using a fitting technique that analyzes the line shape of the missing mass squared distributions in each bin. The kinematic requirements on the data were $1 < Q^2 < 1.75$ GeV$^2$ and $0.1 < -t < 0.3$ GeV$^2$.

The results of the two experiments agree with each other within errors, despite the fact that there should be a dependence of the beam–spin asymmetry on the kinematic variables $x_B$, $Q^2$ and $t$, which are quite different for the two measurements. The average values of the kinematic variables corresponding to the HERMES measurement, as shown in the left panel of figure 3.7, are $\langle Q^2 \rangle = 2.6$ GeV$^2$, $\langle x_B \rangle = 0.11$ and $\langle -t \rangle = 0.27$ GeV$^2$. The obtained value for the beam–spin asymmetry is $-0.23 \pm 0.04$ (stat) $\pm 0.03$ (sys). Unfortunately CLAS does not quote their average kinematic values. The model calculations used to compare to the CLAS data (see right panel of figure 3.7) are carried out at fixed kinematic values of $Q^2 = 1.25$ GeV$^2$, $x_B = 0.19$ and $-t = 0.19$ GeV$^2$, which are probably close to the actual average values of the data. A fit to the data points with the function $A(\phi) = \alpha \sin\phi + \beta \sin 2\phi$ yields $\alpha = 0.202 \pm 0.028$ (stat) $\pm 0.013$ (sys). The CLAS result has a positive sign whereas the one from HERMES has a negative sign as can already be seen when comparing the left and the right panel of figure 3.7, paying attention to the different ranges in $\phi$ displayed on the abscissa. This is due to the charge of the respective beam and is reflected by the $\pm$ sign in front of equation 3.14.

In contrast to HERMES the CLAS Collaboration also quotes a value for the $\sin 2\phi$ contribution. The amplitude is $\beta = -0.024 \pm 0.021$ (stat) $\pm 0.009$ (sys) and thus compatible with zero within errors.

The model calculations displayed in figure 3.7 are carried out based on the parametrization of GPDs as described in section 2.2. The D–term is included for all curves although the beam–spin asymmetry is insensitive to its contribution. The dashed curve used to compare to the CLAS measurement is a twist–2 calculation without a $\xi$–dependence for the GPDs, i.e., $b \to \infty$ in equation 2.22, the dotted curve is a twist–2 calculation with a $\xi$–dependence and the solid curve includes twist–3 effects in the WW approximation. The HERMES measurement is compared to the calculation with twist–3 effects included only. In general, all model calculations agree in sign but slightly overshoot the data in size.

# Chapter 4

# The HERMES Experiment

The HERMES (HERa MEasurement of Spin) experiment was set up in 1994/95 in the East–Hall of the HERA (Hadron Elektron Ring Anlage) electron/positron–proton collider at DESY (Deutsches Elektronen–Synchrotron). HERMES is a fixed–target experiment and uses only the longitudinally polarized lepton[1] beam scattering off an internal polarized or unpolarized gas target. The HERMES detector is a forward spectrometer, determining the momentum of charged particles via tracking chambers located before and behind the spectrometer magnet. The trigger is provided by a combination of hodoscopes and an electromagnetic calorimeter. The latter is in addition capable of measuring energies and positions of charged particles and photons and serves as **P**article–**ID**entification (PID) detector. The PID–System is completed by a **R**ing–**I**maging **Č**erenkov (RICH) counter, a **T**ransition–**R**adiation **D**etector (TRD) and a preshower detector. A small calorimeter close to the beam line serves as luminosity monitor.

In the following the experimental setup will be discussed in more detail while focusing on the parts needed for this analysis.

## 4.1 The Polarized Lepton Beam

The HERA storage rings have a circumference of 6.3 km and provide an electron/positron beam with a momentum of 27.57 GeV/c and a proton beam with a momentum of 920 GeV/c. Operation in the lepton ring was started with electrons, however, since the negatively charged electron beam tends to attract positively charged dust along its path, the lifetime of the beam is severely limited due to Bremsstrahlung losses. After HERMES started data taking in 1995, the lepton

[1]Throughout this thesis the term lepton refers to electrons and positrons only.

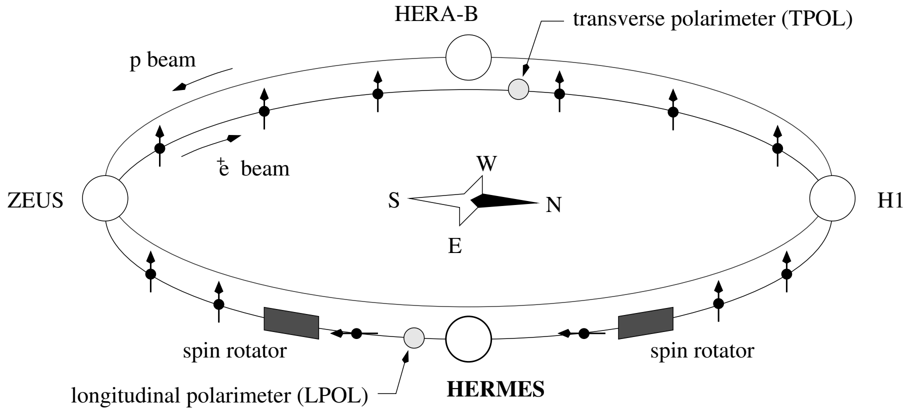


**Figure 4.1:** Schematic view of the HERA collider.

ring was operated with positrons except for a short period in 1998. The lepton beam is initially unpolarized after injection, i.e., the number of leptons with their spins aligned with the vertical magnetic field of the bending magnets ($N^{\uparrow}$) equals the number of leptons aligned in the opposite direction ($N^{\downarrow}$). The polarization P is defined as:

$$P = \frac{N^{\uparrow} - N^{\downarrow}}{N^{\uparrow} + N^{\downarrow}}. \tag{4.1}$$

A transverse polarization of the positron (electron) beam parallel (anti–parallel) to the magnetic dipole fields builds up naturally through the Sokolov–Ternov effect [Sok64], an asymmetry in the small spin–flip probability in the emission of synchrotron radiation in the arcs of the storage ring. The polarization in the ring increases exponentially with time according to

$$P(t) = P_{ST} \cdot \left(1 - exp\left\{-\frac{t}{\tau_{ST}}\right\}\right), \tag{4.2}$$

where $P_{ST}$ is the asymptotic maximum polarization value equal to about 92%, corresponding to the asymmetry in the spin flip amplitude. The characteristic polarization rise–time

$$\tau_{ST} = P_{ST} \frac{m_e}{\hbar c^2 r_e} \frac{\rho^3}{\gamma^5} \tag{4.3}$$

depends on $\rho$, the bending radius in the magnetic field and on the Lorentz factor $\gamma = E/m_e$, with the beam energy $E$ and the electron mass $m_e$. The classical electron radius is denoted by $r_e$. For the HERA storage ring this gives a polarization rise–time of about 40 minutes.

However, while the results given above are for an ideal machine, depolarizing effects in a real storage ring limit the achievable polarization to values smaller than

$P_{ST}$. The dominant contribution arises from non–vertical magnetic field components with respect to the beam orbit. This is due to small magnet misalignments, not perfectly homogenous magnetic fields and the use of other magnets than dipoles, e.g., quadrupoles to focus the beam. In addition, the emission of synchrotron radiation excites oscillations of the particles within a bunch around the design orbit and hence the particles experience non–vertical magnetic fields, leading to the so–called spin diffusion [Bar93]. Furthermore, beam–beam interactions between the lepton and the proton beam in the interaction zones at HERA may reduce the beam polarization.

All depolarization effects can be incorporated into a time constant $\tau_{dep}$, leading to a lower asymptotic maximum polarization value $P_{max}$ which is attained within shorter time $\tau$:

$$P_{max} = P_{ST}\frac{\tau_{dep}}{\tau_{ST}+\tau_{dep}}, \tag{4.4}$$

$$\tau = \tau_{ST}\frac{\tau_{dep}}{\tau_{ST}+\tau_{dep}}. \tag{4.5}$$

On the other hand, there are certain ways to improve the achievable maximum transverse polarization [Bar94] and values of up to 70% polarization have been reached at HERA. However, the typical maximum beam polarization is about 60% with a rise–time of $\tau \approx 25$ min.

As shown in figure 4.1, a spin rotator [Buo86] upstream of the HERMES interaction point turns this transverse beam polarization into the longitudinal direction, a second one downstream of the experiment rotates it back into the original direction.

### 4.1.1 Polarization Measurements

The beam polarization is measured with two independent polarimeters. One is installed in the west area of the HERA ring (see figure 4.1) and measures the transverse polarization (TPOL), the other one (LPOL) determines the longitudinal beam polarization and is therefore located in the HERMES area in between the spin rotators. Both polarimeters use the fact that the cross section for Compton scattering of polarized photons off polarized leptons is spin–dependent. Taking into account that only the vertical $P_y$ and the longitudinal $P_z$ component of the beam polarization are measured, the differential Compton cross section can be written as

$$\frac{d\sigma_C}{d\Omega} = \frac{1}{2}\,r_e^2\,(\frac{k_f}{k_i})^2\,[\Sigma_0 + S_1\Sigma_1 + S_3(P_y\Sigma_{2,y} + P_z\Sigma_{2,z})], \tag{4.6}$$

with $k_i$ and $k_f$ the initial and final photon momenta in the lepton rest frame and $S_1$ and $S_3$ the linear and circular component of the initial photon polarization. The terms $\Sigma_0$ ($\Sigma_1$, $\Sigma_2$) are the cross sections for unpolarized (polarized) scattering.

### The Transverse Polarimeter

Using a circularly polarized photon beam, the TPOL [Bar93] exploits the fact that $\Sigma_{2,y}$ has a spin–dependent azimuthal distribution. A linearly polarized photon beam provided by an argon ion laser, delivering continuous green light at 514.5 nm, is converted by a Pockels cell into a circularly polarized beam. The laser beam is transported through remotely controlled mirrors and lenses over about 200 m to the lepton–photon interaction point. The backscattered Compton photons, which have energies of up to 13.8 GeV, are detected in a tungsten scintillator sandwich calorimeter about 65 m from the interaction point. The calorimeter is split into an optically decoupled upper and lower part, symmetric around the lepton beam plane and thus allows to measure the energy and vertical position of the photons. During the measurement the polarization is flipped at 83.3 Hz, leading to an energy–dependent spatial asymmetry

$$\Delta y(E_\gamma) = \frac{1}{2}(\ \langle y(E_\gamma)\rangle^- - \langle y(E_\gamma)\rangle^+\ ) = \Delta S_3 \cdot P_y \cdot \Pi_y(E_y), \tag{4.7}$$

with $\langle y(E_\gamma)\rangle^\pm$ the mean vertical position of the distribution of Compton photons in the respective helicity state, and $\Delta S_3 = (S_3^+ - S_3^-)/2$ the mean magnitude of circular light polarization. The analyzing power $\Pi_y(E_y)$ relates the measured spatial asymmetry $\Delta y(E_\gamma)$ to the beam polarization $P_y$.

### The Longitudinal Polarimeter

Like the TPOL, the LPOL [Bec02] employs a circularly polarized photon beam, but unlike the y–component $\Sigma_{2,y}$ in equation 4.6, the z–component $\Sigma_{2,z}$ does not have a spin–dependent azimuthal distribution. Instead, a dependence on the energy of the backscattered Compton photons is used which is directly related to the polar scattering angle. Light pulses (532 nm) from a Nd:YAG laser, circularly polarized via a Pockels cell and with alternating helicity at each pulse, are transported through an optical system, similar to that of the TPOL, to the lepton–photon interaction point downstream of the HERMES experiment. The backscattered photons are detected about 54 m downstream of the interaction point by a calorimeter, consisting of a $2 \times 2$ array of radiation hard $NaBi(WO_4)_2$ Čerenkov crystals. Due to the Bremsstrahlung background in the area downstream of the HERMES experiment the LPOL uses the multi–photon method, i.e., about $10^3$ backscattered photons are produced per laser pulse and the energy sum of them is detected. Depending on the helicity of the laser light, the energy sum exhibits an asymmetry

$$A(\Delta S_3, P_z) = \Delta S_3 \cdot P_z \cdot \Pi, \tag{4.8}$$

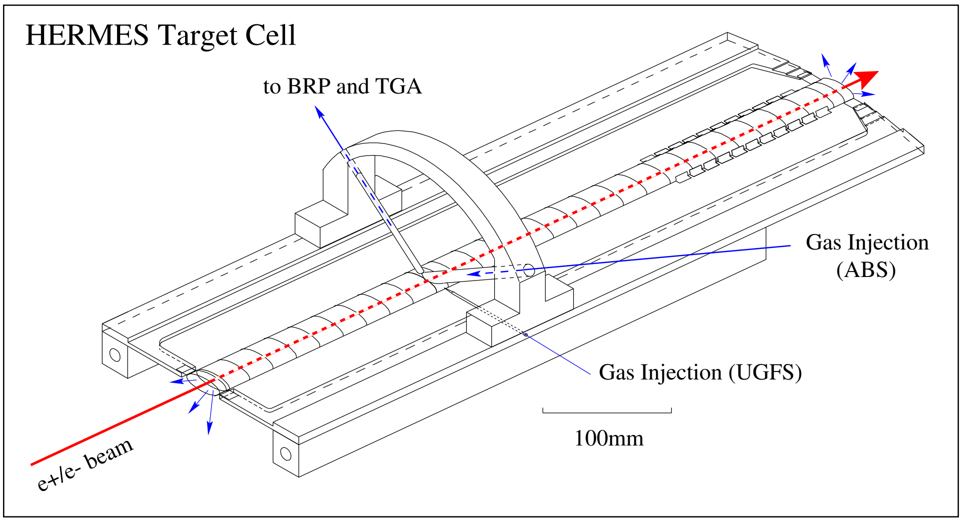


**Figure 4.2:** Schematic view of the HERMES target cell.

which is proportional to the average circular light polarization $\Delta S_3$ defined above and to the longitudinal polarization $P_z$.

## 4.2 The Internal Gas Target

HERMES uses a gas target internal to the storage ring. The thin–walled cryogenically cooled storage cell [Bau03a], mounted coaxially in the vacuum chamber, consists of an open–ended elliptical tube (see figure 4.2) made of ultra–pure aluminum with a uniform wall thickness of 75 $\mu$m and a length of 400 mm. Compared to free gas jet targets the target thickness in a storage cell is about two orders of magnitude larger [Hae85]. Further increase of the target density was achieved in the winter break 1999/2000 when the cell size was decreased from 9.8 mm height and 29 mm width to 8.9 $\times$ 21 mm$^2$, and at the same time the cell temperature was lowered from about 100 K to 60 K. A set of movable and fixed collimators is used to protect the target and the spectrometer against synchrotron light and beam halo particles. To maintain the ultra–high vacuum in the accelerator beam pipe, gas atoms are pumped away at both ends of the storage cell. The target gas is injected via two different tubes (see figure 4.2), depending on whether measurements with polarized or unpolarized gas are carried out.

### 4.2.1 The Unpolarized Target

A variety of pure unpolarized gaseous targets like $^{1}H_2$, $^{2}H_2$, $^{3}He$, $^{14}N_2$, $^{20}Ne$ and $^{84}Kr$ is used. The gas is inserted into the storage cell by the **U**npolarized **G**as **F**eed **S**ystem (UGFS) as shown in figure 4.2. In contrast to the polarized gases, where the technologically limited intensity of the polarized sources restricts the target density in the storage cell to about $10^{13}$ – $10^{14}$ nucleons/cm$^2$, typical densities of $10^{15}$ – $10^{17}$ nucleons/cm$^2$ can be achieved with the UGFS, restricted only by the fact that the reduction of the beam life time must not exceed a certain limit when measuring in parallel to other HERA experiments.

### 4.2.2 The Polarized Target

The polarized hydrogen/deuterium target consists of an **A**tomic **B**eam **S**ource (ABS), a **B**reit–**R**abi **P**olarimeter (BRP), a **T**arget **G**as **A**nalyzer (TGA) and a superconducting magnet to generate the holding field. The ABS [Nas03] supplies the target cell with polarized hydrogen or deuterium atoms, while the BRP [Bau02] measures the atomic polarization of the gas sampled from the cell by a sampling tube. The TGA [Bau03b] measures the degree of dissociation of the target gas with a quadrupole mass spectrometer. Since polarized targets are not used in this analysis no further details will be given here but can be obtained from the above quoted references and references therein.

## 4.3 The HERMES Spectrometer

The HERMES detector [Ack98] is a forward magnet spectrometer consisting of two identical halves located symmetrically above and below the HERA beam–lines. The origin of the HERMES coordinate system coincides with the center of the target. The positive $z$–axis is oriented along the lepton beam axis, the $y$–axis is pointing upwards and in the right–handed coordinate system the $x$–axis is pointing horizontally towards the outside of the ring, which means to the left when looking downstream. Since both the lepton and proton beams have to pass through the magnet they are shielded from its field by a horizontal steel plate with integrated compensator coils. This septum plate in conjunction with the magnet gap leads to an acceptance of 40 mrad $< |\theta_y| <$ 140 mrad and $|\theta_x| <$ 170 mrad. The horizontal acceptance is increased to 270 mrad behind the magnet to accommodate the deflection of charged low–momentum tracks.

The spectrometer (see figure 4.3) consists of three parts, the front and back regions

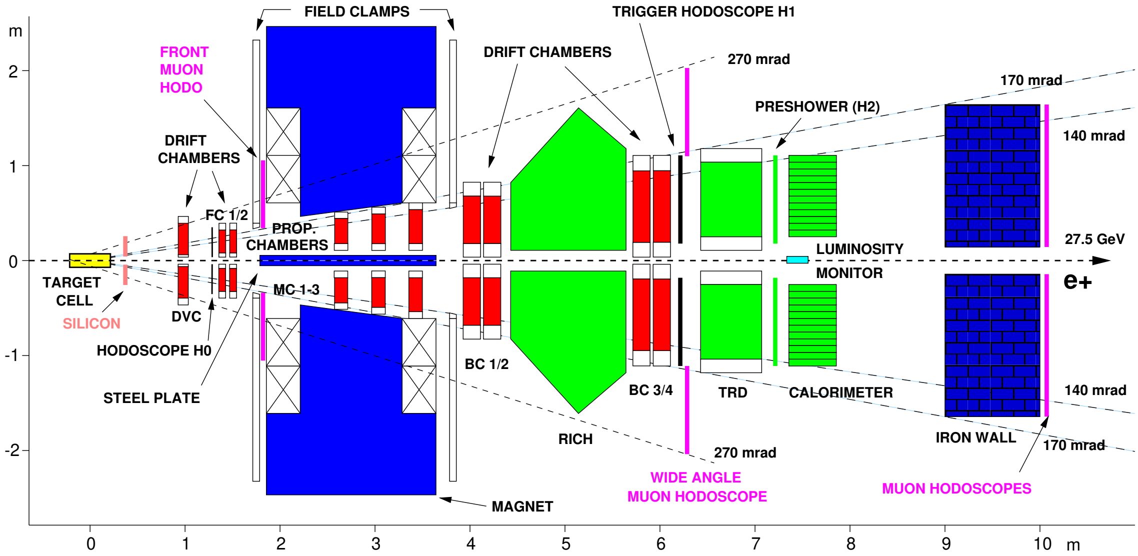


**Figure 4.3:** Schematic side view of the HERMES spectrometer.

divided by the spectrometer magnet. With the exception of a trigger hodoscope the front region only contains tracking devices which identify the trajectories of charged particles. While the magnet hosts some extra tracking chambers, the back region is composed of tracking, trigger, and particle–identification detectors.

### 4.3.1 Tracking

The tracking in the front and back regions of the spectrometer is entirely provided by horizontal drift chambers, namely, the **D**rift **V**ertex **C**hamber (DVC) and two **F**ront **C**hambers (FC 1/2) in front of the magnet and the four **B**ack **C**hambers (BC 1–4) behind it. The horizontally deflecting dipole magnet with an integrated field strength of 1.3 Tm hosts three proportional chambers, the **M**agnet **C**hambers (MC 1–3). The latter are mainly used for the reconstruction of particles with low momenta which get deflected into the iron yoke of the magnet before they can enter the rear part of the spectrometer. All chambers measure the horizontal coordinate $x$ with a plane of vertical wires ($X$–plane) and two coordinates $u$ and $v$ with wire planes which have their wires tilted by $\pm 30°$ ($U$–plane, $V$–plane) with respect to the wires in the $X$–plane.

Each drift chamber consists of six layers of drift cells, where each layer is constructed of a plane of alternating anode and cathode wires between the cathode foils, while the foils belong to the neighboring cell as well, if there is one. The drift cells have a size of 6 mm (DVC), 7 mm (FC) and 15 mm (BC). Two consecutive planes have the same wire inclination, while their drift cells are staggered by half a cell width to avoid left–right ambiguities ($U, U', X, X', V, V'$). The drift chambers are operated with an Ar (90%), $CO_2$ (5%), $CF_4$ (5%) gas mixture. They are read out by amplifier–shaper–discriminator cards mounted on–board the chambers and by TDCs with a time resolution of 0.5 ns. The spatial resolution per plane is about 220 $\mu$m for the DVC, 225 $\mu$m for the FCs and 275 (300) $\mu$m for the BCs 1–2 (3–4).

Since the MCs have to be operated in a strong magnetic field, **M**ulti–**W**ire **P**roportional **C**hambers (MWPCs) were chosen for this purpose. Each chamber consists of three layers of wire planes ($U, X, V$) with a wire spacing of 2 mm, whereas each wire plane is surrounded by two cathode foils. The gas mixture has the same constituents as the drift chamber gas, but with proportions (Ar (65%), $CO_2$ (30%), $CF_4$ (5%)) optimized for MWPC operation. Digital readout of the wires is accomplished with the LeCroy PCOS IV system. The spatial resolution per plane is about 700 $\mu$m.

The identical arrangement of wire planes in each of the tracking detectors was chosen to simplify the event reconstruction [Wan96], which is done by the **H**ERMES **R**econstruction **C**ode (HRC). It reconstructs the partial front and back tracks using the information from the respective drift chambers. To increase the precision of the front track, an additional point is added by projecting the back partial track to the middle of the magnet (forced bridging technique). The momenta of the particles are measured by the slope differences in the $xz$–plane between front and back tracks using a lookup–table. The achieved momentum resolution was between 0.7 and 1.25% over the entire kinematic range of the experiment [Ack98] before the installation of the RICH in the beginning of 1998 and is between 1.5 and 2.5% now [Air03b]. The uncertainty in the scattering angle is better than 0.6 mrad everywhere.

### 4.3.2 Particle Identification Detectors

One of the main features of the spectrometer is the excellent lepton–hadron separation. The efficiency to detect a lepton is above 99% with a hadron contamination of less than one percent. This is accomplished by using a certain combination of the detector responses from the **R**ing–**I**maging **Č**erenkov (RICH) counter, the **T**ransition–**R**adiation **D**etector (TRD), the preshower detector and the electromagnetic calorimeter. The RICH, designed for the separation of pions, protons and kaons, contributes to the lepton–hadron separation only for particles with energies below about 4 GeV. Since this analysis deals with particles with higher energies only, the RICH was not used and is therefore not described any further. For a detailed description see [Ako02]. For this analysis the preshower and the calorimeter are of particular importance due to their photon detection abilities.

### Transition–Radiation Detector

Transition radiation is emitted when a relativistic charged particle crosses a boundary between materials with different dielectric constants $\epsilon$. The TRD consists of six consecutive modules per spectrometer half. Each module is composed of a 6.35 cm thick radiator, loosely packed with 20 $\mu$m thin plastic fibers, and a conventional **M**ulti–**W**ire **P**roportional **C**hamber (MWPC). Each MWPC consists of 256 vertical wires at a pitch of 1.27 cm. The chambers use a gas mixture (Xe (90%), $CH_4$ (10%)) optimized for the absorption of transition radiation.

Transition radiation is emitted under an angle proportional to $1/\gamma$ where $\gamma$ is the Lorentz factor, while the mean energy of the transition radiation scales with $\gamma$. Therefore only leptons produce transition radiation of several keV (X–rays) in the kinematic range of HERMES. However, due to a Lorentz factor on the order of $10^4$ for leptons it is difficult to distinguish between the ionization signal from the charged track and the nearly collinear X–ray in the detector. Thus one has to measure the sum of the deposited energy in the detector, taking advantage of the fact that leptons ionize the gas and produce transition radiation, while hadrons loose energy via ionization only. Thus, leptons can be distinguished from hadrons since they deposit on average about twice as much energy in the TRD.

### Preshower

The preshower detector consists of the hodoscope H2, preceded by a 11 mm thick lead shield (two radiation lengths) which causes the majority of leptons and photons to produce electromagnetic showers before entering the calorimeter. The hodoscope itself consists in each detector half of 42 vertical 1 cm thick scintillator paddles with an area of $9.3 \times 91$ cm$^2$. The paddles are staggered with an overlap of 2–3 mm to avoid insensitive areas between them. Each scintillator is optically coupled via a light guide to a photomultiplier at the outside of the detector (see figure 4.4).

The lepton–hadron separation is based on the fact that leptons, in contrast to hadrons, have a very high probability to produce electromagnetic showers and thus deposit more energy in the scintillators than hadrons which mostly lose energy by ionization only. In the context of this analysis it is important to note that photons can produce electromagnetic showers as well, and thus the preshower, besides the calorimeter, is the only detector capable of detecting photons. However, it does not provide a measurement of the energy or position of the photon that is suitable for

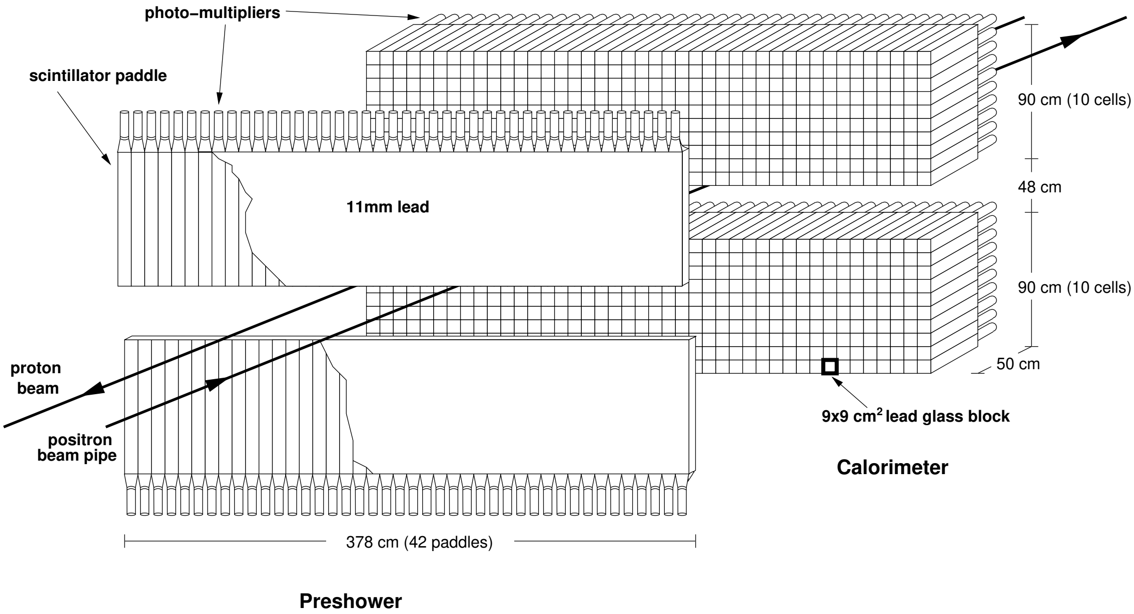


**Figure 4.4:** Schematic view of the preshower detector and the calorimeter.

analysis purposes.

### Electromagnetic Calorimeter

The electromagnetic calorimeter mainly serves as part of the trigger (see next section) and of the PID, however, it is the only detector able to measure the position and energy of the photon, and thus is the most important detector for this analysis. The calorimeter consists of 840 radiation resistant lead–glass blocks, half of them located above and half of them below the beam pipe as indicated in figure 4.4. Each half consists of an array of $42 \times 10$ blocks with a depth of 50 cm (about 18 radiation lengths) and an area of $9 \times 9$ cm$^2$. This cell size meets the requirement that for an axially incident lepton about 90% of the shower is contained in one block. The read out is accomplished by a photomultiplier at the rear end of each block. Summing up the signal in the hit block and in the eight surrounding blocks, more than 99% of the electromagnetic shower is contained in this $3 \times 3$ array which is called a cluster in the following. The energy sum $E$ in a cluster is almost independent ($< 1\%$) of variations of the hit position or of the angle of incidence of the lepton. Hadrons, in contrast to leptons, deposit only a fraction of their energy in the electromagnetic calorimeter. The lepton–hadron separation is eventually based on the ratio of the energy deposited in the calorimeter and the reconstructed momentum from tracking, which is about unity for leptons but smaller for hadrons. In order to relate a cluster from a charged particle to its corresponding track, a hit position has to be determined from the energy distribution inside a cluster. The centroid is calculated as the energy–weighted ($w_i$) average position

$$x = \frac{\sum_{i=1}^{9} x_i w_i}{\sum_{i=1}^{9} w_i}, \qquad y = \frac{\sum_{i=1}^{9} y_i w_i}{\sum_{i=1}^{9} w_i}, \tag{4.9}$$

of the nine blocks of the cluster, with the central horizontal and vertical position $x_i$ and $y_i$ of the block $i$, respectively. A square root energy weight $w_i = \sqrt{E_i}$ was used until recently, a new method [Ely01] now employed in parallel calculates the weight as $w_i = max\{0,\, 4.8 + \ln(E_i/E)\}$. Although the quality of the position reconstruction in the calorimeter is not too important for charged particles since it is only needed to match the back track to its respective cluster, it is vital for the photons since it is the only position information available. The centroid positions derived from the two different algorithms are compared in section 5.5.3.

The quality of the energy reconstruction for leptons in the calorimeter can be checked using the momentum $P$ derived from the tracking system including the spectrometer magnet. In fact, the calorimeter is calibrated by ensuring that $E/P = 1$ for leptons. There is no separate energy reconstruction method for leptons and photons, i.e., it is assumed that the shower development is at least similar. This is probably true for photons which convert into lepton pairs in the preshower and thus, like most of the leptons, start the electromagnetic shower before reaching the calorimeter. Photons which do not convert in the preshower will most likely start the shower inside the calorimeter, i.e., much later. This might lead to a reduced loss of light due to attenuation in the calorimeter and thus to an increased signal in the photomultipliers resulting in an overestimated photon energy. This behavior is reproduced using a Monte–Carlo simulation, as shown in the right panel of figure 6.1.

### 4.3.3 Trigger

The trigger initiates the readout of the detector for an event which is considered to be of interest. While a variety of triggers exists for different physics studies, only two of them are used in this analysis and will be explained in the following. The main physics trigger (trigger–21) should start the readout if a candidate DIS event took place. An event is considered a candidate DIS event, if the scattered lepton traverses one full detector half including detection in the calorimeter with an energy above a preset threshold. For a fast decision on the particle type and trajectory, the hodoscopes H0 and H1 are used in coincidence with the preshower and the calorimeter. The latter two detectors were already described in the last section. The H0 is located in the front region of the spectrometer (see figure 4.3) and consists of only one scintillator paddle in each detector half, read out by two photomultipliers. The hodoscope H1 is placed right in front of the TRD in the back region of the spectrometer. It is made the same way as the preshower hodoscope H2 described above.

Trigger–21 requires the following conditions:

- A signal in H0.
- A signal in H1.
- A signal above the minimum ionizing signal in the preshower to indicate passage of a lepton.
- The sum of the signals in two neighboring calorimeter columns has to be above a certain threshold. The data used in this analysis was collected with a threshold of 3.5 GeV. This provides a good lepton–hadron separation since only a minority of the hadrons has an energy large enough to be able to deposit the required energy in the calorimeter.
- All signals have to arrive in coincidence with the bunch crossing signal from the accelerator. In addition, particles originating from the HERA proton beam and thus entering the spectrometer from the rear are excluded by timing restrictions since they would hit H0 last.

Except for a signal in H0, trigger–18 has the same requirements as trigger–21 and therefore is used in this analysis to determine possible inefficiencies in the H0 detector (see chapter 5.5.1).

### 4.3.4 Luminosity Monitor

The luminosity measurement is based on elastic scattering of beam positrons off target gas electrons (Bhabha scattering) and their annihilation into photon pairs, or on Møller scattering ($e^-e^- \to e^-e^-$) in the case of an electron beam. The luminosity monitor [Ben01] consists of two small calorimeters, mounted symmetrically to the left and right of the beam pipe at a distance of 7.2 m downstream from the target (see figure 4.3). Each calorimeter is built of 12 Čerenkov crystals with a size of $22 \times 22 \times 200$ mm$^3$ arranged in a $3 \times 4$ matrix. Since the calorimeter is mounted close to the beam pipe it experiences a high radiation background, therefore the same radiation hard $NaBi(WO_4)_2$ crystals as in the case of the LPOL are used. Each crystal is read out separately by a photomultiplier. To suppress the detection of background events, coincident signals from both calorimeters are required with an energy threshold of 4.5 GeV in each of them. The absolute luminosity is then given by the measured coincidence rate times the luminosity constant. The latter is obtained from the precisely known Bhabha or Møller cross sections with the knowledge of the detector efficiency and acceptance. The systematic error of the luminosity constant is on the order of 7–8% [Els02] for data taken with a positron beam, but for the running period with an electron beam (1998) an additional systematic uncertainty of 10% [Els03] arises due to the not perfectly simulated cross section ratio between electron and positron beam.

# Chapter 5

# Data Treatment

In order to describe the extraction of the event samples for the following analysis, the HERMES data structure and the various selection criteria applied to the data are explained below. Checks on the quality and consistency of the event samples are performed. Discrepancies found are accounted for, either via rejecting parts of the data or carrying out corrections if possible.

## 5.1 Data Structure and Production

HERMES data sets are divided into fills, runs and bursts. A fill denotes the time period in which the measurement uses the same filling of the HERA lepton ring. It lasts typically 8–14 hours. After a trigger occurs during the measurement, the data acquisition system translates the response from all detectors into a digital form and stores it in a file on a hard disk. A file size of 500 MB determines a run which is typically achieved after 10–30 minutes of data taking depending on the event rate. Every 10 seconds the so–called slow–control data is read out. This arbitrarily chosen time period defines a burst. Slow–control data is not related to a single event but to the performance of the beam, the target, and the detectors which change on a longer time scale.

After a run is completed the file is copied to the DESY tape robot and processed through several programs in order to convert the raw data written in the **E**xperimental **P**hysics **I**nput **O**utput (EPIO) format into useful physics quantities. The **H**ERMES **D**e**C**oder (HDC) is first in line. With the knowledge of the design of the subdetectors and specific mapping and calibration files the HDC program decodes the EPIO files into specific quantities for each subdetector, e.g., hit positions in wiremaps, energy depositions or timing information. The output format is based on the tabular structure of the **A**leph **DA**ta **MO**del (ADAMO) database and the output file is directly sent into the **H**ERMES **R**e**C**onstruction (HRC) program. This program combines the individual detector responses in conjunction with alignment and calibration information in order to reconstruct trajectories in the spectrometer and clusters in the calorimeter, as already explained in section 4.3.1 and section 4.3.2, respectively. The slow–control data, on the other hand, is combined with external data provided by the experts of the detector subsystems, into a single slow–control data file for each fill. In a last step all data relevant for physics analysis are calculated from the HRC output and the slow–control files and merged into a single file for each run, the so–called micro–**D**ata **S**ummary **T**ape ($\mu$DST). These files are usually the ones used for the analysis. This reconstruction chain is iterated at least once since the majority of the calibration and alignment input data is calculated from the actual data.

## 5.2 Data Sample

In order to extract the beam–charge asymmetry measurements with electron and positron beams have to be used. The only available data taken with an electron beam stems from a short running period in 1998. The measurements on hydrogen amount to an integrated luminosity of about 11 pb$^{-1}$. In all other years HERA was using a positron beam. The unpolarized and spin–averaged polarized hydrogen data from 1996/1997, used for the already published beam–spin asymmetry (see section 3.4.2), corresponds to an integrated luminosity of 108 pb$^{-1}$. In 1999 very little data (0.2 pb$^{-1}$) was taken on a hydrogen target. The very successful year 2000 yielded 150 pb$^{-1}$ on unpolarized hydrogen. All available data on hydrogen can be used for this analysis. Still, the statistical error will be dominated by the electron sample.

The installation of the RICH between the 1997 and 1998 running periods resulted in a degradation of the HERMES spectrometer charged–particle reconstruction resolution (see section 4.3.1). This difference in resolution between the 1998 electron sample and the 1996/97 positron sample leads to different signal–to–background ratios and different yields in the final event samples of the two running periods [Ell02a], and thus to additional systematic uncertainties. Details on the latter can be found in the context of the calorimeter calibration (see section 7.2.4), where similar systematic uncertainties emerge due to differences in the reconstruction of the photon energy. Consequently, only the data samples from 1998 and 2000 will be used in this analysis. They have been reproduced including corrections to already identified problems [Ell02a] and the new photon position reconstruction algorithm (see section 4.3.2). Both $\mu$DST productions (Release 98d0 and 00c1) have been produced in an identical way and therefore can be treated identically. The DVCs were omitted in the reconstruction of the front partial tracks in these productions, i.e., the only information about the front tracks stems from the FCs. This directly implies that the forced bridging technique as explained in section 4.3.1 was used.

## 5.3 Data Quality

The decision whether accumulated data is of sufficient quality to be used for analysis purposes or not is done on the run and burst level. On the run level the notes in the electronic logbook made by the people on shift during data taking are taken into account. On the burst level the slow–control data is used.

For the $\mu$DST productions 98d0 and 00c1 the following general criteria were used to select runs:

- the target was unpolarized hydrogen
- the run was marked as analyzable in the electronic logbook

At the burst–level, the following data–quality cuts were applied:

- there were no HV trips in the FCs and BCs
- there were no dead blocks in the calorimeter or luminosity monitor
- there were no dead paddles in the hodoscopes
- the TRD was functioning during the burst
- the burst was longer than 8 seconds
- the beam current was reasonable (5 mA $< I <$ 50 mA)
- the last measurement of the beam polarization was less than 300 seconds ago
- the live time for Trigger–21 was greater than 0.8
- the burst was not the first or last burst in a run
- the PID calculation was performed

For the extraction of the beam–spin asymmetry a lower limit of 0.4 is placed on the beam polarization.

## 5.4 Event Selection and Data Consistency Checks

Since with the present HERMES spectrometer the recoiling proton in the DVCS process cannot be detected, only the scattered beam lepton and the produced real photon can be reconstructed in an event. In a first step, the events where the scattered lepton can be identified within certain kinematic boundaries are selected. The number of these so–called DIS events has to be counted for normalization purposes. In a second step DIS, events are selected if they have exactly one charged track, i.e., the scattered lepton, and exactly one photon fulfilling certain constraints. These events are called single–photon events. The third sample consists of the single–photon events which are likely to be produced exclusively, i.e., as described by expression 3.1, and are therefore called exclusive events.

### 5.4.1 DIS Events

Events triggered by trigger–21 and containing at least one charged track as reconstructed by HRC are called DIS events if at least one charged track meets the following requirements. The track traverses one full spectrometer half and produces a signal in the calorimeter, i.e., it is not bent out of the acceptance by the spectrometer magnet. A projection of the back track, as given by the BCs, to the position of the calorimeter satisfies the fiducial constraints $|x_{calo}| < 175$ cm and 30 cm $< |y_{calo}| < 108$ cm. This corresponds to the track not being incident in the outermost 2/3 of the outer row or column of calorimeter blocks. Otherwise the energy might leak out of the sides of the calorimeter, thus leading to a wrong reconstruction. A correct energy reconstruction in the calorimeter is necessary for the PID system described in section 4.3.2 which must identify the track as a lepton in this case. As already mentioned, the RICH is not beneficial for the particle identification in this analysis and thus only the response of the other three PID detectors is taken into account. The combined response from preshower and calorimeter (PID2) and the response of the TRD (PID5) was chosen to satisfy the requirement $PID2 + PID5 > 2$. This corresponds to the track being at least $10^2$ times more likely a lepton than a hadron. In addition, the track has to be negatively (1998 data) or positively (2000 data) charged. The vertex, as calculated by HRC, is the point of closest approach of the track to the beam. The vertex should be well inside the target cell in the longitudinal direction, i.e., $-18$ cm$< z_{vertex} < 18$ cm, and in the transverse direction, i.e., $t_{vertex} < 0.75$ cm.

The detection of the scattered lepton allows for the calculation of the so–called inclusive variables (equations 3.2–3.6), i.e., the variables that can be calculated with the detection of the scattered lepton only. It has already been discussed in chapter 2 that $Q^2$ should be large compared to the mass of the final hadronic state in order to be in the hard scattering regime where factorization is valid. Since the final hadronic state is a proton, $Q^2 >> 1$ GeV$^2$ would be required. On the other hand, statistics are limited for large values of $Q^2$. The data therefore is constrained to $Q^2 > 1$ GeV$^2$, knowing that this possibly leads to difficulties in the interpretation of the data, as will be discussed in section 9.2. The squared invariant mass of the photon–nucleon system $W^2$ is required to be above 9 GeV$^2$. Although it will be shown later on in figure 5.6 that the exclusive sample satisfies $W^2 > 9$ GeV$^2$ anyway, this constraint is nevertheless important since it restricts the data to the deeply–inelastic regime where the fragmentation model of the Monte Carlo is believed to work, i.e., it makes the comparison between Monte Carlo and data in the next chapter more reliable.

Applying these constraints to the data sets from 1998 and 2000 and normalizing each of them to unity, consistency checks can be carried out for different variables. The two data samples agree quite well for most of the variables. As an example, the distributions of the lepton vertices $z_{vertex}$ along the beam axis ($z$-axis) are shown for the two samples in the left panel of figure 5.1. The distributions agree perfectly and show the expected triangular shape, consistent with the density of the target gas in the target cell when injecting the gas at $z = 0$ cm. Disagreement between the two data sets has been found for two variables. The lepton vertex distributions perpendicular to the beam axis are compared in the middle panel of figure 5.1. The vertices of the 2000 data are in general closer to the nominal beam position than the ones from 1998. This is due to the fact that the beam positions differed more from fill to fill in 1998 than in 2000. However, the difference between the two distributions is small compared to the width of the distributions which is the relevant quantity concerning possible resolution issues in the reconstruction of the opening angle $\theta_{\gamma^*\gamma}$ and the azimuthal angle $\phi$, as will be explained in the next section. The observation that both distributions do not have their maximum at the expected value of $t_{vertex} = 0$ cm, i.e., in the center of the target, is believed to be due to small misalignments of the top and bottom part of the detector, for which presently no final analysis results are available at HERMES.

The distributions of the energy transfer $\nu$ from the incoming lepton to the virtual photon are compared in the right panel of figure 5.1. They are already restricted to be smaller than about 24 GeV due to the trigger threshold of 3.5 GeV for the lepton in the calorimeter, as explained in section 4.3.3. However, no sharp cutoff can be observed at $\nu = 24$ GeV and for the two running periods the yield is not quite the same above $\nu = 22$ GeV, as indicated by the vertical line. This implies

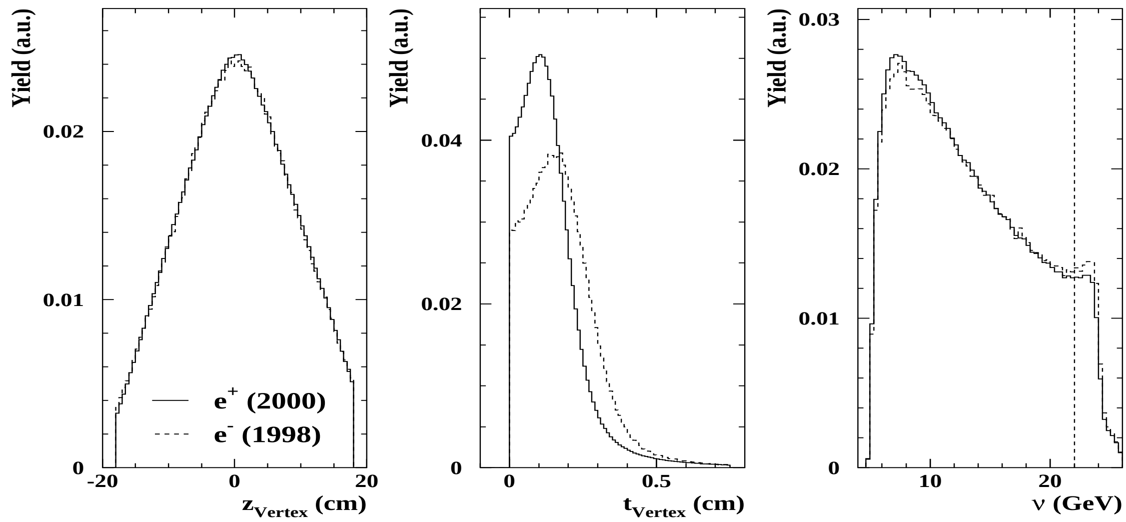


**Figure 5.1:** Distributions of DIS event samples from the years 2000 (solid lines) and 1998 (dashed lines) for the vertex position in the longitudinal direction $z_{vertex}$, in the transverse direction $t_{vertex}$ and for the energy of the virtual photon $\nu$. The data sets are normalized to unity.

---

that the efficiency of the calorimeter threshold was different for the two years. In order to avoid normalization problems, $\nu < 22$ GeV is required in the following to ensure that the lepton was well above the 3.5 GeV threshold. As will be shown in figure 5.6, this cut basically does not affect the exclusive data sample. Note that a correct normalization of the exclusive event sample to the number of DIS events is mandatory for an extraction of the beam–charge asymmetry, but not for an extraction of the beam–spin asymmetry (see section 7.1.2).

### 5.4.2 Single–Photon Events

From the sample of DIS events, only those with exactly one charged track, i.e., the scattered lepton, are taken into account in the following. In addition, exactly one cluster in the calorimeter with no track assigned to it, a so–called trackless cluster, is required. In order that this cluster is accepted as a photon in this analysis, a signal in the preshower detector $E_{pre} > 1$ MeV is required since photons not converting in the preshower are reconstructed with too large energies. This was explained in section 4.3.2 and is displayed in figure 6.1, obtained from a Monte–Carlo simulation. Up to now, no method has been found to reliably correct for this effect [Ell01b] and hence this part of the data ($\approx 15\%$) is not used.

The energy of the real photon $E_\gamma$ is required to be above 3 GeV. This is driven by the fact that the Monte–Carlo simulation does not describe the data for photons with lower energies (see section 6.3). As will be shown below, all photons in the exclusive sample have energies above 3 GeV, so this cut does not sacrifice any valuable data. Note that the photon energy given in the $\mu$DSTs is not multiplied by a factor of 0.97 as usually done in HERMES analyses, e.g., for the reconstruction of $\pi^0$ mesons. This factor has been found to account for the effect that the photon energy is on average reconstructed with a too large value since non–converting photons are used as well [Ell01b].

The photon needs to be in the fiducial volume of the calorimeter for photons, $|x_{calo}| < 125$ cm and 33 cm $< |y_{calo}| < 105$ cm. The constraint in the $y$–direction prevents photons from being incident in the outermost row of calorimeter blocks where the shower is not anymore fully contained in the calorimeter and its energy gets incorrectly reconstructed. The constraint in the $x$–direction is given by the acceptance of the spectrometer magnet for neutral particles coming from the target.

For photons satisfying the above constraints the Mandelstam invariant $t$ can be calculated according to equation 3.7 with the virtual and real photon four–momenta $q$ and $q'$, respectively. The angle between the virtual and the real photon $\theta_{\gamma^*\gamma}$ is given as:

$$\theta_{\gamma^*\gamma} = \arccos\left(\frac{\vec{q}\cdot\vec{q'}}{|\vec{q}||\vec{q'}|}\right). \tag{5.1}$$

The azimuthal angle

$$\phi = \arccos\left(\frac{(\vec{q}\times\vec{k})(\vec{q}\times\vec{q'})}{|\vec{q}\times\vec{k}||\vec{q}\times\vec{q'}|}\right)\frac{\vec{q'}\cdot\vec{q}\times\vec{k}}{|\vec{q'}\cdot\vec{q}\times\vec{k}|} \tag{5.2}$$

can be calculated with the momentum $\vec{k}$ of the incoming lepton.

Applying all constraints, single–photon samples have been extracted for the 1998 and the 2000 data and normalized to their respective number of DIS events. The agreement between the two data sets (not shown) for the variables derived from the outgoing lepton kinematics (inclusive variables) is quite good. The distributions for the variables calculated via the outgoing photon kinematics are given in figure 5.2. A lower limit needs to be placed on the opening angle $\theta_{\gamma^*\gamma}$ since the azimuthal angle $\phi$ is not defined at $\theta_{\gamma^*\gamma} = 0$ mrad. Consequently, it should be calculated only in a region where the opening angle $\theta_{\gamma^*\gamma}$ is non–zero within its resolution. The latter is dominated by the position resolution of photons in the calorimeter which turns out to be about 0.6 mrad when applying certain corrections, as explained in section 5.5.3. Taking into account additional contributions, in particular the width of the

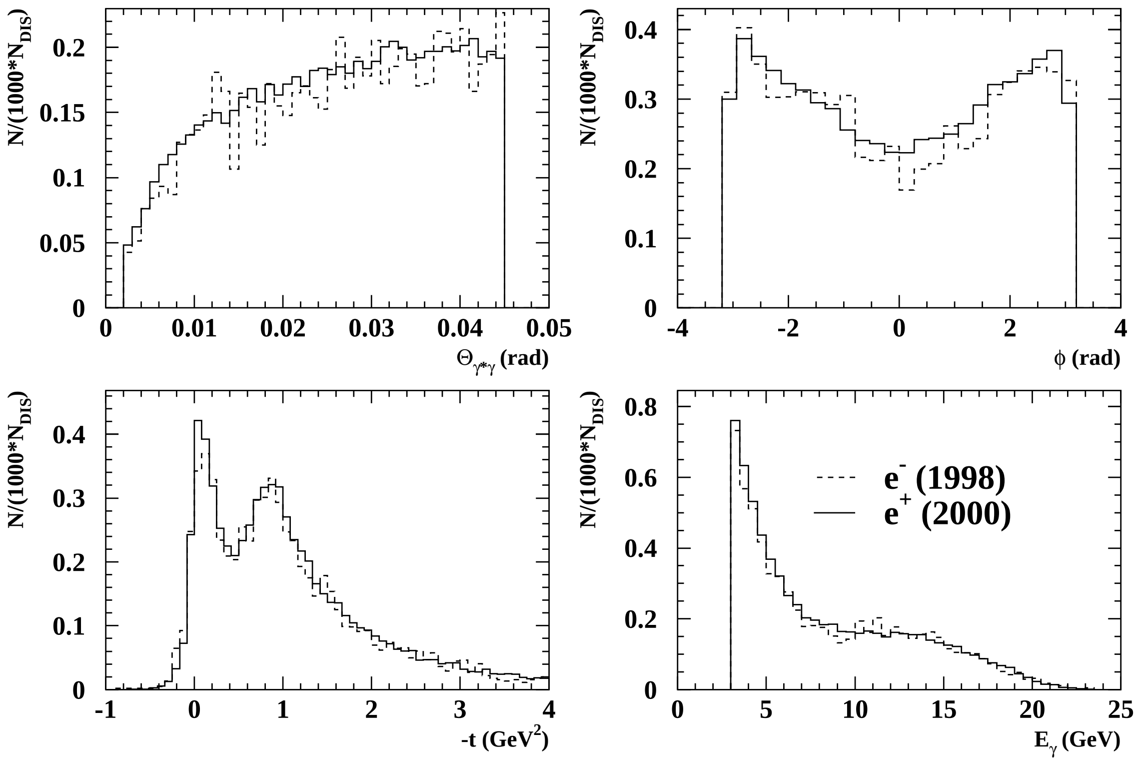


**Figure 5.2:** Distributions of the single–photon event yields per 1000 DIS events for the data from the years 2000 (solid lines) and 1998 (dashed lines) for different variables.

$t_{vertex}$ distribution in figure 5.1, a safe lower limit of 2 mrad can be placed on the opening angle $\theta_{\gamma^*\gamma}$. There is not much data below this value, as shown in the upper left panel of figure 5.2. Note that the previously used lower limit was 15 mrad and the upper limit was 70 mrad (see section 3.4.2). Based on Monte Carlo studies the latter value is decreased to 45 mrad as indicated in the figure, because beyond this point the exclusive event sample contains more background than signal events (see section 6.5). With these limits on the opening angle, the resulting distributions on the azimuthal angle are shown in the upper right panel of the same figure. The influence of the upper $\theta_{\gamma^*\gamma}$ limit on the shape of the $\phi$ distribution will be discussed in the next section.

The $-t$ distribution in the lower left panel of figure 5.2 offers a possibility to distinguish exclusive and non–exclusive processes. Exclusive processes have vanishing momentum transfer, i.e., the peak at $-t \approx 0$ mostly contains exclusive events. Events with $-t > 0.5$ GeV$^2$ are mostly semi–inclusive. These photons predominantly originate from the decay of $\pi^0$ and $\eta$. Their largest fraction comes from the

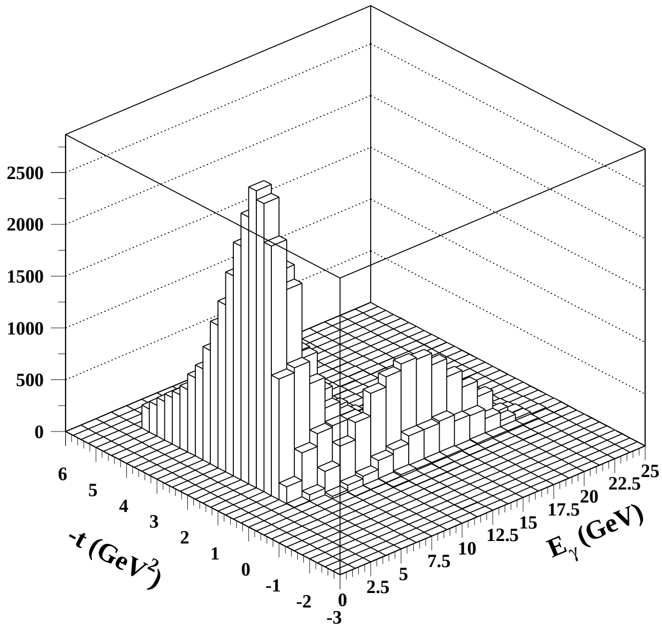


**Figure 5.3:** Correlation between the energy of the photons $E_\gamma$ and the four–momentum transfer squared $-t$ in the single–photon event sample.

---

decay of the $\pi^0$ with one of the two decay photons remaining undetected, usually due to the fact that it is not within the geometrical acceptance of the HERMES spectrometer. In addition, photons with energies below 0.5 GeV are not detected anymore and in the case that the photons are separated by less than about 10 cm at the calorimeter position they are reconstructed by HRC as only one cluster.

The distributions of the photon energy $E_\gamma$, shown in the lower right panel of figure 5.2, are largely dominated by low energetic photons. It has already been claimed above that the imposed constraint $E_\gamma > 3$ GeV does not reject valuable data. This is illustrated in figure 5.3 where the correlation between $-t$ and $E_\gamma$ is shown. Low energetic photons appear mostly at high values of $-t$ and vice versa. Hence an upper limit on $-t$ of 0.5 GeV$^2$ would lead to a predominantly exclusive sample with high energetic photons. However, Monte Carlo studies described in section 6.5 reveal that another method of extracting the exclusive sample is advantageous in terms of an optimized signal–to–background ratio. It is described in the following.

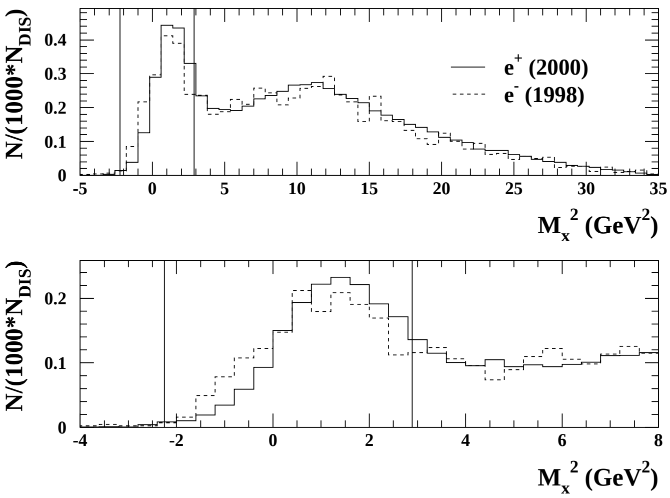


**Figure 5.4:** Missing mass squared distributions in the full kinematic range (upper panel) and in the small $M_x^2$ region (lower panel) from the years 2000 (solid lines) and 1998 (dashed lines). The vertical lines indicate the exclusive bin. The data sets are normalized to the respective number of DIS events.

---

### 5.4.3 Exclusive Events

In the last step of the event selection the single–photon event sample has to be reduced to a sample with predominantly exclusively produced photons. Since the recoiling nucleon cannot be detected at HERMES, missing mass techniques have to be employed. For scattering on hydrogen, the missing mass should then be equal to the proton mass $M_p$ if the proton stays intact and the photon is the only particle produced. Otherwise the process exhibits a higher missing mass. The missing mass squared

$$M_x^2 = (q + p - q')^2, \tag{5.3}$$

with $q$, $p$ and $q'$ being the four–momenta of the virtual photon, the target nucleon and the real photon, respectively, is calculated for every single–photon event. Its distribution for both data sets is shown in figure 5.4. Due to the limited photon resolution of the HERMES spectrometer (see section 6.4) the exclusive peak is quite broad and even extends to negative values in which case $M_x = -\sqrt{-M_x^2}$ is defined. For the data from 1998 the bottom plot shows a clear peak at about the correct position, i.e., at $M_p^2$. The distribution from the 2000 data appears to be shifted against the one from the 1998 data. While the shift is small for large values of $M_x^2$ it gets sizeable when approaching the exclusive region. This points to incorrectly reconstructed photon energies since high values of $M_x^2$ correspond to low photon energies and vice versa, i.e., the effect becomes visible in the exclusive region where the photons have higher energies on average. For the two data sets, this leads to different signal–to–background ratios and to different yields in the small $M_x^2$ region and thus to additional systematic uncertainties in the asymmetry extraction (see section 7.2.4). For the same reason the hydrogen data from 1996/97 was discarded from this analysis, as described in section 5.2. However, in contrast to the there explained difference in the lepton resolution between the two running periods, this difference in the photon energy reconstruction can be checked and adjusted accordingly, as will be explained in section 5.5.2.

In order to define the exclusive sample, the missing mass constraint of -1.5 GeV $< M_x <$ 1.7 GeV used in the earlier analysis (see section 3.4.2) is used for this analysis as well. The size of this exclusive bin is indicated by vertical lines in figure 5.4. Due to the worse lepton resolution of the data sets used here compared to those from 1996/97 (see section 4.3.1), the non-exclusive contribution to this exclusive bin might be bigger. In the first place this could lead to a slightly reduced, i.e., diluted, measured beam–spin asymmetry as compared to the published result. However, in contrast to the published result, the asymmetry will be corrected for the non–exclusive background contribution in this analysis instead of treating it as a systematic error. Then, the asymmetry is expected to be largely insensitive to the size of the exclusive bin as long as the non–exclusive contribution is known. Moreover, based on Monte Carlo studies it will be shown in section 6.5 that this rather arbitrarily chosen size of the exclusive bin is actually reasonable in terms of signal–to–background optimizations.

As already mentioned, an upper limit of 70 mrad on the opening angle $\theta_{\gamma^*\gamma}$ was introduced in the earlier analysis in order to restrict the exclusive sample to a region with full $\phi$ coverage (see section 3.4.2). This is illustrated in figure 5.5 showing the azimuthal angle $\phi$ versus the opening angle $\theta_{\gamma^*\gamma}$. Full acceptance in $\phi$ exists only below $\theta_{\gamma^*\gamma}$ = 70 mrad. Above this value most of the events are centered around $\phi = 0$ and azimuthal asymmetries cannot be reasonably calculated anymore. The new upper limit of 45 mrad introduced in the previous section fulfills the requirement of full acceptance in $\phi$ even better.

In figure 5.6 the exclusive samples from the two data sets are shown for the different variables. As expected, the $Q^2$ distributions have their maximum yield at $Q^2$ = 1 GeV$^2$ with a quick falloff towards higher values of $Q^2$. The $x_B$ distributions display the kinematic range of this variable accessible at HERMES. The $W^2$ and $\nu$ distributions confirm that the imposed constraints of $W^2 >$ 9 GeV$^2$ and $\nu <$ 22 GeV basically do not affect the exclusive sample. The same holds true for the $E_\gamma >$ 3 GeV

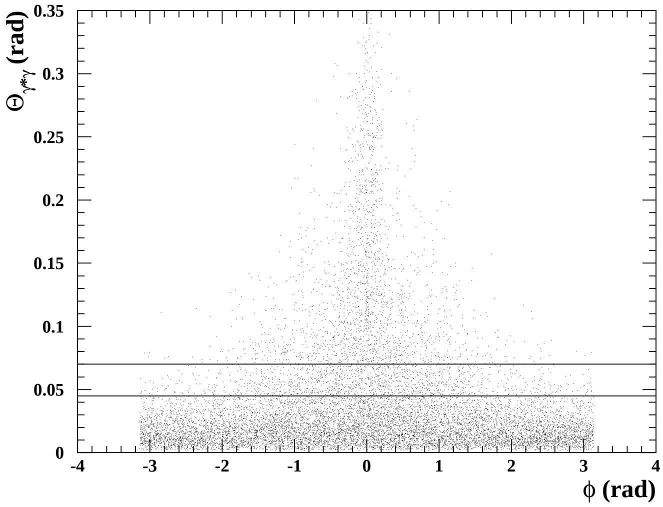


**Figure 5.5:** Scatter plot of the azimuthal angle $\phi$ versus the opening angle $\theta_{\gamma^*\gamma}$ for exclusive events. The horizontal lines mark the old (new) upper limit of 70 mrad (45 mrad) on the opening angle $\theta_{\gamma^*\gamma}$.

requirement. A comparison between the $E_\gamma$ and $-t$ distributions in the exclusive sample (this figure) and in the single–photon sample (figure 5.2) shows that indeed only high energetic photons with the corresponding small values of $-t$ survive in the exclusive sample, as already discussed above. Comparing the $\theta_{\gamma^*\gamma}$ distributions from the exclusive and the single–photon sample it becomes obvious that the exclusive events are peaked at small values of $\theta_{\gamma^*\gamma}$. This distribution proves that considerable statistics is gained when using the lower limit of 2 mrad on $\theta_{\gamma^*\gamma}$ in contrast to the limit of 15 mrad used in the earlier analysis. The variable $-t_c$ will be introduced later on in section 6.4, but the $-t_c$ distributions are already shown here for completeness.

## 5.5 Corrections to the Data

Correction algorithms applied to the data used in this analysis are explained in the following. They account for trigger inefficiencies and improve the energy and position reconstruction of photons in the calorimeter.

### 5.5.1 H0 Inefficiency Correction

It has been shown [DeN01] that inefficiencies of the H0 scintillator array lead to a reduced trigger–21 efficiency in 1998. If this trigger inefficiency is not uniformly

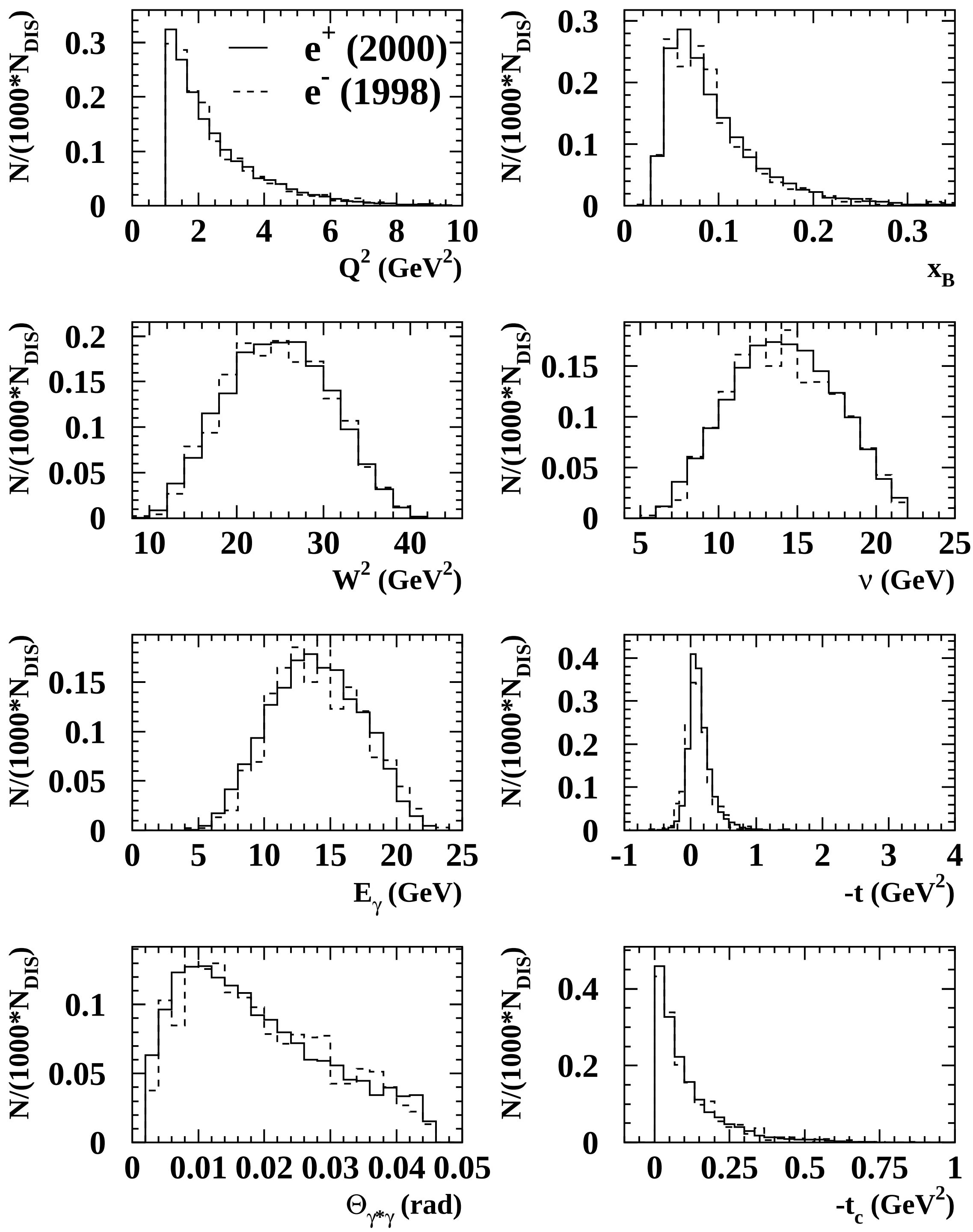


**Figure 5.6:** Distributions of the exclusive events from the years 2000 (solid lines) and 1998 (dashed lines) for different variables. The data sets are normalized to the respective number of DIS events. Note that the variable $t_c$ (lower right panel) will be introduced later on in section 6.4.

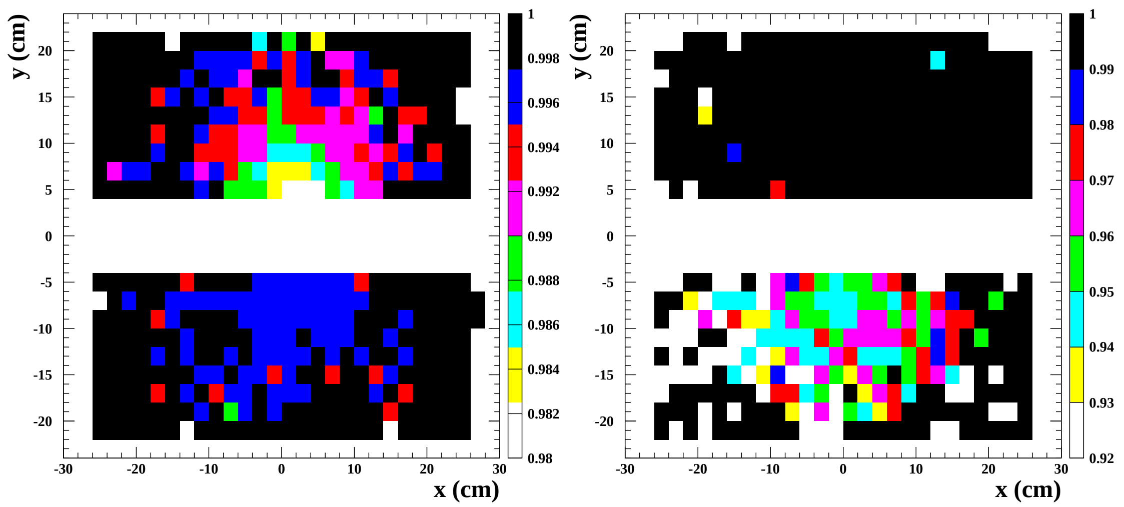


**Figure 5.7:** H0 efficiency for the 2000 data (left panel) and for the 1998 data (right panel) plotted as a grid of 2 cm by 2 cm cells across the H0 scintillator plane.

distributed over the HERMES acceptance or, even worse, if it is different for the 2000 data set, it may bias the angular distributions from which the azimuthal asymmetries have to be extracted. The effect might be particularly strong for this analysis since the event sample consists of events with one charged track only. In this case the signal in H0 has to originate from the DIS lepton itself, while in events with two or more charged tracks the signal might stem from one of the accompanying particles as well, i.e., these inefficiencies decrease with higher event multiplicities. Accordingly, the trigger–21 efficiency is calculated using the full one–track DIS event sample. Since the only difference between trigger–18 and trigger–21 is the required signal in H0, as explained in section 4.3.3, the H0 efficiency is given by the ratio of trigger–18 events with and without trigger–21. Although the trigger–18 events were prescaled, there remained sufficient statistics to calculate the H0 efficiency for a grid of 2 cm by 2 cm cells across the H0 scintillator plane using the lepton tracks that passed trigger–18. The result in figure 5.7 shows that the H0 inefficiency in 2000 (left panel) is centered around the beam pipe in the top half of the spectrometer, while in 1998 (right panel) mostly the bottom part was affected. The efficiency in these areas goes down to values of about 98% in the year 2000 and of about 92% in the year 1998. Thus in this analysis every single–photon event in both data sets is weighted with the inverse of the efficiency in the respective 2 cm by 2 cm cell the DIS lepton passed through. This method artificially restores uniform acceptance for the DIS lepton.

The correction for the H0 inefficiency needs also to be carried out for the usual DIS

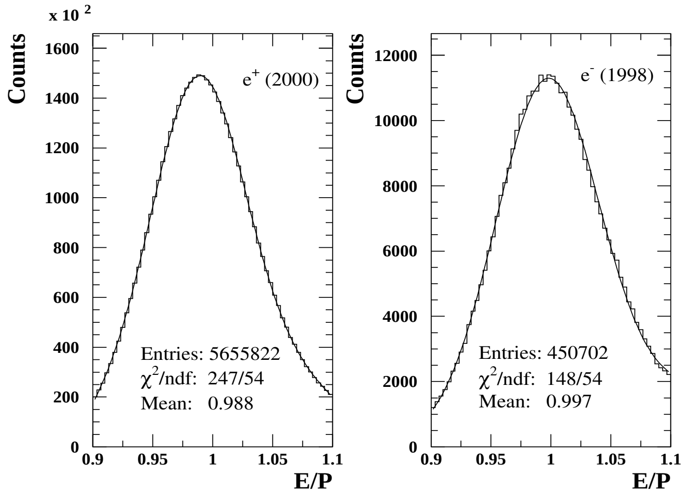


**Figure 5.8:** Distributions of the ratio between the lepton energy deposited in the calorimeter $E$ and the momentum of the lepton $P$, as derived from the $x$–slope difference between the front and the back track, for the 2000 (left panel) and the 1998 (right panel) data set.

---

event sample, as derived in section 5.4.1, since it is used for normalization purposes. The overall efficiency for the H0 scintillator plane is calculated using the usual DIS sample and the number of DIS events is then accordingly weighted by the inverse of this efficiency.

### 5.5.2 Photon Energy Reconstruction Correction

It has been shown in figure 5.4 that the missing mass squared distributions from the 1998 and 2000 data sets appear to be shifted against each other, especially in the exclusive region. A difference in the photon energy reconstruction for the two running periods was identified as a possible reason for this behavior (see section 5.4.3). Although no method has been found to reliably check the quality of the photon energy reconstruction in the high energy region, a relative shift between the two data sets can be identified. This is done using the ratio between the lepton energy deposited in the calorimeter $E$ and the momentum of the lepton $P$, as derived from the $x$–slope difference between the front and the back track. The distributions for the value $E/P$ for the full DIS sample are shown in figure 5.8 for both data sets. A fit to a Gaussian distribution plus a second order polynomial gives a mean value for the 1998 data set close to one, while the 2000 data shows an about 1% smaller value. This implies that the calibration of the calorimeter was not perfect for the 2000 data. Accordingly, the energy of a photon in the 2000 data set, as

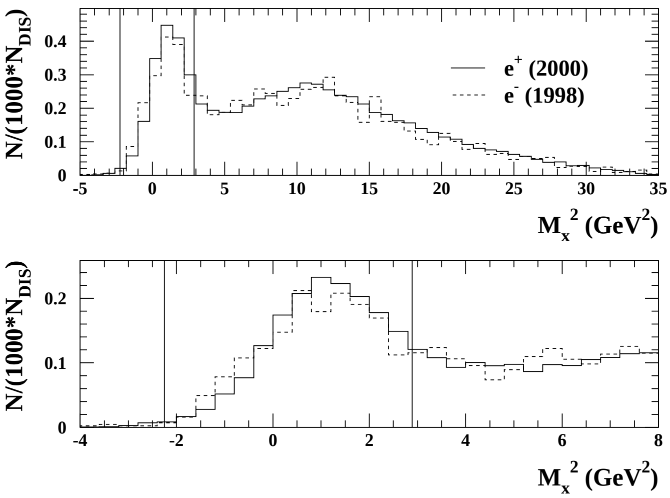


**Figure 5.9:** Missing mass squared distributions in the full kinematic range (upper panel) and in the small $M_x^2$ region (lower panel) from the years 2000 (solid lines) and 1998 (dashed lines) after applying the photon energy reconstruction correction. The vertical lines indicate the exclusive bin. The data sets are normalized to the respective number of DIS events.

---

given in the $\mu$DST–files, is increased by 1% in this analysis. Figure 5.9 shows again the missing mass squared distribution for the two data sets, but this time with the corrected photon energy values for the data from 2000. The agreement between the data sets is much better when compared to figure 5.4, especially in the exclusive region displayed in the lower panel.

### 5.5.3 Photon Position Reconstruction Correction

The quality of the position reconstruction of the calorimeter cannot be checked directly for photons since there is no other device which provides an independent measurement. However, the reconstructed cluster position for charged tracks, e.g., leptons, can be used instead. In contrast to the $\mu$DSTs, the output files of the HRC program still contain this information. An analysis on these files provides the possibility to compare the result given by the calorimeter to the result given by the BCs, when extrapolating the back–track to the position of the calorimeter. Since the HRC output files do not contain the calculated PID values a lepton sample has been identified by applying constraints on the PID detectors separately. The deposited energy in the preshower is required to be above 30 MeV and the signal in the TRD has to exceed 26 keV. In addition, the same fiducial volume constraints and the constraints

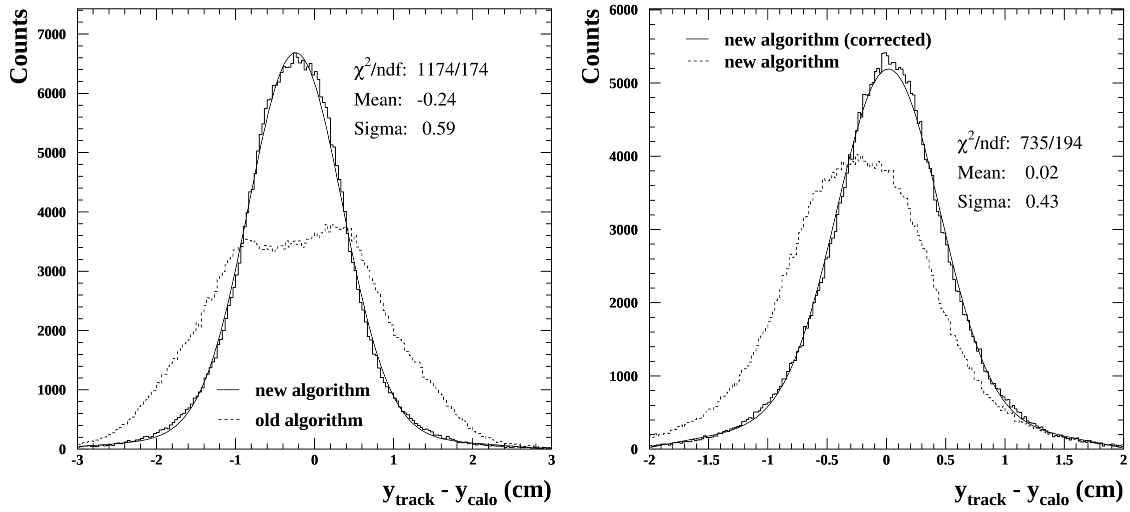


**Figure 5.10:** Difference between the reconstructed lepton $y$–position at the position of the calorimeter derived from the tracking system $y_{track}$ and the calorimeter $y_{calo}$ for the old and the new position reconstruction algorithm (left panel) and for the new one with and without additional corrections applied (right panel), as described in the text. Note the different abscissa scales used.

---

on the reconstructed vertex position as explained in section 5.4.1 are applied. In the left panel of figure 5.10 the difference between the reconstructed positions in the $y$–direction given by the tracking chambers $y_{track}$ and by the calorimeter $y_{calo}$ is shown for two different position reconstruction algorithms. The new algorithm (solid line) for the reconstruction of the cluster position in the calorimeter (see section 4.3.2) has been implemented for the production of this data set for the first time. The old algorithm (dashed line) shows the problem that photons which are not incident in the center of a certain calorimeter block are reconstructed with a shift to the center of the block, i.e., photons incident in the top of a block are reconstructed slightly lower and photons incident in the bottom slightly higher. This explains the two peak structure observed in the figure when using the old algorithm. The new algorithm does not show this behavior and thus is the one used in the following. The position reconstruction in the $x$–direction (not shown) has been checked as well. The same behavior is found.

An important quantity for this analysis is the resolution of the position reconstruction of the calorimeter. The width of the distribution achieved with the new algorithm displayed in the left panel of figure 5.10 should provide a good estimate for the resolution since the width of the resolution of the tracking system is small

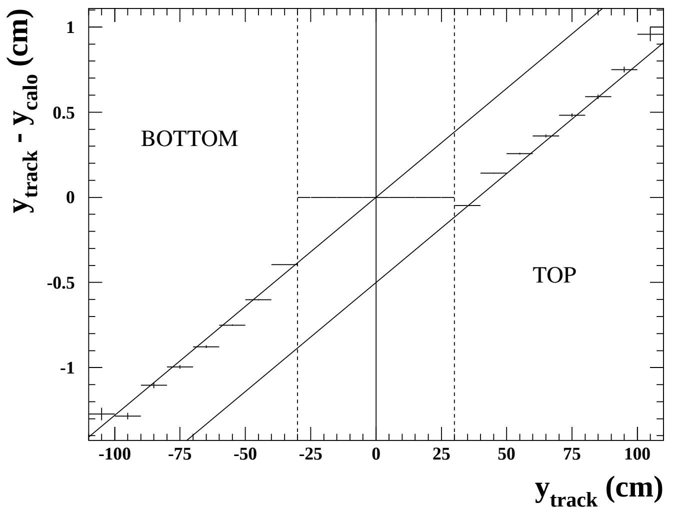


**Figure 5.11:** Difference between the reconstructed lepton $y$–position at the position of the calorimeter derived from the tracking system $y_{track}$ and the calorimeter $y_{calo}$ as a function of the reconstructed position in the $y$–direction.

---

compared to the one of the calorimeter. A fit to a Gaussian plus a second order polynomial results in a sigma of about 0.6 cm which corresponds to a resolution of about 0.8 mrad. A fit for the $x$–direction yields a similar value.

However, while the mean of the peak is expected at zero and indeed is about zero for the $x$–direction, it appears to have an 2.5 mm offset in the $y$–direction, as shown in the same figure. Investigating the difference $y_{track} - y_{calo}$ separately for the top and the bottom part of the calorimeter (not shown) reveals that the mean of this distribution in the top part is about zero while it is about -5 mm in the bottom part. Taking into account that the reconstructed position in the calorimeter might depend on the incident angle of the lepton and therefore on the reconstructed position itself, figure 5.11 shows the mean value of the difference $y_{track} - y_{calo}$ as a function of the reconstructed position in the $y$–direction. On the abscissa, negative (positive) values of $y_{track}$ correspond to the bottom (top) part of the calorimeter. The area between the two dashed lines is the area outside the fiducial volume for leptons. The solid line that fits the data in the bottom part of the calorimeter shows the dependence of the reconstructed position on the actual position. It is zero for the extrapolated position $y_{track} = 0$ cm, i.e., leptons which would be incident under 90° would not have any offset, as expected. This indicates that the tracking system and the bottom part of the calorimeter are well aligned and that the above observed offset of -5 mm between both is just due to the fact that the average incident angle in the bottom calorimeter is non–zero. The solid line that fits the data in the top part has the same slope as the one in the bottom part but it is shifted by -5 mm, i.e., at $y_{track} = 0$ cm it shows an offset $y_{track} - y_{calo} = -5$ mm. It can be concluded that a relative shift of 5 mm between the tracking system and the calorimeter in the upper spectrometer half has been observed. Note that this effect is seen for both the 2000 and the 1998 data set. If the calorimeter indeed has moved physically it is displaced by -5 mm in the $y$–direction, however, a misalignment within the tracking system can as well lead to the same effect. The two possibilities cannot be distinguished at present because there are no final alignment results available yet at HERMES. Note that the observation, that the $t_{vertex}$ distribution (see figure 5.1) does not have its maximum at zero was already attributed to possible misalignment effects in the tracking system, i.e., eventually both effects may have the same origin.

Since the photons used in this analysis did convert into lepton pairs in the preshower detector, it is reasonable to assume that the shower development and thus the position reconstruction in the calorimeter behaves similarly for leptons and photons. Consequently, the reconstructed $y$–position of a photon in the top part of the calorimeter is corrected by -5 mm in this analysis. Using the same assumption, the dependence of the reconstructed position in the calorimeter on the incident angle of the photon is corrected for each event. The correction can be carried out according to the slope of the lines that fit the data in figure 5.11, which corresponds to a 1 cm correction for a particle reconstructed 80 cm away from $x$ or $y$ equal to zero. Note that the correction for the incident angle has been found to depend on the energy of the lepton as well. An additional correction has not been applied since the remaining offsets for the limiting cases of high or low energetic leptons are on the order of less than $\pm 2$ mm per 80 cm.

In summary, the corrected photon positions $x_\gamma$ and $y_\gamma$ are derived from the values $x_{calo}$ and $y_{calo}$, as given in the $\mu$DSTs, using the following equations:

$$x_\gamma = x_{calo}(1 + \frac{1}{80}), \tag{5.4}$$

$$y_\gamma^{TOP} = y_{calo}^{TOP}(1 + \frac{1}{80}) - 0.5 \text{ cm}, \tag{5.5}$$

$$y_\gamma^{BOTTOM} = y_{calo}^{BOTTOM}(1 + \frac{1}{80}). \tag{5.6}$$

A comparison between the results achieved with and without this additional corrections is shown in the right panel of figure 5.10. The important achievement is that the peak is now centered at zero. In addition, the position resolution is about 0.6 mrad now, i.e., it improves by almost 30% when applying these corrections.

# Chapter 6

# Monte Carlo Studies

In the following the **M**onte **C**arlo (MC) simulation used in this analysis will be described and the results will be compared to the data. The simulation will then be used to investigate resolution issues and to optimize signal–to–background ratios. The size of remaining background contributions is eventually extracted per bin in $x_B$, $Q^2$ and $-t$.

## 6.1 The HERMES Monte Carlo

The **H**ERMES **M**onte **C**arlo (HMC) program package is able to simulate a variety of physics processes using different programs on the event generation level. For the simulation of the semi–inclusive background contribution the MC generator LEPTO [Ing97] is used. It simulates complete events in deep–inelastic scattering of leptons off unpolarized nucleons, based on the leading order electroweak cross sections for the underlying scattering on the parton level. Partons produced in the scattering process are handed over to JETSET [Sjö94]. This program is based on the LUND string hadronization model [And83] and models the fragmentation process and the decay of unstable particles. Note that JETSET is tuned using results from high energy experiments so that for the relatively low energy at HERMES a special fragmentation tune is unavoidable [Hil03]. The BH process is taken into account via RADGEN [Aku99], a simulation of the lowest order radiative processes in QED for polarized and unpolarized DIS. Alternatively, the unpolarized case can be calculated directly using the Mo and Tsai formalism [Mo69].

After the event generation the produced particles have to be tracked through the detector. Therefore an accurate model of the detector is needed describing the location and materials of all components the particles might have to pass through.

The modeling and the actual simulation of processes which might occur during the traversal of the detector, e.g., multiple scattering or energy loss via ionization, are accomplished by the GEANT package [Cer93]. Particles crossing sensitive detector components produce a signal which is then digitized and stored in ADAMO tables, i.e., the output of the detector simulation corresponds to the output of HDC as described in section 5.1. The last two steps in the MC production chain are therefore the same as in the data processing chain, i.e., the ADAMO tables are read by HRC and $\mu$DST–files are produced in the end.

## 6.2 Monte Carlo Production and Features

Two MC productions on an unpolarized proton target are used in order to carry out the MC studies. One production, referred to as standard MC production in the following, is based on the above described simulation of the deep–inelastic process in conjunction with the RADGEN generator. The MC data sample can be subdivided in three parts. The BH events with the proton staying intact are called elastic BH events in the following, the ones where the proton undergoes a resonance excitation are referred to as associated BH events[1]. The deep–inelastic events are referred to as semi–inclusive events. The other production consists of elastic and associated BH events only, using the Mo–Tsai formalism and a certain cross–section parametrization for the resonance region [Bra76]. Note that neither the DVCS process nor other exclusive processes are taken into account in the simulation. These processes are not needed for the resolution studies but may affect the signal–to–background ratio. This is discussed in more detail in section 7.2.3.

Both productions have been normalized to their respective cross section. A comparison between them, for the variables of interest, shows only small differences for the elastic BH events. The situation is different in the resonance region where the simulation from the standard MC fails, i.e., JETSET fails below $W = 2$ GeV since there is not enough energy available in order to simulate the processes reliably. The difference on the generation level between the standard MC and the MC with the additional parametrization in the resonance region is shown in the left panel of figure 6.1. The distribution of single–photon events extracted from the standard MC production shows a decrease with increasing generated $W$ but not the expected resonance structure. The other MC shows a resonance structure, especially the $\Delta(1232)$ resonance is clearly seen. Applying the missing mass constraint in addition, the dotted distribution shows the associated BH yield in the exclusive event sample per

[1] For convenience, the DVCS process is accordingly labeled as elastic or associated DVCS process where necessary.

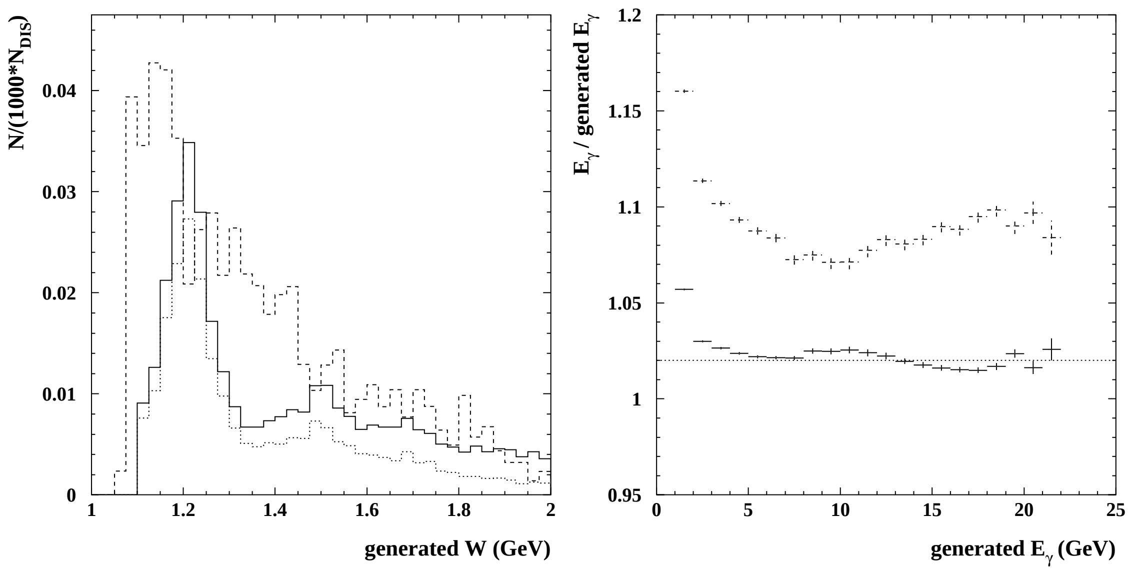


**Figure 6.1:** Left panel: Single–photon event yields from the standard MC (dashed) and from the MC with the additional parametrization [Bra76] (solid) together with the yield in the exclusive bin from the latter one (dotted) versus the generated $W$.
Right panel: Ratio between the reconstructed $E_\gamma$ and the generated $E_\gamma$ versus the generated $E_\gamma$ for photons with (solid) or without (dashed) a signal in the preshower.

---

1000 DIS events. The $\Delta(1232)$ contribution to the full resonance region, i.e., to the region with a generated $W$ between 1 and 2 GeV, is about 60% when integrating up to $W = 1.35$ GeV. For the following studies, the two MC productions are combined in that semi–inclusive processes are taken from the standard MC production and elastic and associated BH processes from the other one.

Checks on the performance of the MC itself reveal an inconsistency in the photon energy reconstruction. Over the full photon energy range used in this analysis ($E_\gamma > 3$ GeV), the energy of a reconstructed photon which did convert in the preshower exceeds the one of the generated photon by about 2%, as indicated by the dotted line in the right panel of figure 6.1. Photons which did not convert in the preshower are reconstructed with an energy overestimated by about 7 to 10%. The latter effect was already explained in section 4.3.2 and is the reason why these photons are rejected in this analysis. The 2% error in the MC for the photons which did convert is not negligible, see for example the clearly different exclusive peak positions from the 1998 and the 2000 data shown in figure 5.4, resulting from an only one percent error in the photon energy reconstruction for the 2000 data (see section 5.5.2). The energy of reconstructed photons in the MC is thus diminished

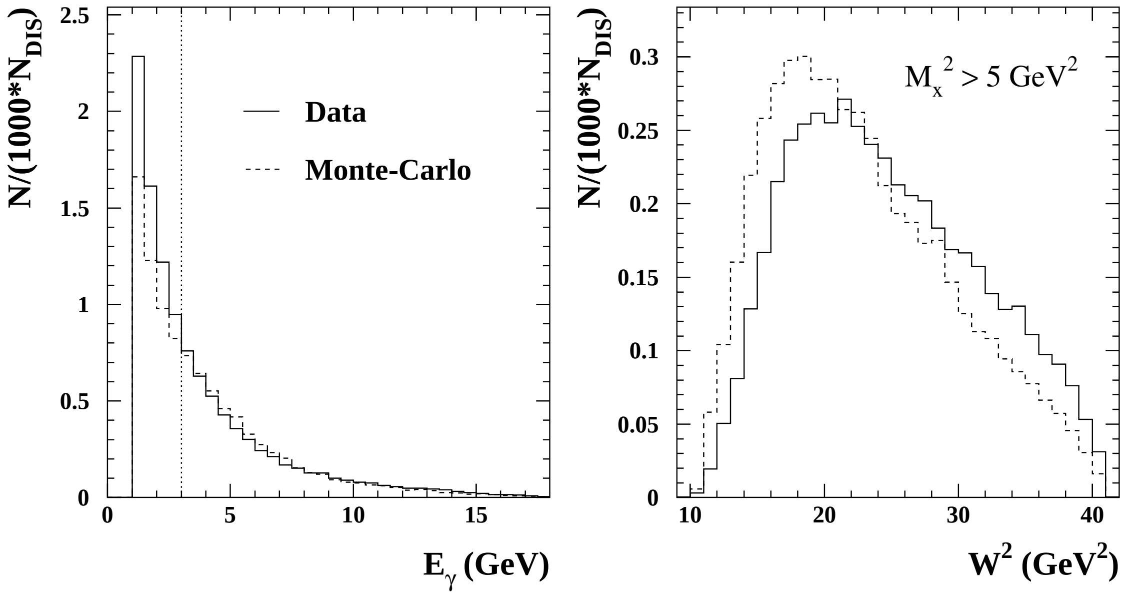


**Figure 6.2:** Single–photon event yields per 1000 DIS events from the data (solid lines) and the Monte Carlo (dashed lines) versus the photon energy $E_\gamma$ and the reconstructed $W^2$. The single–photon samples in the left panel are extracted with the constraint $E_\gamma > 1$ GeV instead of $E_\gamma > 3$ GeV, the samples in the right panel contain non–exclusive events only, ensured by the constraint $M_x^2 > 5$ GeV$^2$.

---

by 2% in the following.

## 6.3 Data to Monte Carlo Comparison

The single–photon sample has been extracted from the combined MC data and normalized to the number of DIS events. In the following all comparisons between MC and data use the data set from the year 2000 because of its higher statistics. It has been mentioned in section 5.4.2 that the constraint $E_\gamma > 3$ GeV does not reject valuable data but is imposed since the MC does not describe the data for photons with lower energies. The reason becomes obvious when comparing the single–photon yield from the data and the MC as a function of the photon energy. Below $E_\gamma =$ 3 GeV the yield in the MC is much lower than in the actual data as shown in the left panel of figure 6.2. This is due to certain processes missing on the event generation level, e.g., the generation of $\omega$ mesons, which eventually produce photons either directly in the decay or in the subsequent decay via the $\pi^0$.

Another discrepancy between data and MC is observed in the non–exclusive $W^2$ distribution, as shown in the right panel of figure 6.2. While the distributions agree with each other in the exclusive region (not shown), the shapes are quite different when using only events with $M_x^2 > 5$ GeV$^2$, i.e., a region largely dominated by semi–inclusive processes. This implies that the actual HERMES fragmentation tune (see section 6.1) used for the MC does not sufficiently well describe the production of neutral particles, especially of the $\pi^0$ which is the dominant source of photons in this region. This is due to the fact that tuning for a better description of the fragmentation processes up to now focused on the production of charged particles. In absence of a better tune the $W^2$ distribution of the MC is reweighted in order to match the data. The weighting function is calculated from the ratio of the two $W^2$ distributions shown in figure 6.2. It is then applied to all semi–inclusive events in the MC whether or not the event has a missing mass squared above 5 GeV$^2$. The resulting $W^2$ distribution of all single–photon events in the MC is compared to the data in the upper left panel of figure 6.3 and shows reasonable agreement. In order to have a valid starting point for the studies below, the consistency between the data and the reweighted MC has been checked for the other variables of interest as well. As shown in the other panels of the same figure, the agreement is quite reasonable, especially in view of the fact that data and MC are compared on the basis of an absolute normalization.

## 6.4 Resolution Studies

It has been explained in section 5.4.3 that the missing mass resolution is mainly driven by the resolution of the photon energy and that, as a consequence of the experimental resolution, events can be reconstructed with negative values of the missing mass squared. The actual photon energy resolution can be checked with the MC. It is derived through a fit to the distribution of the difference between the generated and the reconstructed photon energy. Using the exclusive sample only the resolution results to about 5%. Photons in the exclusive sample have on average an energy of 14 GeV, i.e., the average resolution corresponds to about 700 MeV. Hence, negative values of the missing mass squared do appear with photon energies in the exclusive sample of up to 22 GeV.

Since at HERMES the proton cannot be detected, $-t$ has to be calculated using the virtual and real photon kinematics and consequently is affected by the photon energy resolution as well. Hence, the $-t$ distribution of exclusive events, just like the $M_x^2$ distribution, extends to negative values as can be seen in figure 5.6. Both

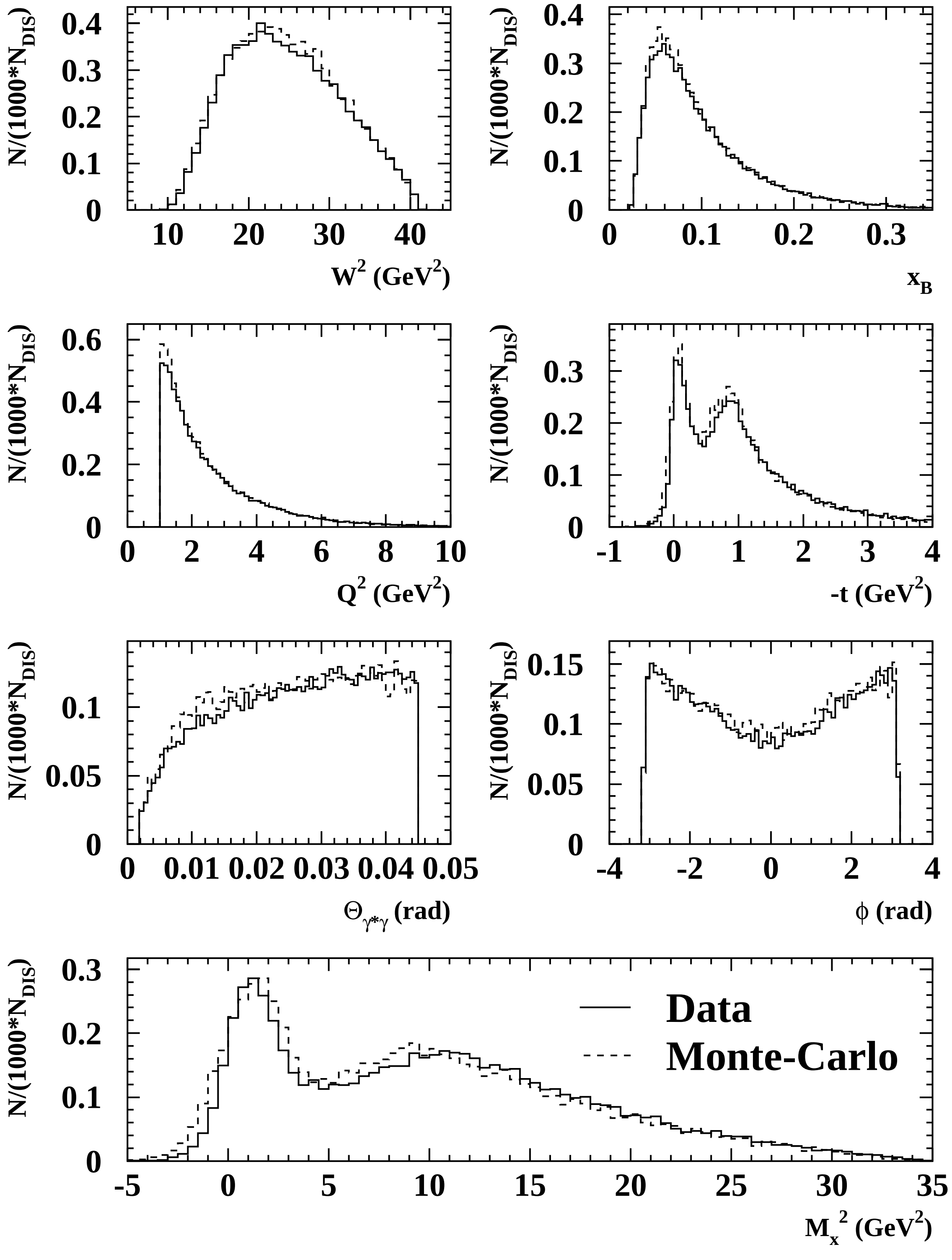


**Figure 6.3:** Comparison of the single–photon event yields per 1000 DIS events between the data from the year 2000 (solid lines) and the reweighted MC simulation (dashed lines) for different variables.

variables are related to each other via

$$M_x^2 = M_p^2 + 2\,M_p\,(\nu - E_\gamma) + t. \tag{6.1}$$

The extraction of the azimuthal asymmetries as a function of $-t$ is a main goal of this analysis. Negative values of $-t$ imply the problem that results are shown in an unphysical region where no comparison to theoretical predictions is possible. In addition, the resolution in $t$ determines the minimum bin width in $t$. The resolution is calculated comparing the generated and reconstructed variables from the MC. The upper left panel in figure 6.4 shows the $-t$ distribution for elastic BH events as calculated from the generated variables in the MC (solid line). As expected, the distribution peaks towards zero. In addition, the $-t$ distribution calculated from the reconstructed variables is shown (dotted line). A fit to the distribution of the difference between these two variables (not shown) yields a resolution in $t$ of about 0.11 GeV$^2$. Considerable improvement can be achieved as explained in the following.

For elastic events, it is possible to calculate $-t$ without the knowledge of the photon energy $E_\gamma$ by setting the missing mass squared in equation 6.1 equal to the proton mass squared. The resulting expression for the photon energy

$$E_\gamma = \frac{t}{2\,M_p} + \nu \tag{6.2}$$

can be inserted into the calculation of the four–momentum transfer squared

$$t = (q - q')^2 = -Q^2 - 2\,E_\gamma\,(\nu - \sqrt{\nu^2 + Q^2}\,\cos\theta_{\gamma^*\gamma}) \tag{6.3}$$

in order to get rid of any dependence from $E_\gamma$. The result is called the constrained momentum transfer squared

$$t_c = \frac{-Q^2 - 2\,\nu\,(\nu - \sqrt{\nu^2 + Q^2}\,\cos\theta_{\gamma^*\gamma})}{1 + \frac{1}{M_p}\,(\nu - \sqrt{\nu^2 + Q^2}\,cos\theta_{\gamma^*\gamma})}, \tag{6.4}$$

as it relies on the assumption $M_x = M_p$.

Calculating $t_c$ for the elastic BH events from the reconstructed variables in the MC results in the dashed line in the upper left panel of figure 6.4. Note that it is hardly seen because it is almost identical to the distribution of the generated $-t$ values (solid). A fit to the distribution of the difference between these two variables (not shown) yields a resolution in $t_c$ better than 0.01 GeV$^2$, i.e., the resolution is an order of magnitude better than the measured one. However, this ansatz is only correct for elastic events. In order to be able to apply this method to all data in the exclusive bin, the behavior of $t_c$ for the background reactions needs to be investigated. The

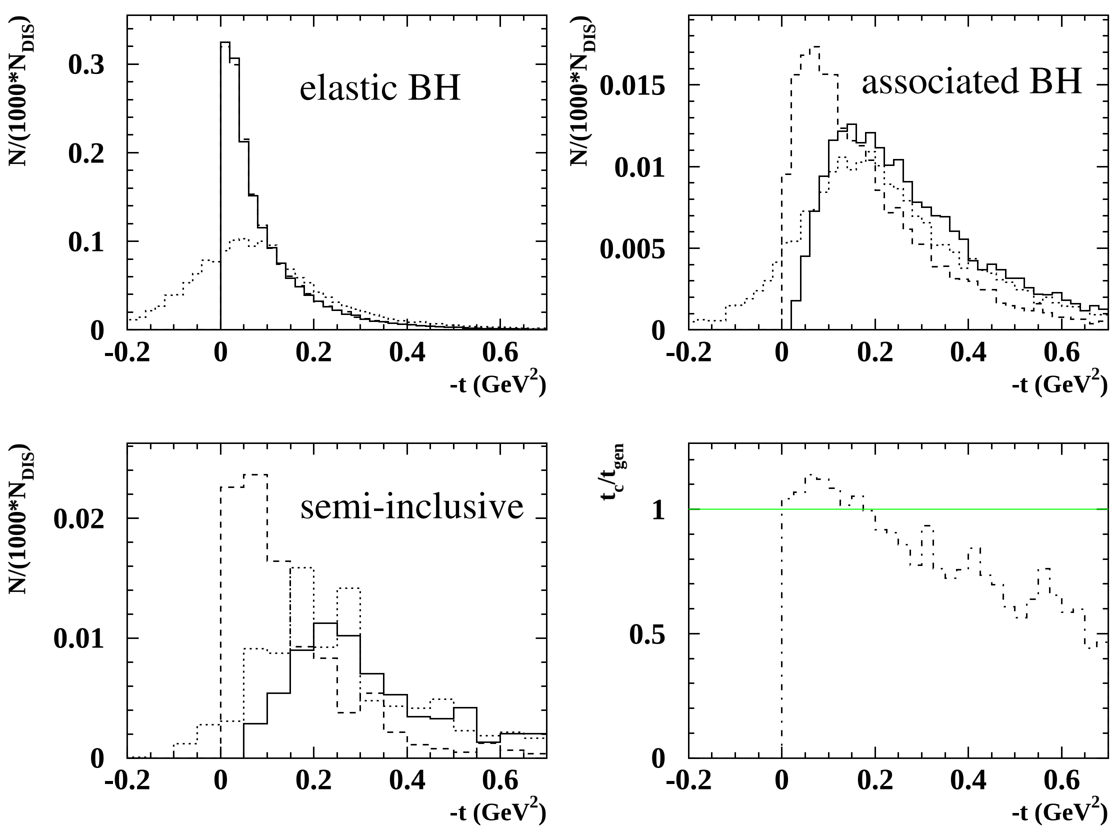


**Figure 6.4:** Different $-t$ distributions from the three processes in the exclusive MC sample as calculated from the generated variables (solid line), from the reconstructed variables (dotted line) and from the reconstructed variables in the MC when using the constraint $M_x = M_p$ (dashed lines). The lower right panel shows the ratio between constrained and generated $-t$ for the full exclusive sample.

---

upper right panel of figure 6.4 shows the generated $-t$ distribution (solid), together with the reconstructed (dotted) and the constrained one (dashed) for associated BH events in the exclusive bin. As expected, the generated $-t$ distribution does not peak at zero as in the case of elastic BH events but slightly above. Apart from the fact that the distribution of the reconstructed variable extends to negative values of $-t$ it mostly follows the generated one. This is not true for the $t_c$ distribution which is shifted towards low $-t$ values with its peak almost at zero. This is due to the fact that the assumption $M_x = M_p$ is used, i.e., these events are assumed to be elastic and therefore $-t$ is systematically calculated too small. An even stronger effect can be observed for the semi–inclusive background in the exclusive sample as shown in the lower left panel. The generated $-t$ distribution peaks at an even higher value while the constrained $-t$ has its maximum still close to zero. Note that the shape of the generated $-t$ distribution is due to the upper limit of the exclusive bin. Without an upper limit the full semi–inclusive $-t$ distribution would be similar to the $-t$ distribution shown in figure 6.3 without the exclusive peak at $t$ close to zero, i.e., it would have its peak at about $-t = 1$ GeV$^2$.

In summary, using the constrained $t$ method improves the resolution for elastic events by an order of magnitude while background events migrate towards lower $-t$ values. This can change the measured asymmetry as a function of $-t$. Assuming for instance that the background has no asymmetry and therefore acts as a dilution only, the measured asymmetry would be diminished for lower $-t$ values and enhanced for higher $-t$ values. The magnitude of this migration is shown in the lower right panel of figure 6.4. The dashed–dotted line shows the ratio $t_c/t_{gen}$ as a function of $-t$ for the full exclusive sample. For larger values of $-t$ up to 50% of the events did migrate to lower $-t$ values. Although this is a large effect, the absolute number of associated BH events and semi–inclusive events at large values of $-t$ is small as shown in the upper right and the lower left panel of the figure. Consequently, the resolution in $-t_c$ for the full exclusive sample is still about 0.01 GeV$^2$. Hence the constrained $t$ method is the preferred one to use for displaying the final result. Note that due to the migration effect the resolution in $-t_c$ is even better than 0.01 GeV$^2$ for small values of $-t_c$ and is on the same order as the measured one for large $-t_c$ values, in contrast to the resolution of the measured $-t$ value that is approximately constant in the full $-t$ range. By using the constrained method in the MC as well, the migration effect is taken into account for the calculation of the fractional contribution of background processes per kinematic bin in $-t_c$. This will be done in the next chapter.

## 6.5 Background Studies

It has been shown in section 6.3 that the combined and reweighted MC matches the data quite well. This now allows for the study of signal–to–background ratios per kinematic bin in the variables of interest and of possible optimizations when changing certain constraints on the data sample.

The contributions of the elastic BH process, the associated BH process and the semi–inclusive processes are shown separately as a function of the missing mass squared in the upper panel of figure 6.5. Note that the sum of these three contributions is the one used to compare to the actual data in the bottom panel of figure 6.3. The missing mass squared constraints are indicated by vertical lines in figure 6.5. The

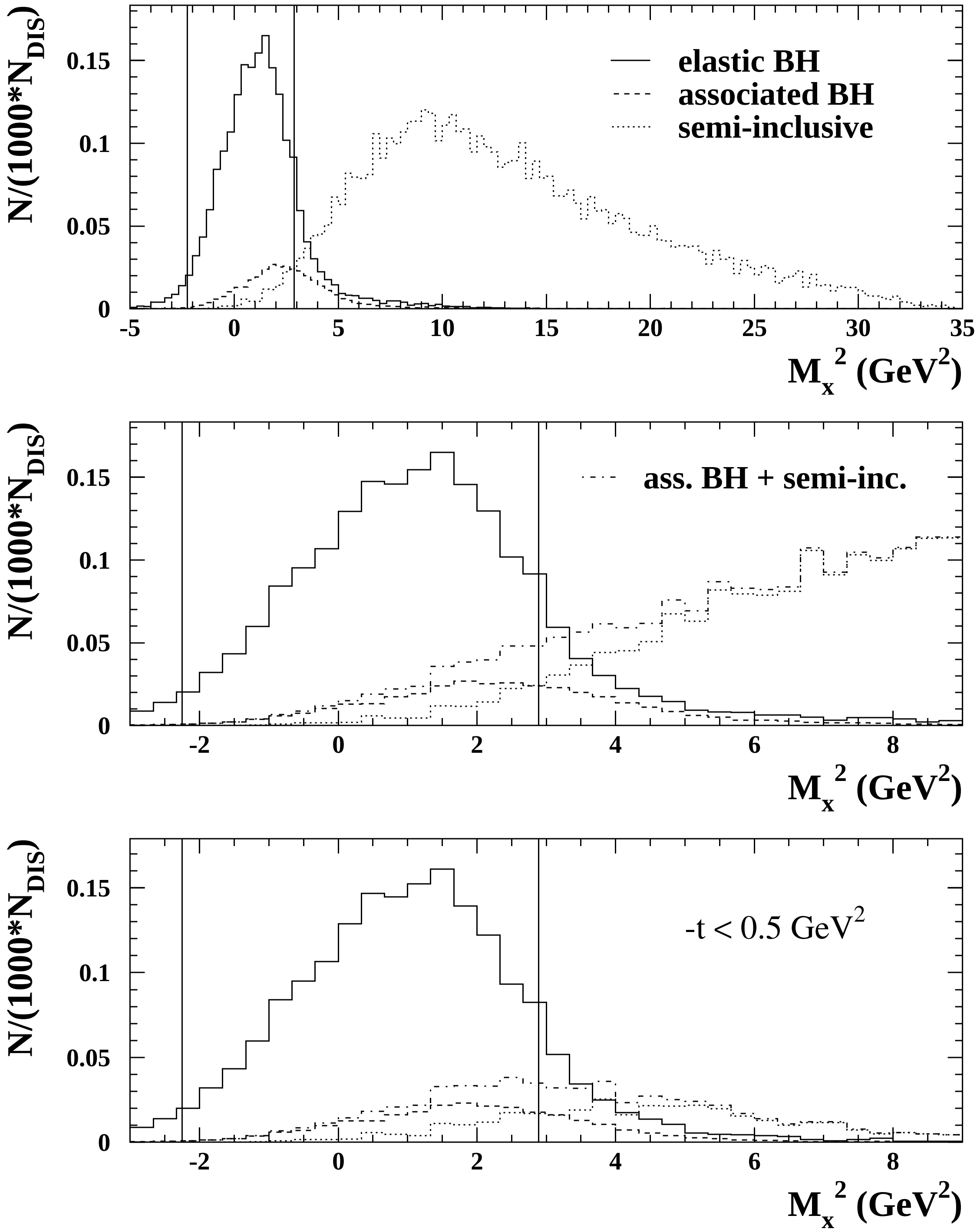


**Figure 6.5:** Contribution from the elastic BH process (solid line), the associated BH process (dashed line) and from semi–inclusive processes (dotted line) to the MC single–photon event sample as a function of the missing mass squared. The dashed–dotted line shows the sum of the background processes. The vertical lines indicate the exclusive bin. An additional $-t < 0.5$ GeV$^2$ constraint is placed on the data shown in the lower panel.

decision to use the somewhat arbitrarily chosen upper missing mass constraint from the published result (see section 3.4.2) also for this analysis can now be justified when studying the signal–to–background ratio in the region above the proton mass. In the middle panel this region is enlarged. The dashed–dotted line not present in the upper panel is the sum of the associated BH and the semi–inclusive contribution, i.e., the combined background. The used upper limit of the exclusive region appears as an adequate choice since beyond this region the elastic BH process contributes less than the background processes.

It was claimed in section 5.4.2 that although an exclusive sample can be achieved using events with small measured values of $-t$ only, the missing mass method is advantageous in terms of an optimization of the signal–to–background ratio. A maximum four–momentum transfer squared of about 0.5 GeV$^2$ would serve as a possible upper limit since most of the events in the exclusive data sample have a smaller $-t$ value (see figure 5.6). The lower panel in figure 6.5 shows again the contributions of the different processes, but this time with the additional constraint on the measured four–momentum transfer squared. The yield of the BH processes is almost unaffected while the semi–inclusive background is largely reduced above $M_x^2 = (1.7\text{ GeV})^2$. However, using only this method is disadvantageous compared to using only the missing mass method since in the region above the upper missing mass constraint the background contribution (dashed–dotted line) still dominates the signal contribution (solid line). A more strict constraint on $-t$ improves the signal–to–background ratio, but at the same time diminishes the elastic BH yield. This is not a favorable option in view of the fact that the asymmetry as a function of $t$ is a main goal of this analysis. Therefore the range in $t$ should be as large as statistics allows. Applying a restriction on the four–momentum squared which rejects only little valuable data, e.g., $-t < 0.5$ GeV$^2$, in addition to the missing mass method does not enhance the signal–to–background ratio. This can be seen when comparing the middle and the lower panel of figure 6.5 in the region below $M_x^2 = (1.7\text{ GeV})^2$. The exclusive data sample will therefore not be restricted to a certain measured $t$ range.

It has been mentioned in section 5.4.2 that the upper limit of the opening angle between the real and the virtual photon $\theta_{\gamma^*\gamma}$ is decreased to 45 mrad for this analysis. This choice is motivated by the distribution of elastic BH events (solid line), associated BH events (dashed line) and semi–inclusive events (dotted line), shown as a function of $\theta_{\gamma^*\gamma}$ in the left panel of figure 6.6. The dashed–dotted line gives the sum of the associated BH and the semi–inclusive events. The right panel shows the fraction of each process compared to the full single–photon yield in the exclusive sample as a function of $\theta_{\gamma^*\gamma}$. In the right panel it can be observed that the background

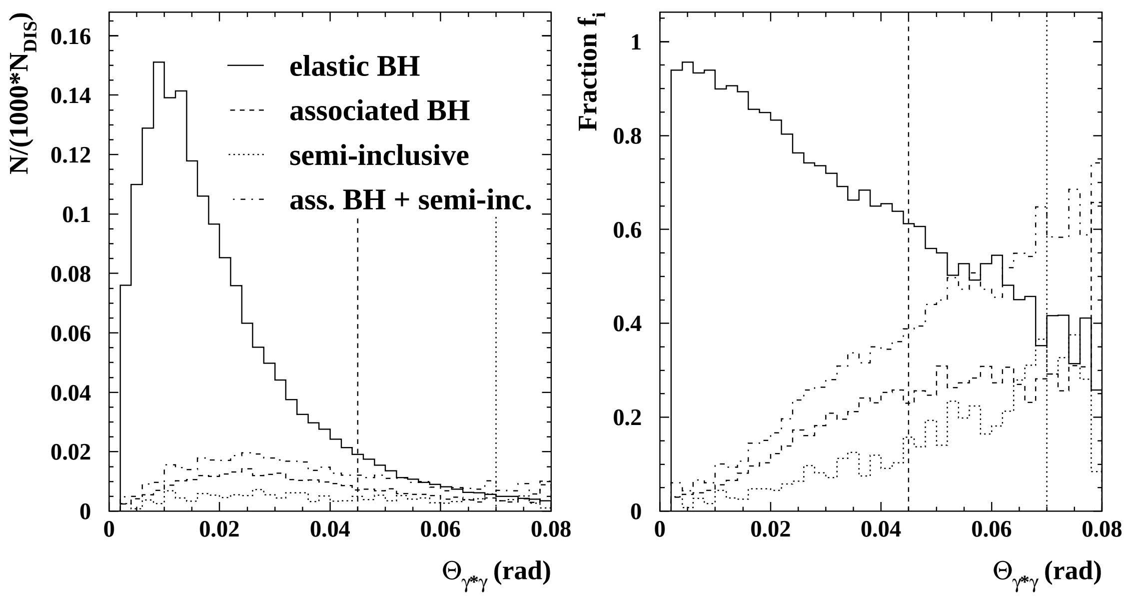


**Figure 6.6:** Single–photon yield in the exclusive sample for different processes (left panel) and the fraction of these processes with respect to the full yield (right panel) as a function of $\theta_{\gamma^*\gamma}$. The new (old) constraint on $\theta_{\gamma^*\gamma}$ of 45 mrad (70 mrad) is indicated as dashed (dotted) vertical line in both panels.

contribution exceeds the signal contribution beyond about 55 mrad, while the yield in this region is not very high as shown in the left panel. As a compromise between statistical precision and an enhanced signal–to–background ratio 45 mrad has been chosen as an upper limit. Compared to the earlier constraint of 70 mrad the total associated BH yield is decreased by about 25% and the semi–inclusive contribution is decreased by 35% while the elastic BH events in the sample are diminished by only 7%.

Ultimately the asymmetries are extracted as a function of $x_B$, $Q^2$ and $-t_c$. In order to be able to correct the measured asymmetries for the various background contributions, the contribution of each process needs to be known in each kinematic bin. The result is shown in figure 6.7 for the actual binning that is used later to display the asymmetries.

The kinematic ranges in $x_B$ and $Q^2$, as well as the bin widths, have been chosen according to the available statistics in the exclusive sample (see figure 5.6). The kinematic range in $-t_c$ is shown in the same figure. Even if statistics would allow to go up to $-t_c = 1$ GeV$^2$, the sample is already dominated by background events beyond $-t_c = 0.7$ GeV$^2$, as shown in the right panel of figure 6.7. Therefore, this

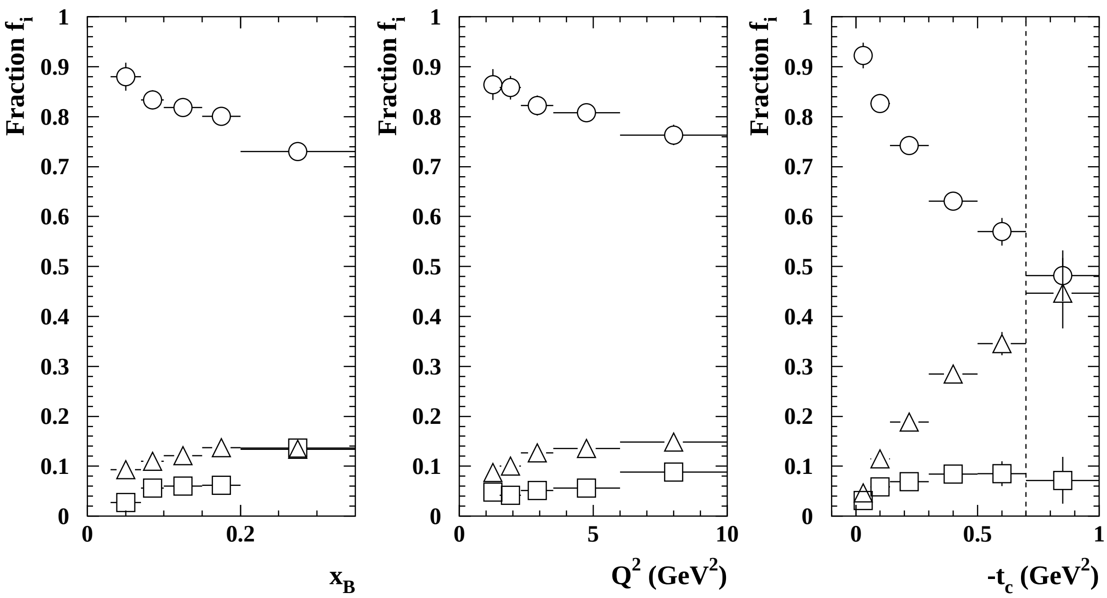


**Figure 6.7:** Fractional contribution of elastic BH events (circles), associated BH events (triangles) and semi–inclusive events (squares) with respect to their sum in the exclusive sample.

value is chosen as an upper limit and the last bin shown in the figure is discarded in the following. To summarize, in addition to the selection criteria already explained in section 5.4, the exclusive sample is constrained by the following kinematic boundaries:

$$0.03 < x_B < 0.35, \tag{6.5}$$

$$Q^2 < 10 \text{ GeV}^2, \tag{6.6}$$

$$-t_c < 0.7 \text{ GeV}^2. \tag{6.7}$$

The events in the exclusive sample originate from the elastic BH process (84.2%), from the associated BH processes (10.9%) and from semi–inclusive processes (4.9%).

# Chapter 7

# Extraction of Azimuthal Asymmetries

In the following the extraction of the beam–spin and the beam–charge asymmetries is performed. Corrections to and systematic uncertainties of the achieved results are discussed and calculated.

## 7.1 Extraction Methods

Azimuthal dependences of the beam–spin and the beam–charge asymmetries can be extracted via a fit to a cross section asymmetry as a function of the azimuthal angle $\phi$ or via a direct calculation using the so–called weighted moment method. The two methods are discussed and compared below and the latter one will be eventually chosen for the representation of the results.

### 7.1.1 Fit Method

#### Beam–Spin Asymmetry

Using a longitudinally polarized beam (L) and an unpolarized target (U), the beam–spin asymmetry $A_{LU}(\phi)$ can be calculated via a cross section ratio as

$$A_{LU}(\phi) = \frac{1}{\langle P \rangle} \frac{\frac{\overrightarrow{N}(\phi)}{\overrightarrow{NORM}} - \frac{\overleftarrow{N}(\phi)}{\overleftarrow{NORM}}}{\frac{\overrightarrow{N}(\phi)}{\overrightarrow{NORM}} + \frac{\overleftarrow{N}(\phi)}{\overleftarrow{NORM}}}, \tag{7.1}$$

where $\overrightarrow{N}$ ($\overleftarrow{N}$) represents the exclusive yield in the helicity state parallel (antiparallel) to the beam direction. The normalization (NORM) for the respective helicity state

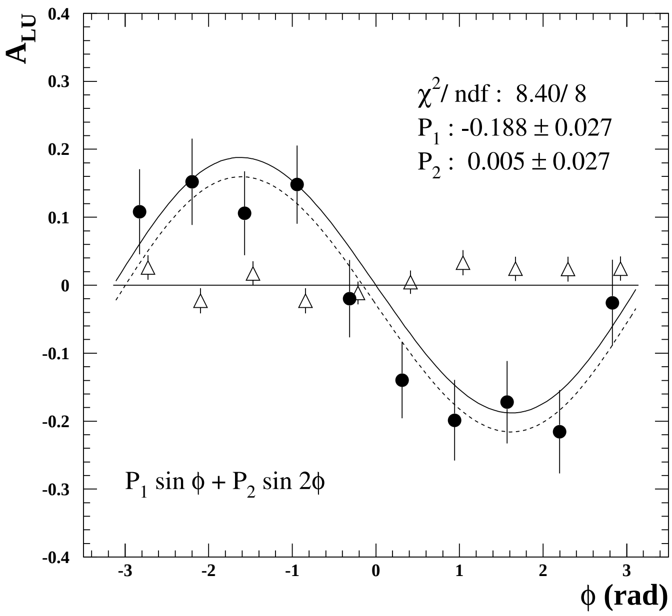


**Figure 7.1:** Beam–spin asymmetry $A_{LU}$ for the hard electroproduction of photons off the proton as a function of the azimuthal angle $\phi$ for the exclusive (filled circles) and the non–exclusive (open triangles) sample. The solid curve shows the result of the indicated two–parameter fit with the values given in the plot. The result of a fit with an additional constant term is given by the dashed curve.

---

can be done either to the number of DIS events or to the luminosity. The luminosity for a burst is calculated as the product of the rate in the luminosity monitor, the live time of trigger 21 and of the burst length. The luminosity is then given as the sum over all bursts satisfying the data quality constraints. The average value of the beam polarization $\langle P \rangle = (\langle \overrightarrow{P} \rangle + \langle |\overleftarrow{P}| \rangle)/2$ accounts for the beam not being 100% polarized. The polarization in the 2000 data sample was very similar in the positive helicity state (54%) and in the negative helicity state (-55%).

The beam–spin asymmetry as a function of $\phi$ is shown in figure 7.1, where the normalization has been done with respect to the luminosity. The amplitude of the $\sin\phi$ dependence can be obtained via a fit to the asymmetry. As has been explained in section 3.3.1, a $\sin 2\phi$ contribution may arise at higher twist and thus should be suppressed in comparison to the $\sin\phi$ contribution. A possible offset can only be due to the quality of the normalization since there is no helicity–dependent but $\phi$–independent term in the photon production cross section (see equations 3.10–3.12). A fit to the function $P_1 \sin\phi + P_2 \sin 2\phi$ has therefore been carried out. The result (solid line in figure 7.1) yields a strong $\sin\phi$ dependence of $-0.188 \pm 0.027$ while the $\sin 2\phi$ component ($0.005 \pm 0.027$) is compatible with zero. As a check, the beam–spin asymmetry has been calculated with a normalization to the number of DIS events as well (not shown). The $\sin\phi$ and $\sin 2\phi$ amplitudes yield the same values as above. In addition, including a constant term into the fit for the luminosity normalized beam–spin asymmetry, shown as a dashed line in figure 7.1, or for the DIS normalized beam–spin asymmetry (not shown), does not change the amplitudes either.

In order to demonstrate that the azimuthal asymmetries are present in the exclusive region only, $A_{LU}(\phi)$ is displayed in the same figure for the non–exclusive sample as well. Note that for the non–exclusive sample the constraint on $t_c$ is not used since already the definition of $t_c$ assumes an exclusive sample, i.e., $t_c$ has no meaning in the non–exclusive region. In order to increase statistics, the upper constraint on $\theta_{\gamma^*\gamma}$ is discarded for this sample since non–exclusive events appear on average at larger angles $\theta_{\gamma^*\gamma}$.

### Beam–Charge Asymmetry

The extraction of azimuthal dependences of the beam–charge asymmetry via the fit method follows in the same way. The beam–charge asymmetry as a function of $\phi$ is calculated as

$$A_C(\phi) = \frac{\frac{N^+(\phi)}{DIS^+} - \frac{N^-(\phi)}{DIS^-}}{\frac{N^+(\phi)}{DIS^+} + \frac{N^-(\phi)}{DIS^-}}, \tag{7.2}$$

with the yield $N^+$ ($N^-$) and the number of DIS events $DIS^+$ ($DIS^-$) using the positron (electron) beam. A normalization to the luminosity is disfavored for the calculation of the beam–charge asymmetry due to the large systematic uncertainty for the electron data (see section 4.3.4). When both beam and target are unpolarized, the leading twist contribution should be dominated by a $\cos\phi$ behavior, possibly accompanied by a kinematically suppressed offset as discussed in section 3.3.2. However, in the analyzed data the beam is not unpolarized, i.e., $\lambda$ is not zero in equation 3.12, and thus an additional $\sin\phi$ dependence is expected. The beam–charge asymmetry as a function of $\phi$ is shown in figure 7.2. Using the exclusive sample, a fit to the function $P_1 + P_2\sin\phi + P_3\cos\phi$ (dashed curve) yields a $\cos\phi$ dependence with an amplitude of $0.045 \pm 0.027$. The constant term is compatible with zero. The $\sin\phi$ dependence is indeed sizeable but smaller than the one extracted in the last section from the positron sample and, moreover, has a different sign. This is explained in the following. In the numerator of the beam–charge asymmetry, the difference is calculated between a positron sample $N^+$ containing both helicities with an average polarization of -7.5% and an electron sample $N^-$ containing one

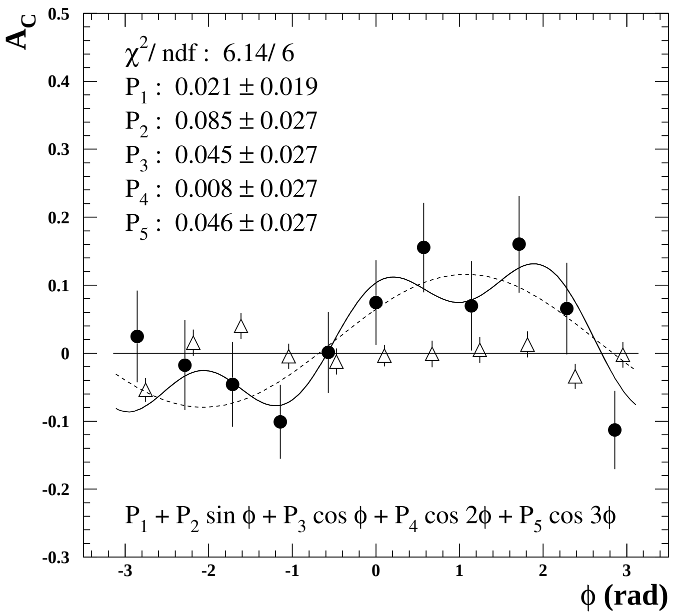


**Figure 7.2:** Beam–charge asymmetry $A_C$ for the hard electroproduction of photons off the proton as a function of the azimuthal angle $\phi$ for the exclusive (filled circles) and the non–exclusive (open triangles) sample. The solid curve shows the result of the indicated five–parameter fit with the values given in the plot. The result of the fit with $P_4$ and $P_5$ set equal to zero is given by the dashed curve.

---

helicity state only with an average polarization of about -30.5%. The difference in the numerator of the beam–spin asymmetry (see equation 7.1) is defined between a positive helicity sample $\overrightarrow{N}$ and a negative helicity sample $\overleftarrow{N}$, both derived using the same beam charge. Since the sign of the $\sin\phi$ amplitude in the interference term (see equation 3.12) depends on the charge and the helicity of the beam, the $\sin\phi$ behavior in the numerator of the beam–charge asymmetry is the same whether the sample $N^+$ is a positron sample with a negative helicity or an electron sample with a positive helicity. Assuming the latter case together with the negative helicity electron sample $N^-$, the numerator yields the same $\sin\phi$ dependence as the one of the beam–spin asymmetry when using an electron beam. Since the sign of the beam–spin asymmetry depends on the charge of the beam (see equation 3.14), the $\sin\phi$ asymmetry of -0.188, as extracted from the positron sample in the last section, translates in a positive one for the electron sample. The main reason for the about two times smaller $\sin\phi$ contribution derived here is due to the fact that equation 7.2 is not weighted by the inverse average beam polarization. Note that even with the additional weight applied, the $\sin\phi$ values are not necessarily consistent due to different contributions in the denominator.

It was mentioned in section 3.3.2 that possible higher twist contributions should exhibit a $\cos 2\phi$ and $\cos 3\phi$ behavior. A second fit including these two functions has been carried out for the beam–charge asymmetry as well. The result is shown in the same figure and yields the same results as the three–parameter fit for the values of $P_1$, $P_2$ and $P_3$. Similar to the case of the beam–spin asymmetry, the $\cos 2\phi$ value is compatible with zero. In contrast to the expectation the $\cos 3\phi$ contribution has the same size as the leading twist contribution. This will be discussed in section 9.2.

The size of remaining azimuthal asymmetries in the non–exclusive sample is small as shown in the same figure (open triangles). As above, no constraint on $t_c$ and on the upper limit of $\theta_{\gamma^*\gamma}$ is applied.

### 7.1.2 Weighted Moment Method

#### Beam–Spin Asymmetry

The $\sin\phi$ ($\sin 2\phi$) dependence of the beam–spin asymmetry for a longitudinally polarized beam (L) and an unpolarized target (U) can be directly calculated via the weighted moment method as

$$A_{LU}^{w(\phi)} = \frac{2}{\langle P \rangle} \frac{\frac{1}{\overrightarrow{NORM}} \sum_{i=1}^{\overrightarrow{N}} w(\phi_i) - \frac{1}{\overleftarrow{NORM}} \sum_{i=1}^{\overleftarrow{N}} w(\phi_i)}{\frac{\overrightarrow{N}}{\overrightarrow{NORM}} + \frac{\overleftarrow{N}}{\overleftarrow{NORM}}} \tag{7.3}$$

with $w(\phi) = \sin\phi$ ($\sin 2\phi$). The weighting method projects out the $\sin\phi$ ($\sin 2\phi$) moment which has half the size of the respective amplitude. The additional factor of two was introduced to account for this. Asymmetries of the form $A^{w(\phi)}$ are referred to as $w(\phi)$ moment of the asymmetry $A$ in the following. The variables are the same as used in section 7.1.1. In the case of the beam–spin asymmetry the ratio $\overrightarrow{N}/\overrightarrow{NORM}$ has to be equal to $\overleftarrow{N}/\overleftarrow{NORM}$, because the cross section has to be the same for both helicities after integrating over $\phi$. Equation 7.3 then simplifies to

$$A_{LU}^{w(\phi)} = \frac{1}{\langle P \rangle} \left( \frac{1}{\overrightarrow{N}} \sum_{i=1}^{\overrightarrow{N}} w(\phi_i) - \frac{1}{\overleftarrow{N}} \sum_{i=1}^{\overleftarrow{N}} w(\phi_i) \right) . \tag{7.4}$$

This is a very convenient simplification since no normalization to the number of DIS events or to the luminosity is needed anymore. In the special case that no helicity–independent $\sin\phi$ ($\sin 2\phi$) contributions need to be canceled in the asymmetry, i.e.,

$s_1^{BH}$ in equation 3.10 is zero as well as possible $\sin\phi$ ($\sin 2\phi$) contributions arising from acceptance effects, the equation can be simplified further. Taking the sign of the helicity into account via a polarization weighting of every single event, the $w(\phi)$ moment of the beam–spin asymmetry can be calculated as

$$A_{LU}^{w(\phi)} = \frac{2}{N}\sum_{i=1}^{N}\frac{w(\phi_i)}{P_i} \tag{7.5}$$

with $N = \overrightarrow{N} + \overleftarrow{N}$. Note that even if the assumptions made above are correct, the last two equations are only exactly equivalent if the polarization is constant and the yield is the same in both helicity states. Although this never is the case, it is approximately true for the data used in this analysis. The difference in the results derived from the two equations has been checked and found to be negligible. The advantage of equation 7.5 is that the asymmetry can be calculated from any given yield N, whether or not both helicity states contribute. In addition, in a case where the yield in one helicity state is higher than in the other, the statistical error obtained through the latter equation with the combined event sample is smaller than that from the former equation, where the errors from the two helicity samples are calculated separately and added in quadrature. The data from the two helicities can be combined since the physics information is the same in both states, as shown in the left panel of figure 7.3 for the case of the $\sin\phi$ asymmetry. It is displayed as a function of the missing mass for both helicity states separately. They are consistent in the exclusive region within errors. The asymmetry for the exclusive sample can be calculated via an integration between -1.5 and 1.7 GeV. The result in the positive (negative) helicity state is $-0.174\pm0.041$ ($-0.205\pm0.035$). The result from equation 7.5 for the full data sample is displayed by the full circles in the right panel of the same figure. The integration yields an asymmetry of $-0.192\pm0.027$. Since this is the result from the combined statistics, the value is not exactly the average of the two separate results (-0.190), but is slightly shifted towards the value from the helicity state with the bigger statistics, i.e., the negative one. The same calculation has been carried out for the $\sin 2\phi$ asymmetry. The weighted method yields $-0.006 \pm 0.027$.

Taking into account the contribution of the different processes per bin in $M_x$ as shown in figure 6.5, the asymmetry in the right panel of figure 7.3 shows the expected behavior. Note that figure 6.5 actually shows $M_x^2$, with $M_x = -\sqrt{-M_x^2}$ if the missing mass squared is negative. The asymmetry is the largest for the first two bins in $M_x$ where the contribution of the background processes is the smallest. The third bin that includes the proton mass ($0.4 < M_x < 1.4$ GeV) shows a slightly smaller asymmetry since background contributions start to dilute the asymmetry. The fourth bin yields a mixture of the exclusive and the non–exclusive sample and

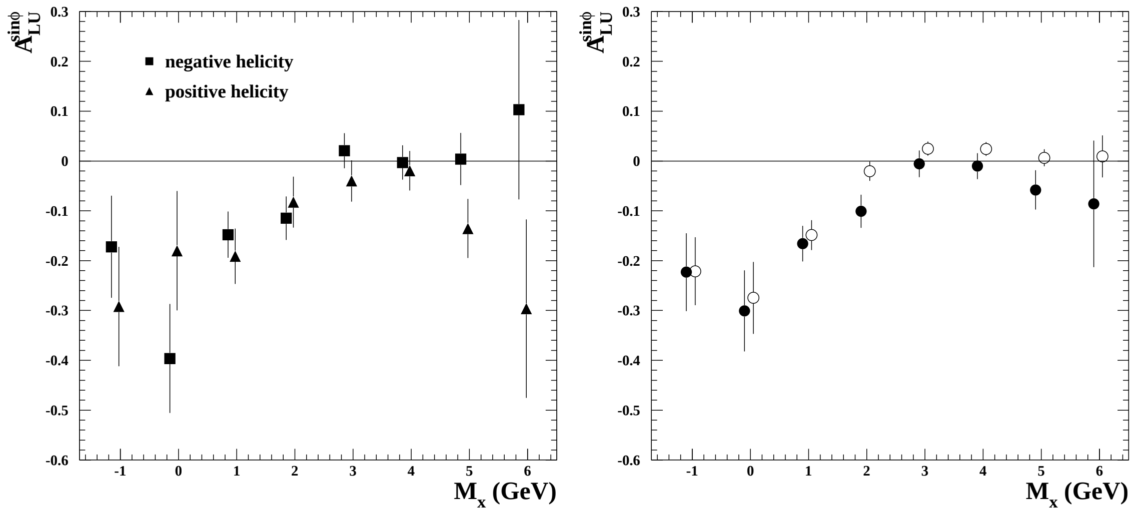


**Figure 7.3:** The $\sin\phi$ moment of the beam–spin asymmetry $A_{LU}^{\sin\phi}$ as a function of the missing mass for the positive and negative helicity sample (left panel) and for the combined sample (right panel). The filled and open circles in the right panel show the results for the single–photon sample with and without the constraints on $t_c$ and on the upper limit of $\theta_{\gamma^*\gamma}$, respectively.

---

consequently shows a decreased asymmetry value. In addition, in this bin the filled and the open circles clearly deviate. The open circles show the asymmetry without the constraints on $t_c$ and on the upper limit on $\theta_{\gamma^*\gamma}$, i.e., the data sample contains more semi–inclusive events, and thus the asymmetry is reduced for this sample. The last four bins should not yield any contributions from the BH–DVCS interference anymore. There indeed is no sign for a negative asymmetry, especially when looking at the open circles with the increased statistics. The latter sample even shows a small positive asymmetry in the two bins around 2.9 and 3.9 GeV. This is due to a beam–spin asymmetry in $\pi^0$ production which is carried by the one detected photon from the $\pi^0$ decay. The calculation of the latter in the exclusive bin is described in detail in section 7.2.3. The same calculation in the two bins around 2.9 and 3.9 GeV, i.e., from 2.4 to 4.4 GeV, indeed results in a slightly positive asymmetry of $0.036 \pm 0.015$.

### Beam–Charge Asymmetry

The moments of the weighted beam–charge asymmetry are defined as

$$A_C^{w(\phi)} = 2\frac{\frac{1}{DIS^+}\sum_{i=1}^{N^+} w(\phi_i) - \frac{1}{DIS^-}\sum_{i=1}^{N^-} w(\phi_i)}{\frac{N^+}{DIS^+} + \frac{N^-}{DIS^-}}, \tag{7.6}$$

with $w(\phi) = \cos\phi$, $\cos 2\phi$, $\cos 3\phi$ and the other variables defined as above. The constant part of the beam–charge asymmetry can be calculated setting $w(\phi)$ equal to 1/2 in order to cancel the additional factor of two in the equation. This equation cannot be simplified as in the case of the beam–spin asymmetry since the cross section integrated over the azimuthal angle $\phi$ is not the same for the two beam charges, i.e., $N^+/DIS^+$ is not equal to $N^-/DIS^-$. This is due to the $\phi$–independent but charge–dependent term $c_0^I$ in the interference term (see equation 3.12). In addition, the physics information is not the same in both charge states, i.e., they are both needed to cancel out charge–independent contributions which can actually be large. As an example, $A_C^{\cos\phi}$ has been calculated separately for the two beam–charges according to equation 7.6. The result is shown in the left panel of figure 7.4. Note that the result from the electron data has been multiplied by $-1$ for an easier comparison in the figure. The huge $\cos\phi$ moment in the high missing mass region is due to acceptance effects and will be discussed in the next section in more detail. In the lower missing mass region the $\cos\phi$ dependence of the BH process ($c_1^{BH}$ in equation 3.10) should constitute the charge–independent contributions in addition to acceptance effects. Since these contributions should be the same for both charges, differences between the two results should therefore point to a non–zero beam–charge asymmetry. This can be observed in the two bins at 0.9 GeV and 1.9 GeV only. The size of the asymmetry is then approximately half of the seen difference. The $\cos\phi$ asymmetry from the combined sample is shown in the right panel of the same figure. Only the two above mentioned bins show a clear signal. The integration in the exclusive missing mass region yields an asymmetry of $0.051 \pm 0.027$. Calculating the $\cos 2\phi$ ($\cos 3\phi$) asymmetry using the weighted moment method gives a value of $0.007 \pm 0.027$ ($0.060 \pm 0.027$).

The behavior of the $\sin\phi$ moment of the beam–spin asymmetry as a function of the missing mass (see right panel of figure 7.3) was discussed above and found to be understandable taking into account the signal–to–background ratios per missing mass bin. The high missing mass region of the $\cos\phi$ moment of the beam–charge asymmetry in the right panel of figure 7.4 looks quite similar. The large contributions from the single charges at high missing masses (left panel) cancel in the combined sample (right panel). Especially when looking at the open circles with the increased

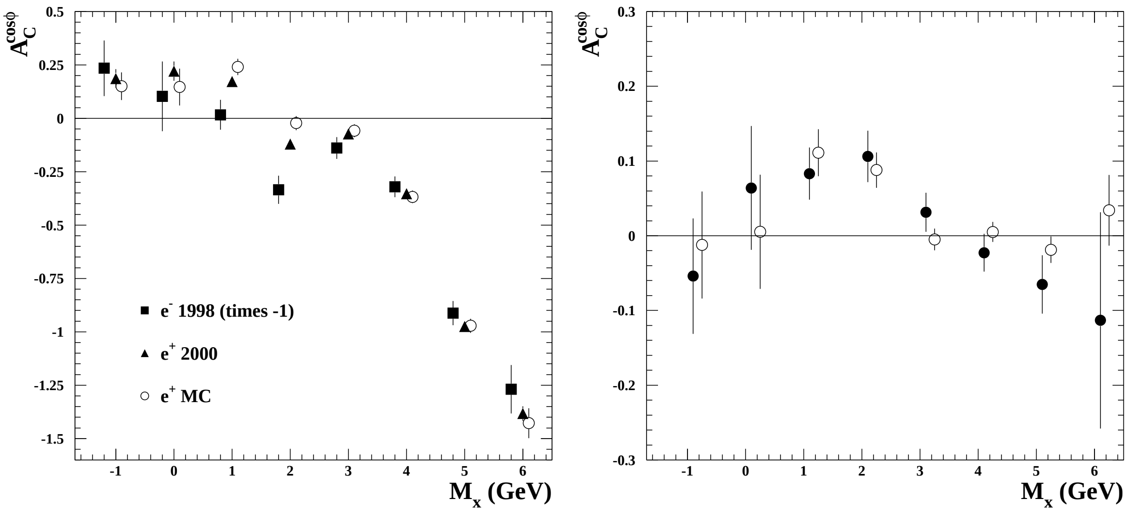


**Figure 7.4:** The $\cos\phi$ moment of the beam–charge asymmetry $A_C^{\cos\phi}$ as a function of the missing mass for the data from 1998 and 2000 and from the MC data (left panel). The result for the electron sample is multiplied by $-1$ for easier comparison. In the right panel, the result is given for the combined single–photon data sample with (filled circles) and without (open circles) the constraints on $t_c$ and on the upper limit of $\theta_{\gamma^*\gamma}$.

---

statistics due to releasing the $t_c$ and $\theta_{\gamma^*\gamma}$ constraints, the asymmetry is compatible with zero for the last four missing mass bins. The behavior in the first four bins, on the other hand, is completely different when compared to the beam–spin asymmetry. While the signal in the first two $M_x$ bins is statistically inconclusive, the fact that the asymmetry in the fourth bin is even slightly higher than the one in the third bin cannot be understood from simple signal–to–background ratio arguments anymore. The fourth bin should already be largely diluted from charge symmetric semi–inclusive processes. Moreover, the asymmetry in this particular bin is only slightly diminished when going from the usual single–photon sample (filled circles) to the one with the enhanced background contributions (open circles). This implies a possible explanation, namely, that the $\cos\phi$ moment from the signal (BH, DVCS) events gained via opening the constraints seems to be so large that it keeps the asymmetry almost constant, even though the dilution due to the additional background (semi–inclusive) events became bigger. A common feature of the additional signal and background events is their large value of $-t$. Note that the measured $t$ is the only valid one in this discussion since the use of $t_c$ automatically fixes the missing mass to be equal to the proton mass, i.e., there are no different bins to compare to each other anymore. The average $-t$ value in the third and fourth bin of the usual single–photon sample amounts to 0.13 GeV$^2$ and 0.44 GeV$^2$, respectively. At the same time the average values of $x_B$ and $Q^2$ show only small variations. This confirms the conjecture that the asymmetry is large only for large values of $-t$. It gives a possible explanation for the seemingly strange behavior versus $M_x$ and calls for an extraction of the asymmetry as a function of the kinematic variables, in particular of $-t$.

### Acceptance Corrections

In general, the HERMES spectrometer acceptance is not uniform and, in particular, may affect the measured $\phi$ distributions of the single-photon events. This might bias the extracted moments of the asymmetries while $\phi$–dependent acceptance effects cancel out in the fit method that uses a ratio of cross sections. Acceptance corrections will therefore only be discussed for the weighted moment method.

The HERMES acceptance has a large $\cos\phi$ moment as can be seen in the left panel of figure 7.4 at high missing masses. While the $\cos\phi$ moment at small missing masses has contributions from the BH process, the BH-DVCS interference and from the acceptance, the $\cos\phi$ moment at high missing masses should arise from acceptance effects alone. This can be checked using the MC described in chapter 6. The $\cos\phi$ moment extracted from the MC sample is shown in the left panel of figure 7.4 together with the $\cos\phi$ moments from the data. The agreement between the data and the MC is very good in the high-missing mass region. Since associated and elastic BH contributions are essentially zero in this region (see figure 6.5) and the DVCS process is not even included in the MC simulation, it confirms that the large values in the $\cos\phi$ moment are due to acceptance effects. Note that the disagreement between MC and data observed in the low missing mass region is expected since in this region the asymmetry is observed.

Despite the fact that the individual $\cos\phi$ moments can be large, the $\cos\phi$ moment of the combined sample seems to be largely insensitive to the acceptance as shown in figure 7.4, where the acceptance effects of the individual moments in the high missing mass region (left panel) cancel entirely in the high missing mass region of the moment from the combined sample (right panel). Nevertheless, for an extraction of asymmetries per kinematic bin and for the extraction of higher $\sin\phi$ and $\cos\phi$ moments an acceptance correction in every kinematic bin is needed. It is described in the following.

The normalized experimental yield can be expanded in a Fourier series in $\phi$ [Car99],

$$\frac{2\pi}{N}\frac{dN}{d\phi} = 1 + \sum_m \left[\alpha_m \cos(m\phi) + \beta_m \sin(m\phi)\right], \tag{7.7}$$

as can the "true" cross section of the observed process times the luminosity ($\sigma L$) as well as the spectrometer acceptance ($\epsilon$):

$$\frac{2\pi}{\sigma L}\frac{d(\sigma L)}{d\phi} = 1 + \sum_m \left[a_m \cos(m\phi) + b_m \sin(m\phi)\right], \tag{7.8}$$

$$\frac{2\pi}{\int \epsilon(\phi) d\phi}\epsilon(\phi) = 1 + \sum_m \left[A_m \cos(m\phi) + B_m \sin(m\phi)\right]. \tag{7.9}$$

Using the fact that $\frac{dN}{d\phi} = \frac{d(\sigma L)}{d\phi}\epsilon(\phi)$ and restricting the Fourier series to $m \leq 3$, the result can be rewritten using a matrix representation

$$\begin{pmatrix} \alpha_1 \\ \alpha_2 \\ \alpha_3 \\ \beta_1 \\ \beta_2 \\ \beta_3 \end{pmatrix} = N_f \times \begin{pmatrix} A_1 \\ A_2 \\ A_3 \\ B_1 \\ B_2 \\ B_3 \end{pmatrix} + \frac{1}{2} N_f \times \tag{7.10}$$

$$\begin{pmatrix} 2+A_2 & A_1+A_3 & A_2+A_4 & B_2 & B_1+B_3 & B_2+B_4 \\ A_1+A_3 & 2+A_4 & A_1+A_5 & B_3-B_1 & B_4 & B_1+B_5 \\ A_2+A_4 & A_1+A_5 & 2+A_6 & B_4-B_2 & B_5-B_1 & B_6 \\ B_2 & B_3-B_1 & B_4-B_2 & 2-A_2 & A_1-A_3 & A_2-A_4 \\ B_1+B_3 & B_4 & B_5-B_1 & A_1-A_3 & 2-A_4 & A_1-A_5 \\ B_2+B_4 & B_1+B_5 & B_6 & A_2-A_4 & A_1-A_5 & 2-A_6 \end{pmatrix} \times \begin{pmatrix} a_1 \\ a_2 \\ a_3 \\ b_1 \\ b_2 \\ b_3 \end{pmatrix}.$$

The normalization factor $N_f$ arises from the multiplication of the two Fourier series and is given by

$$N_f = \frac{1}{1 + \frac{1}{2}\sum\limits_{m=1}^{3}(A_m a_m + B_m b_m)}. \tag{7.11}$$

The matrix representation visualizes the convolutions of acceptance and cross section moments for any measured moment. Assuming for instance that only the $\cos\phi$ moment of the HERMES detector acceptance $A_1$ has a non–zero value, the measured $\cos\phi$ moment $\alpha_1 = N_f\,(a_1 + A_1 + A_1\,a_2/2)$ gets contributions not only from this first acceptance moment $A_1$ as discussed above, but in addition from the convolution of this moment with the true $\cos 2\phi$ moment $a_2$, if there is one. If, on the other hand, all true moments but the $\cos\phi$ moment $a_1$ are zero, the measured $\cos\phi$ moment $\alpha_1 = N_f\,(a_1 + A_1 + a_1\,A_2/2)$ is still made up by the first moment of the acceptance $A_1$ and by the convolution of the true moment with the $\cos 2\phi$ moment of the acceptance $A_2$, if it is sizeable.

The acceptance moments have been calculated using BH events from the MC. In order to get rid of the $\cos\phi$ dependence of the BH cross section (see equation 3.10),

| $A_1$ | $A_2$ | $A_3$ | $A_4$ | $A_5$ | $A_6$ |
|---|---|---|---|---|---|
| -0.238 | 0.003 | 0.001 | 0.000 | 0.000 | 0.002 |
| $B_1$ | $B_2$ | $B_3$ | $B_4$ | $B_5$ | $B_6$ |
| 0.004 | -0.001 | 0.004 | -0.012 | -0.001 | -0.007 |

**Table 7.1:** The first six cosine ($A_1$–$A_6$) and sine ($B_1$–$B_6$) moments of the HERMES detector acceptance for the integrated kinematics of the given data sample. The statistical error per acceptance moment is 0.001.

---

every reconstructed event was reweighted by the ratio of the BH cross section at a fixed angle $\phi = c$ divided by the BH cross section at the angle of the actual event. The BH cross section was calculated using a computer code by Vanderhaeghen, Guichon and Guidal [Van01] which was used on the generator level as well for consistency. The first six sine and cosine moments of the acceptance have been extracted from the reconstructed and reweighted events. This was done for every kinematic bin in $x_B$, $Q^2$ and $t_c$ used later on to display the results. These moments are shown in table B.1 for the cosine and in table B.2 for the sine acceptance moments per kinematic bin. The acceptance moments for the integrated kinematics are shown in table 7.1. The $\cos\phi$ moment of the acceptance is indeed the dominant one. The resulting effect for the measured $\cos\phi$ moment was already shown and discussed above. Concerning the measured $\sin\phi$ moment $\beta_1$, the biggest acceptance effect might thus arise from the coupling of the $\cos\phi$ moment of the acceptance with the $\sin 2\phi$ moment of the true cross section $b_2$ (see Equation 7.10), if the latter one is non–zero.

The acceptance correction has been carried out for every individual beam-spin and beam-charge moment in every bin. The acceptance corrected individual moments are derived by inverting the matrix equation 7.10. The results are shown in the next section. Note that the acceptance moments are derived using the reconstructed variables, thus they include possible effects arising from detector smearing and external bremsstrahlung. This will be discussed in more detail in section 7.2.1.

### 7.1.3 Comparison of Methods

Two different methods to extract the azimuthal dependences of the beam–spin and the beam–charge asymmetries have been discussed above and used to extract values for the integrated asymmetries. Even without any acceptance corrections applied, the results turn out to be quite similar for both methods, e.g., the size of the $\sin\phi$ ($\cos\phi$) dependence of the beam–spin (beam–charge) asymmetry was found to be

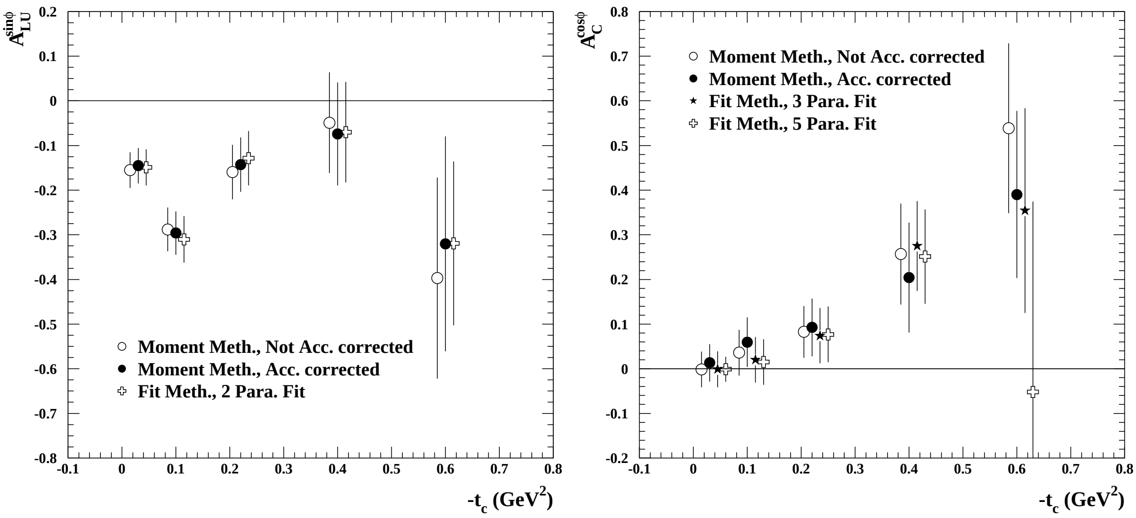


**Figure 7.5:** The $\sin\phi$ moment $A_{LU}^{\sin\phi}$ (left panel) and the $\cos\phi$ moment $A_C^{\cos\phi}$ (right panel) as a function of $-t_c$. The results are derived using the moment method before and after the acceptance correction and the fit method. The fit functions are the two–parameter fit (left panel) already used in figure 7.1 and the three– and the five–parameter fit (right panel) employed in figure 7.2.

---

$-0.188 \pm 0.027$ ($0.045 \pm 0.027$) and $-0.192 \pm 0.027$ ($0.051 \pm 0.027$) when using the fit and the moment method, respectively. In addition, the fit method was found to be essentially insensitive to the number of fit parameters. However, since the goal of this analysis is the extraction of the asymmetries per kinematic bin, the comparison between the two methods should be based on these results. As an example, the first moments of the asymmetries are shown as a function of $-t_c$ in figure 7.5. In the left panel the $\sin\phi$ moment of the beam-spin asymmetry is shown before and after acceptance corrections together with the result obtained from the fit method when applying it to every bin in $-t_c$. The results are quite close to each other except in the last bin where the acceptance correction gives a visible effect. The corrected value is in excellent agreement with the result from the fit and thus gives confidence in the acceptance correction procedure, although the statistics in this particular bin may be too small to be conclusive. In the right panel of figure 7.5 the fit results from the three– and from the five–parameter fit to the beam–charge asymmetry are shown in addition to the values obtained from the moment method before and after the acceptance correction. In the first four bins the values from the two fits agree quite well with each other and with the values from the moment method before applying the acceptance corrections. This indicates that $\phi$–dependent acceptance effects are small, since the fit method is independent of them but the moment method is not. The difference between the moments before and after the acceptance correction should then be due to external bremsstrahlung and detector smearing, which are not taken into consideration in the fit method but accounted for by the acceptance correction. This will be investigated further in section 7.2.1.

Concerning the stability of the fit method the number of parameters and bins used for the fit has been varied. If the statistics are large enough, as it is the case in the first three bins in the right panel of figure 7.5, the differences between the results of the three– and the five–parameter fits are negligible. The difference becomes visible in the forth bin and is quite sizeable in the last one. The result of the five–parameter fit is not reliable anymore and consequently also the extraction of higher moments turns out to be not reliable in the last bin. The number of bins used for the three–parameter fit has been varied by up to $\pm 3$ bins with respect to the 11 bins used up to now (see e.g. figure 7.2). The difference in the extracted results (not shown) is even larger than the one between the three– and the five parameter fit shown in the right panel of figure 7.5, since it is already visible in the third bin.

The decision about which method to use in the following is taken considering the advantages and drawbacks of both methods. In summary, the fit method is independent of $\phi$–dependent acceptance effects, but it still suffers from bremsstrahlung and detector smearing. For the moment method, the acceptance correction accounts for the latter two effects as well. In addition, the fit method yields extra systematic uncertainties due to fluctuations in the extracted value depending on the number of bins and parameters used for the fit. Therefore the moment method will be used to extract the final results for the azimuthal asymmetries.

## 7.2 Corrections and Uncertainties

### 7.2.1 Acceptance, External Bremsstrahlung and Smearing

While small variations in the initial beam energy (up to 30 MeV in 1998) are recorded for every burst and thus can be taken into account easily, the incoming lepton may loose energy by radiating a photon before the interaction takes place. This usually cannot be taken into account since the photon propagates undetected down the beam pipe. Consequently, the incoming lepton has a lower energy than the nominal beam energy and the event kinematics get wrongly reconstructed. The same can happen after the interaction, i.e., if the scattered lepton radiates a photon before traversing the magnet, it already lost some energy and thus gets reconstructed with a too low

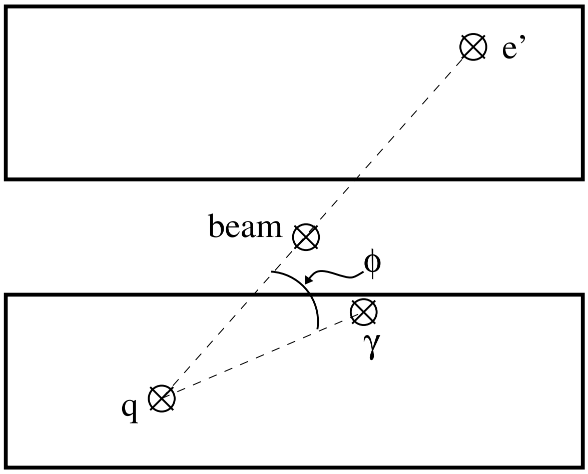


**Figure 7.6:** Visualization of a single–photon event in the HERMES acceptance.

energy. If the lepton radiates a photon while interacting with some detector material, such as the target exit window, the process is referred to as external bremsstrahlung. If it happens in the electromagnetic field of the target nucleon it is called internal bremsstrahlung. The latter process constitutes the BH process itself and is discussed in the next section.

The amount of external bremsstrahlung radiated from the incoming lepton is negligible since there is essentially no material to interact with. The effect of external bremsstrahlung radiated from the scattered lepton in the front part of the detector can be understood with the help of figure 7.6. The acceptance of the HERMES-detector is indicated with the two rectangular boxes. In the front view, the direction of the incoming lepton beam (beam), the scattered lepton ($e'$), the real ($q$) and the virtual ($\gamma$) photon are shown for a certain event. If in the same configuration the scattered lepton radiates a photon in the front region of the detector, this photon is usually almost collinear with the lepton direction. The direction of the lepton in the front region does essentially not change, but the reduced reconstructed energy leads to a reduced measured value of $Q^2$. The reconstructed direction of the virtual photon is then shifted towards the beam pipe and the measured angle $\phi$ gets enlarged. In other words, if the scattered lepton loses energy in the front region, the reconstructed angle $\phi$ is shifted towards $\pm\pi$. This behavior can be seen in the MC, but it is even visible in the data, as will be shown in the following.

As mentioned above, the lepton and the radiated photon are collinear, but this only holds true up to the magnet. While the photon traverses undisturbed, the lepton is bent and hits the calorimeter at a different position, i.e., two separate clusters can

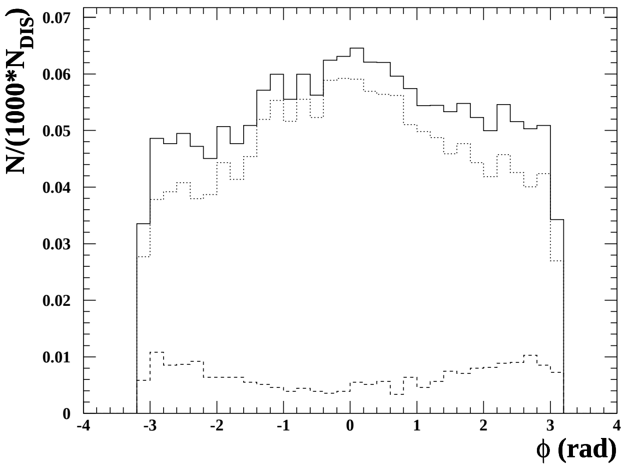


**Figure 7.7:** Exclusive single–photon yield per 1000 DIS events for the data from the year 2000 as a function of $\phi$ (solid line). The full sample is split up into one with (dashed line) and one without (dotted line) an identified additional bremsstrahlung photon.

---

be observed. HRC associates the two clusters with the front and with the back track of the lepton. Events in which external bremsstrahlung has occurred can then be identified in the $\mu$DSTs by the fact that the sum of the cluster energies associated with the lepton track differs from the energy of the cluster associated with the back partial track. Using the full single–photon sample in the exclusive bin, the two samples with and without an additional bremsstrahlung photon and their sum are shown in figure 7.7 as a function of $\phi$. It is clearly visible that the sample without an identified bremsstrahlung photon has the maximum yield around $\phi = 0$ while the one with a bremsstrahlung photon peaks at $\pm\pi$. The sum still has its maximum at zero, but the distribution did flatten out compared to the one without the additional photon, i.e., the amplitude of the cosine modulation has decreased. This implies that $\cos\phi$ moments might be affected more than $\sin\phi$ moments.

The differences between the full single–photon sample in the exclusive bin and a sample where events in which bremsstrahlung occurred are excluded, are shown in figure 7.8 for the first moments of the beam–spin and beam–charge asymmetries as functions of $-t_c$. The relative change of the moments before acceptance corrections (squares) is indeed about twice as large for the beam–charge asymmetry than for the beam–spin asymmetry when integrating over all five bins in $-t_c$. It has been mentioned above that the acceptance corrections should take care of external bremsstrahlung and smearing. Calculating and applying the acceptance corrections separately for the full single–photon sample and for the one without the identified

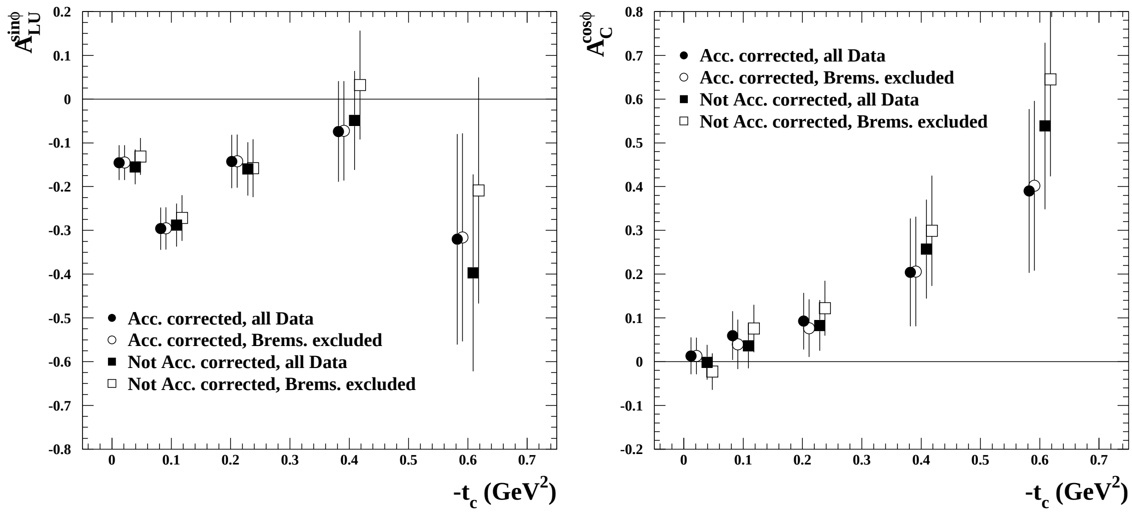


**Figure 7.8:** The $\sin\phi$ moment $A_{LU}^{\sin\phi}$ (left panel) and the $\cos\phi$ moment $A_C^{\cos\phi}$ (right panel) as a function of $-t_c$. The results are shown for the full exclusive sample (solid) and for the one without events with an identified additional bremsstrahlung photon (open) and are compared before (squares) and after (circles) acceptance corrections.

---

bremsstrahlung photons, the results (circles) nicely agree with each other as shown in the same figure. This implies that the acceptance correction indeed accounts for external bremsstrahlung. The remaining differences between the two results after acceptance corrections are calculated per bin and assigned as one component of the systematic error. The other component is due to the fact that the calculation of the acceptance moments of the HERMES detector relies on a weighting procedure at a fixed angle $\phi_c$ and this angle was quite arbitrarily chosen to be 90°. The acceptance correction has also been performed at $\phi_c = 60°$ and 170° in order to check the stability of the method. The differences between the three results are small. Nevertheless, the difference between the result at 90° and the two other results has been calculated per bin and the maximum in each bin is taken as the other component of the systematic error. Both components are added linearly since they are not independent.

### 7.2.2 Radiative Corrections

The size of possible corrections to the asymmetries due to internal bremsstrahlung, commonly referred to as radiative corrections, is difficult to determine. Theoretical

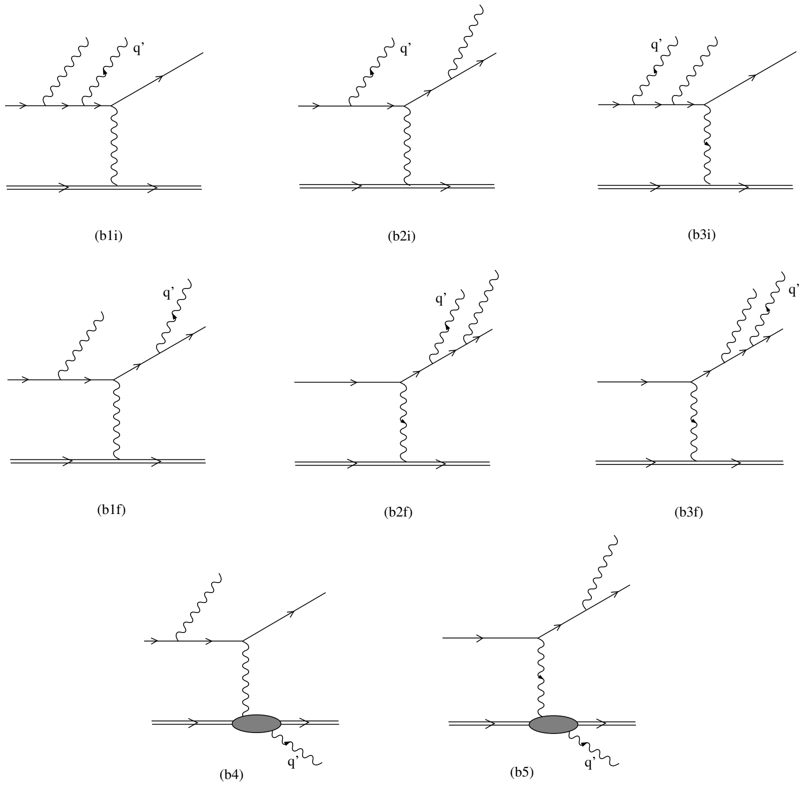


**Figure 7.9:** First order soft photon emission contribution to the $e\,p \to e\,p\,\gamma$ reaction. The hard photon is denoted by $q'$. Figure taken from reference [Van00].

estimates for the case of the beam–charge asymmetry are absent. For the beam–spin asymmetry only one theoretical calculation is available [Van00], carried out for the kinematics at Jefferson Lab. It is estimated that the $\sin\phi$ dependence cannot be changed by more than 5%. This at best is a hint on the order of magnitude of this effect at HERMES and not a valid upper limit. Besides the different average kinematics of the data samples also differences in the experimental setup play a role. They are important since the calculation of the first order soft photon contribution to the hard photon production processes shown in figure 7.9 is performed for soft photon energies of up to 100 MeV, i.e., higher energetic photons are expected to be distinguishable from single–photon events by the experimental setup. The missing mass constraint of 1.7 GeV used in this analysis gives room for additional photons of much higher energies.

In the following an attempt is made to estimate the soft photon contribution. The MC is not able to simulate the processes shown in figure 7.9 since RADGEN is only able to calculate lowest order radiative processes, i.e., the radiative correction to the first order BH processes (panels b1i–b3i, b1f–b3f) are not simulated. In addition, the DVCS process itself and consequently the radiative corrections to this process (panels b4,b5) are absent. However, a data–to–MC comparison can help to estimate the size of these radiative corrections. It has been explained in the previous section that additional bremsstrahlung photons in the final state can be identified in the data. They are due to internal and external final state bremsstrahlung, while in the MC simulation they originate from external bremsstrahlung only. Since the latter should be well simulated by GEANT, a MC–to–data comparison can be carried out. The amount of exclusive single–photon events with an identified additional bremsstrahlung photon in the data (12.2%) exceeds the one in the MC only slightly (11.9%). This means that only 0.3% of all events in the data are accompanied by an additional soft photon from internal bremsstrahlung. Since the emitted photons are restricted to small energies in order to satisfy the missing mass constraint for exclusive events, their amount depends on the missing mass reconstruction, i.e., on the correct reconstruction of the photon energy. Corrections to the measured photon energy in the 2000 data (see section 5.5.2) and to the simulated reconstructed photon energy in the MC (see section 6.2) have been applied. The amount of soft photons can increase from 0.3% to a maximum of 0.8% when varying both corrections by $\pm 1\%$ each. Taking 0.8% soft photon emission contribution in the final state as an upper limit, the initial state radiation is assumed to be not more than four times bigger. This number is achieved from the ratio of first order initial–to–final state radiation in the MC, assuming that the ratio of second order initial–to–final state radiation is similar. Internal bremsstrahlung photons in the MC were assumed to belong to the initial (final) state radiation if they have an angle of less than 30 mrad with respect to the incoming (outgoing) lepton. Small variations of this angle, of the energy range of the scattered lepton and of the upper limit on the photon energy between 0.8 GeV and 1.5 GeV showed that the factor of four always serves as an upper limit.

In summary, the maximum soft photon contribution emitted in the initial (final) state is assumed to be 3.2% (0.8%) and a change of the asymmetry on the same order is taken as systematic uncertainty. Although the resulting effects of initial and final state radiation should partially cancel each other since the reconstructed angle $\phi$ is shifted from $\pm\pi$ towards zero and from zero towards $\pm\pi$, respectively, the systematic errors are added up linearly for a conservative estimate.

### 7.2.3 Semi–inclusive and Exclusive Background

In the following the asymmetry is corrected for the semi–inclusive background. The systematic uncertainties due to the correction itself and due to the exclusive background are estimated.

The fraction of semi–inclusive events $f_{semi}$ in the exclusive sample was derived using the MC simulation described in chapter 6. The fractions per bin in $x_B$, $Q^2$ and $-t_c$ are shown in figure 6.7. The extracted asymmetry can be corrected for the semi–inclusive contribution if the asymmetry of the semi–inclusive events is known. The MC shows that the photons in the semi–inclusive background mostly stem from the $\pi^0$ meson ($> 80\%$) and that the rest is dominated by photons from the decay of the $\eta$ meson. The semi–inclusive production of these particles should not depend on the charge of the beam. It acts as a pure dilution and can be corrected according to $f_{semi}$ in every bin. Whether or not the $\pi^0$ production depends on the helicity of the beam is unknown, in particular the asymmetry carried by the one detected photon after the decay is the value of interest here. The detected photon usually is the higher energetic (leading) one, since the event is reconstructed with a missing mass in the exclusive region despite the fact that only one photon from the $\pi^0$ decay is detected. As a consequence, it might well carry a part of the $\pi^0$ azimuthal dependence if there is one. In order to estimate the size of the beam–spin asymmetry in $\pi^0$ production, the single–photon analysis as described above has been carried out for the data from 2000 in a similar manner for $\pi^0$ mesons. The only differences are that events with exactly two photons in the final state have been selected and that the two photons are required to have an invariant mass between 0.1 GeV and 0.17 GeV. The lower energetic photon is afterwards dismissed and the usual single–photon analysis is carried out with the leading photon. In order to maximize the available statistics, the upper limit on $\theta_{\gamma^*\gamma}$ and on $-t_c$ is discarded. In addition, the signal in the preshower detector is not obligatory here. The resulting $\sin\phi$ moment for the leading photon is shown in figure 7.10. It is obvious that the available statistics do not allow for a bin by bin correction of the measured asymmetry. Since no strong kinematic dependence on $x_B$, $Q^2$ and $-t_c$ can be observed, the integrated value of the asymmetry is used instead. The integrated $\sin\phi$ ($\sin 2\phi$) asymmetry of $-0.030 \pm 0.194$ ($0.330 \pm 0.195$) is the result for a mixture of semi–inclusive and exclusive $\pi^0$ mesons. However, the statistical error is large and is therefore expected to cover the true asymmetry of the semi–inclusive events. The same check has been carried out for semi–inclusive $\eta$ production but is inconclusive due to a lack of statistics. Since $\eta$ production contributes only about 15% to the semi–inclusive sample it is assumed that it can alter the extracted asymmetry from the leading $\pi^0$ decay photon, also referred to as $\pi^0$ asymmetry in the following, only

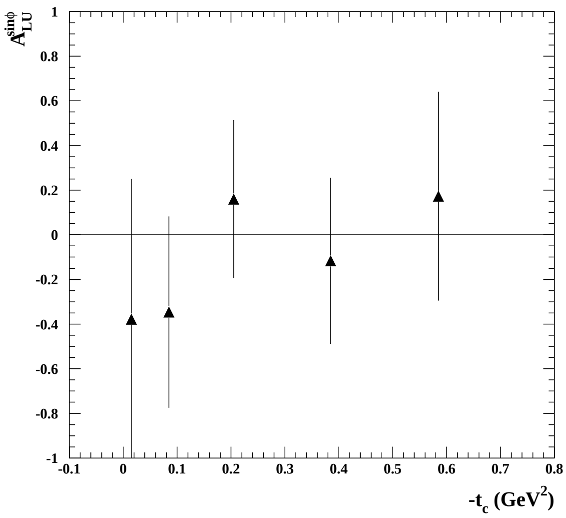


**Figure 7.10:** The $\sin\phi$ moment $A_{LU}^{\sin\phi}$ for the leading photon from the $\pi^0$ decay as a function of $-t_c$.

within the statistical errors. Each bin is therefore corrected by the value of the extracted integrated $\pi^0$ asymmetries. Setting $A_{semi}$ equal to these asymmetries for the $\sin\phi$ and $\sin 2\phi$ moments or equal to zero for the moments of the beam–charge asymmetry, the correction to the measured asymmetry

$$A^i_{meas} = (1 - f^i_{semi})A^i_I + f^i_{semi}A_{semi} \tag{7.12}$$

can be carried out in each bin $i$. Using the fractions $f^i_{semi}$ per kinematic bin i given in figure 6.7, the BH–DVCS interference asymmetries per bin $A^i_I$ can be derived via equation 7.12.

The systematic error of the applied background correction is investigated below. It consists of two components, the systematic plus statistical error of the fractions $f^i_{semi}$ and the statistical uncertainty of the $\pi^0$ asymmetry $A_{semi}$. The systematic uncertainty of the fractions $f^i_{semi}$ needs to take into account the reliability of the MC simulation itself. In order to get good agreement between MC and data in the semi–inclusive region, a reweighting procedure has been performed (see section 6.3). The applied weight per event was derived using an event sample satisfying the requirement $M_x^2 > 5$ GeV$^2$. This constraint was chosen slightly arbitrarily. Varying this value between 3 and 9 GeV$^2$, the derived semi–inclusive contribution of 4.9% varies between 4.9% and 5.5%, respectively. This corresponds to a possible increase of the background by up to 11%. On the other hand, the DVCS reaction itself and the exclusive production of the $\pi^0$ was not taken into account in the calculation of the fractions. Including more processes leads to a decrease of the semi–inclusive background contribution. Figure 3.3 shows for a fixed kinematic setting close to the average kinematics of this analysis, that the DVCS process is more than an order of magnitude smaller than the BH contribution in the region $|\theta_{\gamma^*\gamma}| < 0.045$ mrad. Note that $\theta_{\gamma^*\gamma}$ can become negative only in the specific definition used for that figure. Together with an estimated conservative upper limit of 2.5% for the exclusive $\pi^0$ contribution [Ely02a], the decrease of the semi–inclusive contribution cannot exceed 11% either. It is therefore concluded that the fractions of the semi–inclusive background per bin have a systematic uncertainty of $\pm 11\%$. The statistical uncertainty of each fraction per bin is added in quadrature to this systematic uncertainty. The first component of the systematic uncertainty on the background correction is thus derived by varying each fraction $f^i_{semi}$ by adding or subtracting its systematic uncertainty and calculating the corresponding two corrected asymmetries according to equation 7.12. The maximum deviation between these two results and the actual corrected asymmetry value is taken as first component of the systematic uncertainty of the background correction. In the same manner the second component is derived by varying the semi–inclusive asymmetry $A_{semi}$ itself by its statistical error which is non–zero for the $\sin\phi$ ($\sin 2\phi$) moments only.

A reliable MC description of the fractional contribution of the exclusive $\pi^0$ in every bin is not yet available. A conservative upper limit on the overall contribution of 2.5% has been estimated in [Ely02a]. Assuming that the beam–spin and beam–charge asymmetries resulting from the exclusive $\pi^0$ production are equal to $A_{semi}$ within its errors and that the contribution per bin does not exceed 2.5%, the maximal possible correction to the asymmetry $A^i_I$ is calculated per bin and taken as the systematic uncertainty for the exclusive background contribution.

### 7.2.4 Calorimeter Calibration

An observed shift between the missing mass squared distributions from the electron (1998) and the positron (2000) data (see figure 5.4) was corrected by increasing the photon energies given in the $\mu$DST–files from the 2000 data by 1% (see section 5.5.2). The beam–charge asymmetry is sensitive to this factor since increasing (decreasing) the photon energy for the 2000 data leads to a larger (smaller) number of events in the exclusive bin and to a worse (better) signal–to–background ratio. In addition, since the cross section integrated over the angle $\phi$ is not the same for the two beam charges due to the $\phi$–independent term $c^I_0$, a difference in the number of exclusive events $N$ in one data sample directly enters the calculation of the moments in equation 7.6. In contrast to the beam–charge asymmetry, the beam–spin asymmetry should be insensitive to this correction since the cross sections are the same in both helicity samples and thus a change in the number of events $N$ cancels in the calculation of their moments (see equation 7.4). Moreover, since the beam–spin asymmetry is calculated from data of the same running period, the number of exclusive events and hence the signal–to–background ratio in both helicity samples change in the same way for different calorimeter calibrations. The amount of background in the exclusive bin and the systematic uncertainty on this quantity was already accounted for in the previous section.

While the correction of 1% was achieved using the ratio $E/P$ for leptons, i.e., the method how the calorimeter is calibrated, the relative calorimeter calibration between the two running periods can also be checked using the invariant mass of reconstructed $\pi^0$ mesons. The result implies an increase of the photon energies in 2000 by another 0.7%, i.e., the total correction is 1.7%. Taking the difference between the two methods as systematic error, the moments of the beam–charge asymmetry are calculated for corrections of 0.3 and 1.7% and the maximum deviation to the actual result in each bin is taken as its systematic error.

### 7.2.5 Beam Polarization

The beam polarization measurements were carried out by both polarimeters (see section 4.1.1) in parallel during most of the time in the 2000 running period. For every burst, the polarimeter group specifies the polarimeter from which the measured value should be taken from. This usually is the longitudinal polarimeter (LPOL) since it has a smaller systematic uncertainty (1.6%). Only if the LPOL shows problems during operation, the values from the transverse polarimeter (TPOL) with a systematic uncertainty of 3.4% are taken. The resulting systematic error of 1.9% for the beam polarization measurement is given by the fractional use of LPOL and TPOL in the 2000 running period. The systematic error to the beam–spin asymmetry is then 1.9% of the asymmetry in the respective bin.

### 7.2.6 Asymmetries of the Associated Processes

After applying the semi–inclusive background correction, the corrected value of the asymmetry $A_I^i$ in each bin $i$ should originate from the BH–DVCS interference alone. This asymmetry gets contributions from both, the elastic and the associated processes, also referred to as elastic and associated asymmetry in the following. The asymmetry from the associated processes $A_{asso}$ is unknown, only first model calculations have been performed [Gui03]. They indicate that the associated asymmetry, just as the elastic asymmetry, is strongly model dependent. A further discussion follows in chapter 9.

A possible way to disentangle the contributions from the elastic and the associated processes is given in the following. The data sample can be subdivided in two samples and the two corresponding asymmetries

$$A_I^1 = f_{I,elas}^1 A_{elas}^1 + f_{I,asso}^1 A_{asso}^1, \quad (7.13)$$
$$A_I^2 = f_{I,elas}^2 A_{elas}^2 + f_{I,asso}^2 A_{asso}^2 \quad (7.14)$$

can be extracted. The fractional contributions from the elastic ($f_{I,elas}$) and from the associated ($f_{I,asso}$) interference are unknown. Under the assumption that the cross section ratios between the elastic and the associated processes are about the same for the BH and the DVCS processes, i.e., $\sigma_{BH,elas}/\sigma_{BH,asso} \approx \sigma_{DVCS,elas}/\sigma_{DVCS,asso}$, the ratio between the elastic and the associated contribution of the interference term is the same as well. As a consequence, the fractional elastic and associated BH contributions are approximately of the same size as the corresponding ones from the interference contribution, i.e., $f_{BH,elas} \approx f_{I,elas}$ and $f_{BH,asso} \approx f_{I,asso}$. Therefore the fractions of the elastic and the associated contributions for the two samples in the equations 7.13 and 7.14 can be derived using the MC as described in chapter 6. The second assumption needed is $A_{elas}^1 \approx A_{elas}^2$ and $A_{asso}^1 \approx A_{asso}^2$. This is only true if the asymmetries are either independent of the kinematic variables or if the average kinematics in the two chosen samples are about the same, at least for the variables where a strong dependence is expected. The $\cos\phi$ moment of the beam–charge asymmetry seems to clearly depend on $-t_c$ but not too strongly on $Q^2$ and $x_B$. Assuming that the associated asymmetry has a similar behavior, two samples from different missing mass regions but with about the same average $-t$ have been selected. Note that the measured $t$ is used here since the use of $t_c$ would automatically set the missing mass equal to the proton mass. Using samples from different missing mass regions yields the advantage that they have quite different values for the fractional elastic and associated contributions. The equations 7.13 and 7.14 can now be solved. It turns out, however, that the error on the extracted associated asymmetry $A_{asso}$ covers the full possible range between -1 and +1 due to lack of statistics.

It is possible to calculate a systematic uncertainty for the associated asymmetry, assuming $A_{asso}$ within a certain range of values. Unfortunately, the first model calculations carried out [Gui03] used only one model and one kinematic setting. In addition, they are only done for the first moments. The underlying code was made available [Van03], but is exhaustive in the use of computing time and thus only some first calculations have been carried out. The possible influence of the associated asymmetries will be discussed in chapter 9 for the first moments, but a consistent discussion or calculation of a systematic uncertainty for all moments and different kinematics is not possible at present. The resulting moments of the asymmetries given in the next chapter are thus derived from the unseparated data sample that comprises the contributions from both the elastic and the associated BH–DVCS interference.

### 7.2.7 Combined Systematic Uncertainties

An example for the systematic errors from the various sources discussed above is given in table 7.2 per bin in $-t_c$ for the first moment of the beam–spin (BSA) and the beam–charge (BCA) asymmetry. The main contributions to the systematic uncertainty of the $\sin\phi$ moment are given by the poorly known beam-spin asymmetry of the semi–inclusive background and by the exclusive background. These are also the major sources for the uncertainty of the $\sin 2\phi$ moment. The systematic uncertainty of the first and of the higher moments of the beam–charge asymmetry is dominated by acceptance effects for small values of $-t_c$. At large values of $-t_c$ the uncertainty gets the strongest contribution from the difference in the calorimeter calibration since a small increase (decrease) in the reconstructed photon energy mostly adds (removes) events with a larger value of $-t_c$ to (from) the exclusive sample. The constant term of the beam–charge asymmetry is directly sensitive to this yield difference in the exclusive sample for the two different years. It is estimated that the uncertainty from the calorimeter calibration exceeds the combined systematic error of the other sources by a factor of two. Thus it did not appear necessary to take the other systematic error sources into account for the constant term, especially since its extracted values are compatible with zero already within their statistical errors in almost all kinematic bins.

The remaining question is whether or not the separate sources of systematic errors are correlated, i.e., whether they should be added linearly or in quadrature. The acceptance effects and the radiative corrections should not be strongly correlated. However, the two systematic uncertainties have not been derived independently. The same holds true for the semi–inclusive and the exclusive background. The two sources from the semi–inclusive background are definitely correlated. The combined systematic uncertainty is therefore obtained by adding linearly the uncertainties from the acceptance and the radiative corrections, adding linearly the systematics from the background sources and afterwards adding in quadrature the resulting two uncertainties together with the one from the calorimeter calibration and from the

| BSA: $-t_c$ bin | 1 | 2 | 3 | 4 | 5 | Int |
|---|---|---|---|---|---|---|
| Acc+Brems+Smear | 0.000 | 0.001 | 0.001 | 0.001 | 0.006 | **0.001** |
| Radiative Corr | 0.006 | 0.013 | 0.006 | 0.003 | 0.014 | **0.008** |
| $f_{semi}$ | 0.001 | 0.003 | 0.001 | 0.001 | 0.009 | **0.002** |
| $A_{semi}$ | 0.006 | 0.012 | 0.014 | 0.018 | 0.018 | **0.010** |
| exclusive Backg | 0.008 | 0.012 | 0.008 | 0.006 | 0.012 | **0.009** |
| Calo Calibration | - | - | - | - | - | **-** |
| Beam Polarization | 0.003 | 0.006 | 0.003 | 0.002 | 0.007 | **0.004** |
| **Combined Sys.** | **0.016** | **0.030** | **0.025** | **0.025** | **0.045** | **0.023** |

| BCA: $-t_c$ bin | 1 | 2 | 3 | 4 | 5 | Int |
|---|---|---|---|---|---|---|
| Acc+Brems+Smear | 0.001 | 0.021 | 0.017 | 0.005 | 0.016 | **0.010** |
| Radiative Corr | 0.001 | 0.003 | 0.004 | 0.009 | 0.017 | **0.003** |
| $f_{semi}$ | 0.000 | 0.001 | 0.001 | 0.004 | 0.013 | **0.001** |
| $A_{semi}$ | - | - | - | - | - | **-** |
| exclusive Backg | 0.000 | 0.002 | 0.002 | 0.005 | 0.010 | **0.002** |
| Calo Calibration | 0.003 | 0.004 | 0.010 | 0.027 | 0.056 | **0.007** |
| Beam Polarization | - | - | - | - | - | **-** |
| **Combined Sys.** | **0.003** | **0.024** | **0.023** | **0.032** | **0.069** | **0.015** |

**Table 7.2:** Systematic errors per bin in $-t_c$ for the first moment of the beam–spin (upper table) and the beam–charge asymmetries (lower table). The uncertainties on the asymmetries are due to the acceptance correction including effects from external bremsstrahlung and smearing (Acc+Brems+Smear), due to radiative corrections (radiative Corr), due to the uncertainty of the amount ($f_{semi}$) and asymmetry ($A_{semi}$) of the semi–inclusive background when applying the background correction, due to exclusive background (exclusive Backg), due to the different calorimeter calibration in different years (Calo Calibration) and due to the uncertainty in the beam polarization measurement (Beam Polarization).

beam polarization in quadrature.

### 7.2.8 Statistical Uncertainty

The statistical uncertainty of an extracted moment can be calculated in two different ways. The estimator formalism developed in [Bes79] uses the formula

$$\sigma^2_{stat} = \frac{2}{N}(1 - \epsilon^2/2), \tag{7.15}$$

where N is the number of counts and $\epsilon$ is the value of the extracted moment of the asymmetry. The other way is to use the spread in the calculated mean. For a $w(\phi)$ moment given by

$$A^{w(\phi)} = \frac{2}{N}\sum_{i=1}^{N} w(\phi_i), \tag{7.16}$$

the uncertainty is given by

$$\sigma^2_{stat} = \frac{4}{N-1}\left(\overline{w^2(\phi)} - \overline{w(\phi)}^2\right), \tag{7.17}$$

where $\overline{w^2(\phi)} = \sum w^2(\phi_i)/N$ and $\overline{w(\phi)} = \sum w(\phi)/N$. Note that in the above equations the beam polarization needs to be included in the case of the beam–spin asymmetry.

Both equations yield the same statistical error as long as the extracted moments are small. As soon as the moments become large, equation 7.15 breaks down. This is not a problem for the $\sin\phi$ moments as they are always quite small. The $\cos\phi$ moments, on the other hand, can become large for the separate charges due to acceptance effects, as shown in the left panel of figure 7.4. Hence, the statistical error for all moments is calculated using equation 7.17 for consistency.

# Chapter 8

# Results

All relevant moments of the beam–charge and beam–spin asymmetries have been extracted in dependence on several kinematic variables. The data was collected by the HERMES collaboration using an unpolarized hydrogen target. The results are given in this chapter. Their interpretation including a comparison to model calculations follows in the next chapter.

The measurement of the beam–spin asymmetry (BSA) is based on data collected in 2000 using a polarized positron beam, the beam–charge asymmetry (BCA) is based on the same data set together with data taken with an electron beam in 1998. An exclusive single–photon sample satisfying certain constraints has been selected. The asymmetries were extracted as functions of the kinematic variables $x_B$, $Q^2$ and $-t_c$, whereby the respective other two variables were integrated over. The numerical results on all measured asymmetries per kinematic variable are presented in appendix A. The range of these variables was restricted as follows:

$$\begin{aligned} 0.03 < x_B &< 0.35, \\ 1\ \mathrm{GeV}^2 < Q^2 &< 10\ \mathrm{GeV}^2, \\ -t_c &< 0.7\ \mathrm{GeV}^2. \end{aligned}$$

For the beam–spin asymmetry the exclusive single–photon sample contains 4014 events in the positive helicity state and 5373 events in the negative helicity state. For the beam–charge asymmetry samples of 715 events taken with an electron beam and 9516 events taken with a positron beam have been selected. The average values of the kinematic variables for the exclusive sample are:

$$\begin{aligned} \langle\, x_B \,\rangle &= 0.09, \\ \langle\, Q^2 \,\rangle &= 2.5\ \mathrm{GeV}^2, \\ \langle\, -t_c \,\rangle &= 0.11\ \mathrm{GeV}^2. \end{aligned}$$

| | A $\pm$ (stat.) $\pm$ (sys.) |
|---|---|
| $A_C^{\cos\phi}$ | 0.068 $\pm$ 0.030 $\pm$ 0.015 |
| $A_{LU}^{\sin\phi}$ | -0.195 $\pm$ 0.028 $\pm$ 0.023 |
| $A_C^{\cos 2\phi}$ | 0.026 $\pm$ 0.029 $\pm$ 0.008 |
| $A_{LU}^{\sin 2\phi}$ | -0.063 $\pm$ 0.029 $\pm$ 0.030 |
| $A_C^{\cos 3\phi}$ | 0.063 $\pm$ 0.028 $\pm$ 0.008 |
| $A_C^{const}$ | 0.027 $\pm$ 0.019 $\pm$ 0.014 |

**Table 8.1:** Moments of the beam–charge and of the beam–spin asymmetry, integrated over the full kinematic range. The results per kinematic bin in $x_B$, $Q^2$ and $-t_c$ are given in appendix A.

---

The extracted $\cos\phi$ moments of the beam–charge asymmetry are shown in the left panels of figure 8.1 in dependence on $-t_c$, $x_B$ and $Q^2$. This data constitutes the only performed measurement of the beam–charge asymmetry. An intermediate result of this analysis [Ell02b] yielded a preliminary integrated value of 0.11 $\pm$ 0.04 (stat.) $\pm$ 0.03 (sys.) at the average kinematics $\langle\, x_B \,\rangle = 0.12$, $\langle\, Q^2 \,\rangle = 2.8$ GeV$^2$ and $\langle\, -t \,\rangle = 0.27$ GeV$^2$. At first glance the integrated present result given in table 8.1 appears different, however, while the average values of $x_B$ and $Q^2$ did barely change this is not true for $t$. The average $-t$ value became much smaller, mainly due to the fact that events with small angles $\theta_{\gamma^*\gamma}$ between the virtual and the real photon have been included in this analysis, i.e., it is not caused by using $-t_c$ in this analysis instead of the measured $-t$ value. The $\cos\phi$ moment shows a strong $t_c$–dependence displayed in the upper left panel of figure 8.1. At small values of $-t_c$ it is compatible with zero and becomes sizeable and positive only at higher $-t_c$ values. The average kinematics in the third $-t_c$ bin (see table A.1) are closest ($\langle\, x_B \,\rangle = 0.11$, $\langle\, Q^2 \,\rangle = 3.0$ GeV$^2$ and $\langle\, -t_c \,\rangle = 0.20$ GeV$^2$) to the ones from the intermediate result of this analysis. The asymmetry value in this bin (0.100 $\pm$ 0.070 (stat.) $\pm$ 0.021 (sys.)) is compatible to the earlier result.

The $\sin\phi$ moments of the beam–spin asymmetry are shown in the right panels of figure 8.1 as a function of $-t_c$, $x_B$ and $Q^2$. The result integrated over the full kinematic range is shown in table 8.1. It can be compared to the already published integrated values from HERMES ($-0.23 \pm 0.04$ (stat.) $\pm$ 0.03 (sys.)) and CLAS (0.202 $\pm$ 0.028 (stat.) $\pm$ 0.013 (sys.)). It has been mentioned in section 3.4.2 that the latter two results agree with each other within errors although they are obtained at quite different average kinematics, especially in $x_B$ and $Q^2$. Looking at the asymmetry as a function of $x_B$ and $Q^2$ in the middle and lower right panels, respectively,

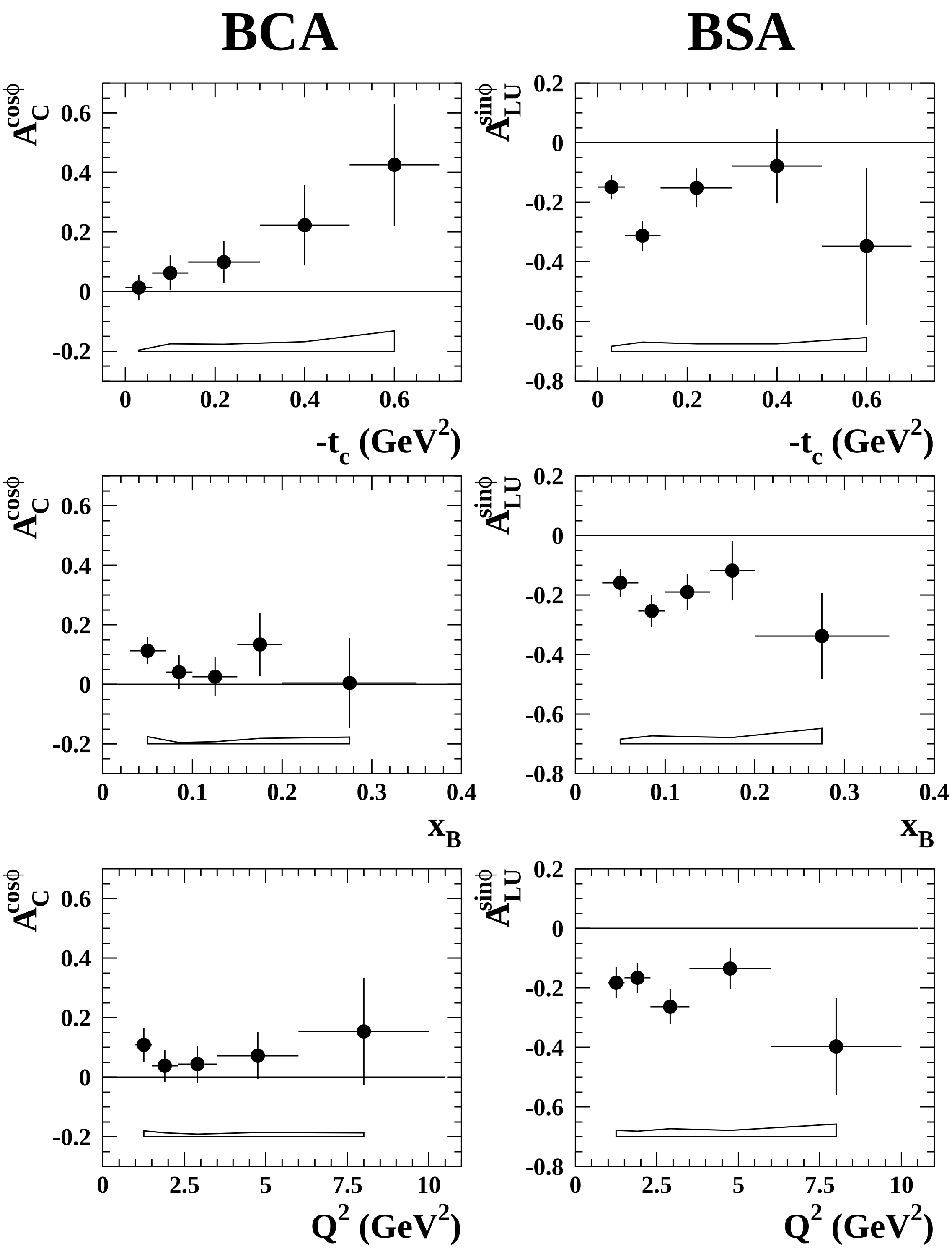


**Figure 8.1:** The $\cos\phi$ moment of the beam–charge asymmetry (BCA, left panels) and the $\sin\phi$ moment of the beam–spin asymmetry (BSA, right panels) as functions of $-t_c$, $x_B$ and $Q^2$.

these dependences appear to be not very strong. Especially the changes in the asymmetry between the average values in $x_B$ (HERMES: 0.11, CLAS: $\approx$ 0.19) and $Q^2$ (HERMES: 2.6 GeV$^2$, CLAS: $\approx$ 1.25 GeV$^2$) are small. Since the $t_c$–dependence does not seem to be strong either, the integrated published results should yield similar results, taking into account that the different sign of the results at HERMES and CLAS is due to the different beam charges. Consequently, the integrated result of this analysis, performed at a much smaller average value of $-t_c$ when compared to the published HERMES result, does agree as expected with both previous results. The data used for the published HERMES result has also been used to obtain a preliminary result [Ely02b] on the kinematic dependences of the $\sin\phi$ moment. With the statistical and systematic errors in this preliminary result being more than twice as large as the ones from this analysis, the results are in agreement.

The second moments of the beam–spin and the beam–charge asymmetry are displayed in figure 8.2. They do not show a clear dependence on any of the kinematic variables. The integrated values of both second moments (see table 8.1) are reduced to about 1/3 with respect to their first moments. The $\cos 2\phi$ moment is compatible with zero within errors. The $\sin 2\phi$ moment is still sizeable, although the systematic error for this particular moment is quite large due to the poorly known $\sin 2\phi$ moment of the background when carrying out the background corrections (see section 7.2.3). The CLAS collaboration also included a $\sin 2\phi$ component in their fit to the asymmetry (see section 3.4.2). Note that both results should have a different sign due to the different beam charges used in the two measurements. Although this is not the case, the CLAS result ($-0.024 \pm 0.021$ (stat.) $\pm 0.009$ (sys.)) is consistent with zero within errors and thus in agreement with this analysis, especially in view of the fact that in the $Q^2$ region of the CLAS measurement ($1 < Q^2 < 1.75$ GeV$^2$) the $\sin 2\phi$ moment of this analysis is compatible with zero even within statistics, as can be seen from the lower right panel of figure 8.2.

The $\cos 3\phi$ moment of the beam–charge asymmetry is shown in the left panels of figure 8.3. The integrated value (see table 8.1) is not compatible with zero within errors. Although no clear dependence of the third moment on the kinematic variables can be observed, the non–zero $\cos 3\phi$ moment seems to be apparent at small values of $Q^2$ taking into account that the first bin in $x_B$ has a small average $Q^2$ value as well (see table A.5). The right panels show the $\phi$–independent term of the beam–charge asymmetry. It is consistent with zero in essentially all kinematic bins.

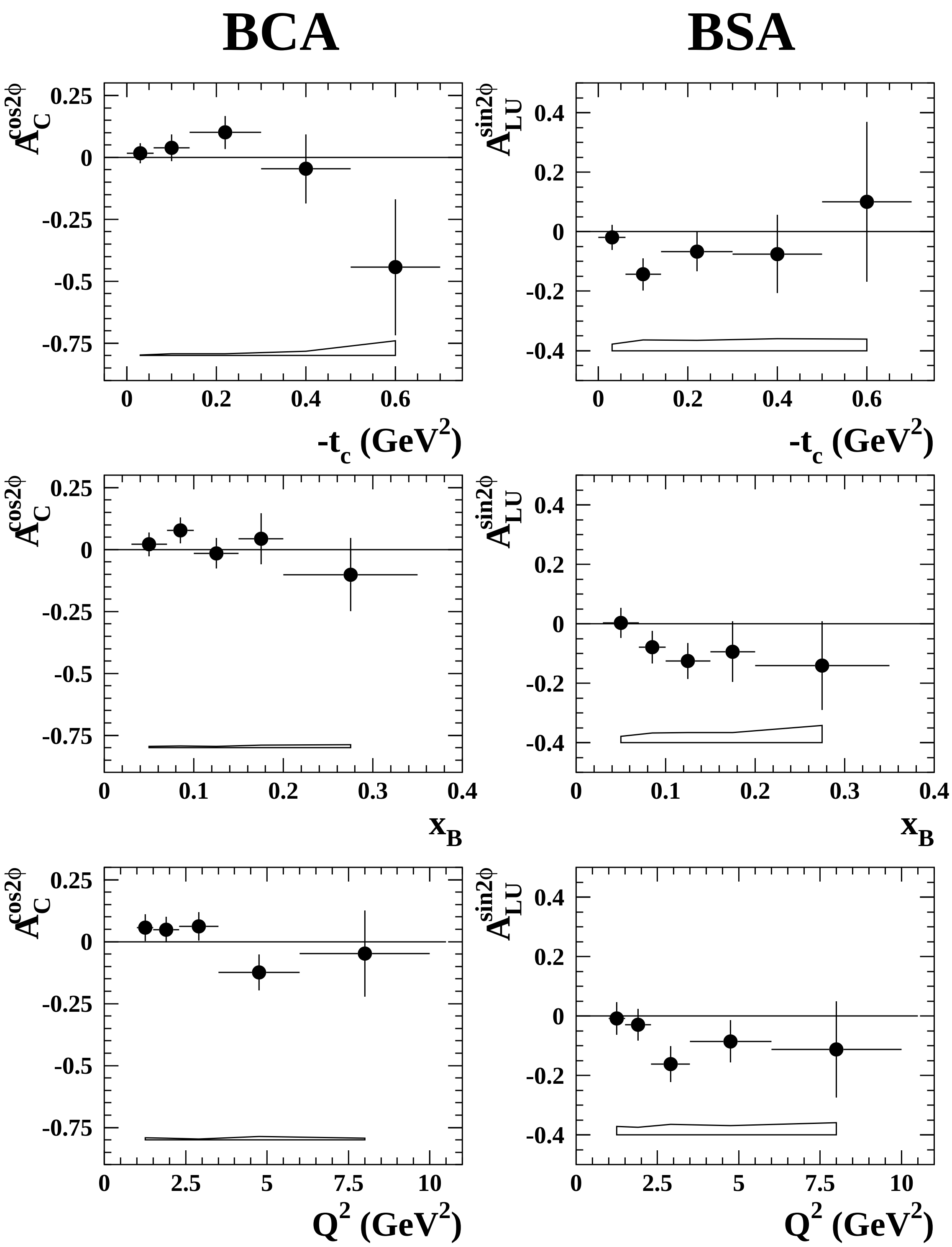


**Figure 8.2:** The $\cos 2\phi$ moment of the beam–charge asymmetry (BCA, left panels) and the $\sin 2\phi$ moment of the beam–spin asymmetry (BSA, right panels) as functions of $-t_c$, $x_B$ and $Q^2$.

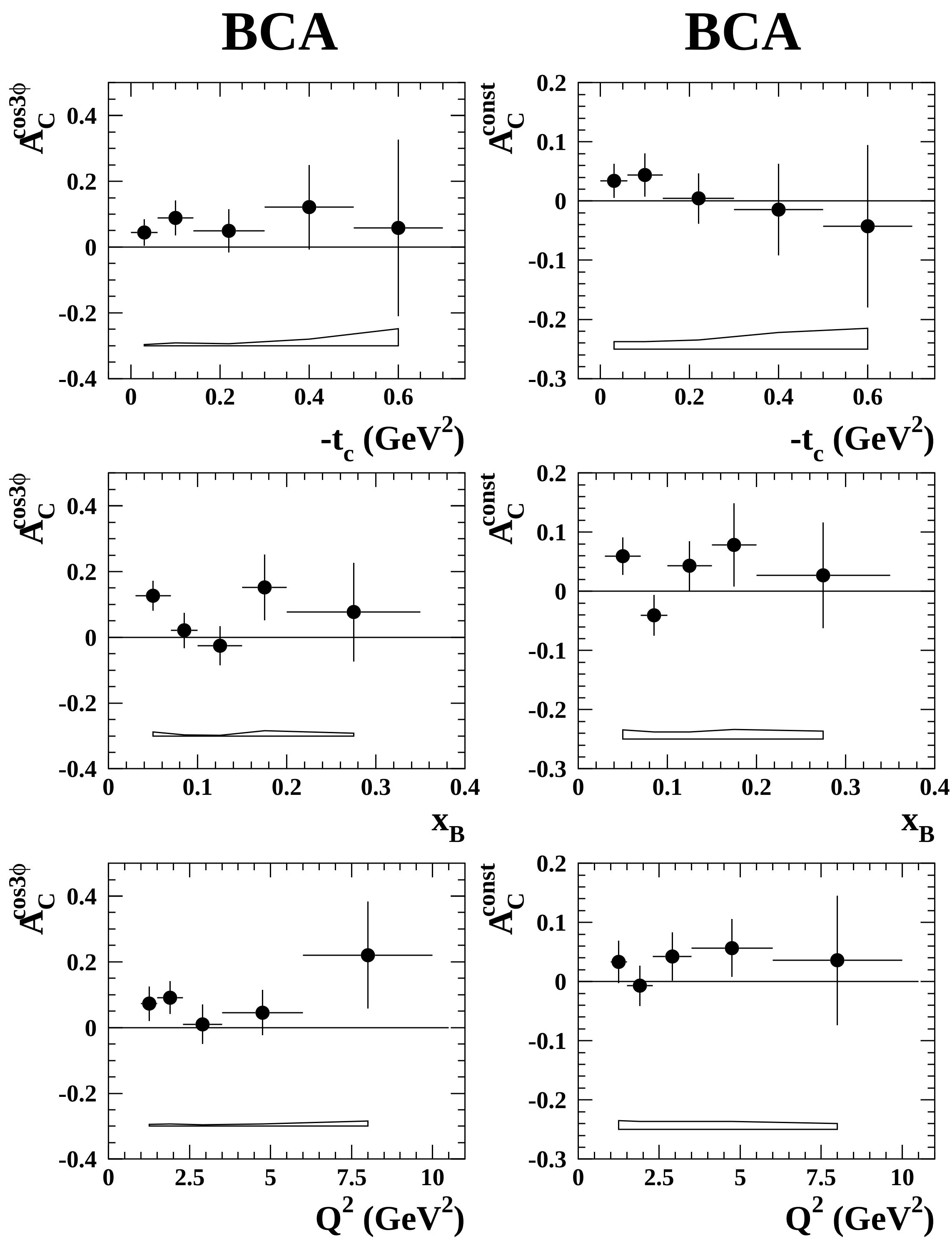


**Figure 8.3:** The $\cos 3\phi$ moment of the beam–charge asymmetry (BCA, left panels) and its $\phi$–independent part (BCA, right panels) as functions of $-t_c$, $x_B$ and $Q^2$.

# Chapter 9

# Model Calculations and Interpretation

In the following the results displayed in the last chapter will be compared to model calculations and interpreted.

## 9.1 Model Calculations

A common way of modeling GPDs is to use a phenomenological parametrization, as described in detail in section 2.2, following the model developed in references [Van99, Kiv01a, Goe01]. The underlying code is available [Van01] and was used to calculate, for various parameter settings, the predicted values for the asymmetries shown in the last chapter at the average kinematics of every bin. Note that in the following, specific sets of parameters for this model are called models as well. In order to reduce the large number of adjustable parameters to a manageable set, the parameters leading to sizeable changes in the asymmetries of interest were selected. At leading twist, the contribution of the CFF $\tilde{H}_1$ ($E_1$) and consequently the contribution of the GPD $\tilde{H}$ ($E$) is kinematically suppressed compared to the GPD $H$ by at least an order of magnitude at the average value of $x_B$ ($t$) of this data set (see equation 3.19). Possible effects of the GPDs $\tilde{H}$ and $E$ may become visible in the last bin where the respective values of $x_B$ and $-t_c$ become large. The differences in the predicted values between neglecting the contribution of these GPDs or not were found to be negligible compared to the large statistical errors of the data in the last bin in $x_B$ and $-t_c$. Since the CFF $\tilde{E}_1$ does not contribute at leading twist (see equation 3.19), for all GPDs but $H$ the parameters were fixed at their standard values.

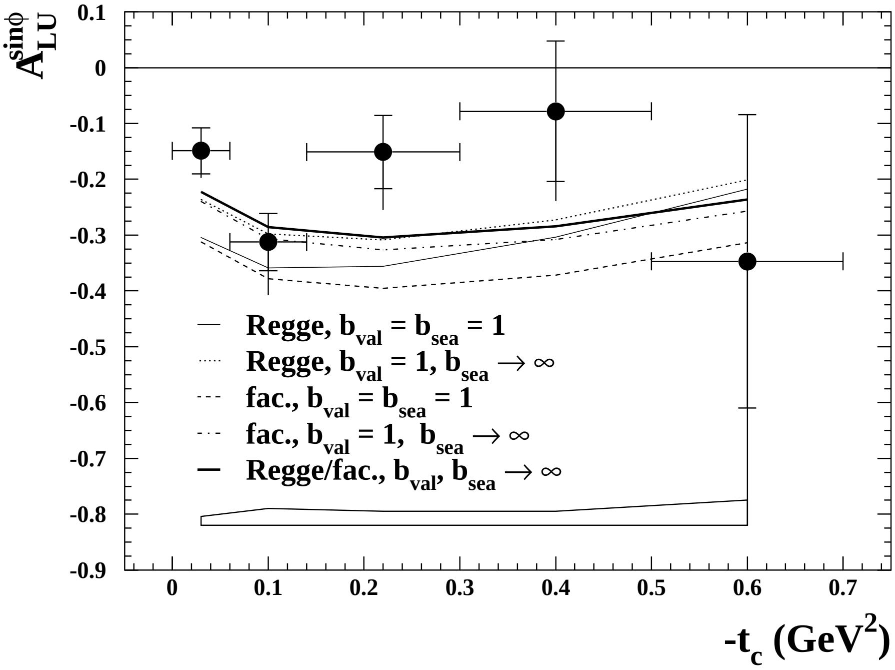


**Figure 9.1:** Model calculations and experimental results for the $\sin\phi$ moment of the beam–spin asymmetry as a function of $-t_c$. See text for details.

---

The $t$–independent part of the GPD $H$ is modified by incorporating or neglecting the D–term contribution to the double distribution part of the GPD, as explained in section 2.2.1. In addition, it was mentioned there that the parameters $b_{val}$ and $b_{sea}$ in the profile function (see equation 2.22) can be used as fit parameters. The $t$–dependence of the GPD $H$ is calculated in either the simplest ansatz where the $t$–dependence factorizes from the $t$–independent part $H^q(x, \xi)$ (see equations 2.25–2.27) or in the Regge–motivated ansatz (see equation 2.28).

In order to have as few free parameters as possible to start with, the $\sin\phi$ moment of the beam–spin asymmetry is confronted with the results from the model calculations first. This is advantageous since the beam–spin asymmetry is essentially insensitive to the D–term as explained in section 3.3.4. The $\sin\phi$ moment is calculated for every bin in $-t_c$ at its respective average values of $-t_c$, $x_B$ and $Q^2$, as given in table A.2, for six different sets of parameters. They are compared to the data in figure 9.1. The asymmetric systematic error added to the statistical error bar is achieved under the assumption that the asymmetry of the associated DVCS–BH interference has a value in between the elastic asymmetry, i.e., no systematic uncertainty, and zero. This assumption seems to be justified for the $\sin\phi$ moment by first model calculations

[Gui03] for the associated production of pions in the processes $ep \to e\gamma\pi^0 p$ and $ep \to e\gamma\pi^+ n$. These calculations directly relate the associated DVCS processes to the GPDs in the nucleon and were found to be valid up to a cutoff value of $W = 1.35$ GeV. Using the MC, it has been shown in section 6.2 that only 60% of the background from the resonance region resides below $W = 1.35$ GeV. However, the associated asymmetry would need to change quite dramatically above $W = 1.35$ GeV in order to have an integrated value not in the region between the elastic asymmetry and zero. Another uncertainty arises from the fact that the calculations for the associated pion production [Gui03] have been performed only for the simplest model (factorized $t$, $b_{val} = b_{sea} = 1$). It can be seen in figure 9.1 that at least for the $\sin\phi$ moment arising from the elastic processes the results from the other model calculations are similar compared to the result from the simplest one (dashed line). It is reasonable to assume that this holds true for the associated production as well and thus the systematic uncertainty assigned should be a valid upper limit.

Even with this systematic error included, all six models represented by five model curves shown in figure 9.1 tend to undershoot the data. However, paying attention to the first $-t_c$ bin a clear discrepancy is only found for the two models with $b_{val} = b_{sea} = 1$. The Regge and the factorized ansätze with a large value of $b_{sea}$ are not excluded by the data, especially when taking the systematic error into account. The fifth model with $b_{val}, b_{sea} \to \infty$, i.e., a $\xi$–independent GPD ansatz as explained in section 2.2.1, is not excluded either. This model curve represents both the Regge and the factorized ansatz since a noticeable difference in the predicted results is found for the last $t_c$ bin only. The result of a calculation with an increased value of $b_{val}$ but $b_{sea} = 1$ (not shown) yields approximately the same result as the calculation with $b_{val} = b_{sea} = 1$, independently of the ansatz used for the $t$–dependence.

The results of the model calculations for the beam–spin asymmetry shown in figure 9.1 are independent of whether or not the D–term is included. This is not true anymore for the model calculations of the $\cos\phi$ moment of the beam–charge asymmetry displayed in figure 9.2. The six models are now shown with and without the D–term contribution. As for the $\sin\phi$ moment, the additional systematic uncertainties are calculated under the assumption that the integrated asymmetry of the associated BH–DVCS interference processes lies in between that of the elastic asymmetry and zero. This assumption is derived using the same line of arguments as above, but it yields one complication. The elastic asymmetry varies substantially, depending on the used model, as seen in the figure. Moreover, it has been shown [Gui03] that the associated beam–charge asymmetries do not have a common behavior. While the asymmetry in neutral pion production changes depending on whether the D–term is taken into account or not, the asymmetry in charged pion production does

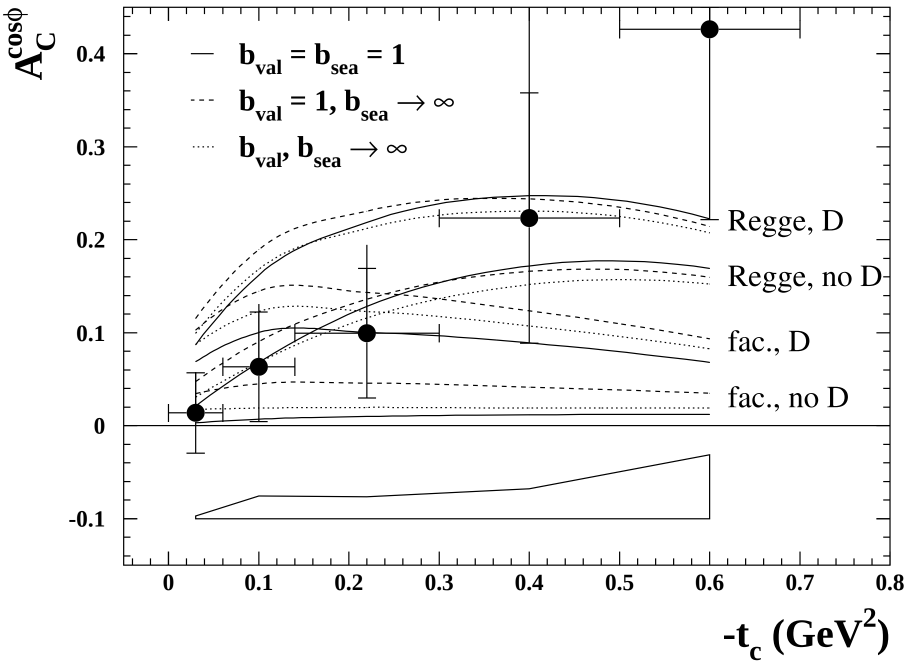


**Figure 9.2:** Model calculations and experimental results for the $\cos\phi$ moment of the beam–charge asymmetry as a function of $-t_c$. See text for details.

essentially not depend on it. Although the underlying computer code for the associated production became available only recently [Van03], some first checks for a few models and kinematic settings could be carried out in the context of this thesis. They confirm that the combined associated asymmetry still has a value in between that of the elastic asymmetry and zero. Note that from another very recent calculation [Che03] it was concluded that the DVCS amplitudes for associated pion production are not related to the nucleon GPDs, in contrast to reference [Gui03]. In any case, no systematic error is assigned to the higher moments of the beam–charge and the beam–spin asymmetry since nothing is known there about the associated production.

The results of the model calculations in figure 9.2 show that for the $\cos\phi$ moment the ansatz for the $t$–dependence plays a major role as does the D–term. The differences are large and thus even with the statistical uncertainty of this measurement the data can discriminate between the models. Varying the $b$–parameters, on the other hand, results in only small differences. In order to be able to compare the model calculations to the full set of results, the number of models needs to be reduced further. The models shown in the figure can be subdivided in four groups depending

| Model | D–Term | $b_{val}$ | $b_{sea}$ | Ansatz $t$–dependence |
|---|---|---|---|---|
| A | No | 1 | $\infty$ | Regge |
| B | Yes | 1 | $\infty$ | Regge |
| C | No | $\infty$ | $\infty$ | factorized |
| D | Yes | $\infty$ | $\infty$ | factorized |
| A/B | No/Yes | 1 | $\infty$ | Regge |
| C/D | No/Yes | $\infty$ | $\infty$ | factorized |
| E | No/Yes | 1 | 1 | Regge |
| F | No/Yes | 1 | 1 | factorized |

**Table 9.1:** Parameter sets for the GPD models. The predictions from the models A, B, C and D are used for comparison with the beam–charge asymmetry. The beam–spin asymmetry is insensitive to the D–term contribution and thus compared to the models A/B, C/D, E and F.

on the ansatz for the $t$–dependence and on the contribution from the D–term. For a representative sample one model from each of these groups is chosen. The two best suited factorized models are probably those with the predictions in the middle of their respective group, i.e., the two models with and without the D–term and $b_{val}$, $b_{sea} \to \infty$. Concerning the choice of the two Regge models, no obvious preferences can be identified except that the models with $b_{val} = b_{sea} = 1$ are already disfavored by the comparison to the $\sin\phi$ moment, as shown in figure 9.1. The two models with and without the D–term and $b_{val} = 1$, $b_{sea} \to \infty$ are selected. The resulting set of models (A, B, C, D) chosen to be compared to the beam–charge asymmetry in the next section is shown in table 9.1. Note that the predicted results from these models have only a weak dependence on the parameters $b_{val}$ and $b_{sea}$. Since the beam–spin asymmetry is insensitive to the D–term, the models A and B (C and D) yield the same result and thus are combined to a model A/B (C/D) for the comparison (see table 9.1). Note here that model C/D yields very similar results if the Regge ansatz is used instead. For completeness, the beam–spin asymmetry is also compared to the Regge (E) and to the factorized (F) model with $b_{val} = b_{sea} = 1$, although both are disfavored.

## 9.2 Interpretation

In the following the predictions of the chosen models are confronted with the experimental data in all three kinematic variables. Figure 9.3 shows the comparison to the first moments of the beam–charge and the beam–spin asymmetry which are related to the leading twist photon–helicity–conserving DVCS amplitudes (see section 3.3.3). For the $\cos\phi$ moment of the beam–charge asymmetry (left panels) the predictions from the four models differ substantially in all three kinematic variables. Model A fits all data quite well while model B seems almost excluded. The factorized ansätze represented by the models C and D are both possible but less favored. Thus the best agreement is found for the Regge ansatz without a D–term contribution. The physics importance of the D–term has been explained in section 2.1.2. The question whether or not it does indeed contribute is under debate. The preliminary integrated result of this beam–charge asymmetry analysis [Ell02b] was already used for comparisons to model calculations (not shown). The two calculations based on double distributions gave the best agreement with the preliminary data when the D–term was either included [Van02] or not included [Bel02b] in the used model. It is interesting to note that the former calculation is based on the same computer code as is used here. The difference in the conclusion concerning the D–term is due to the fact that the integrated value was given at average kinematics close to the ones in the third $-t_c$ bin, where the Regge models without a D–term contribution and the factorized models with a D–term contribution yield approximately the same value since they have a crossing point (see figure 9.2). The quite different shape between these two groups of models can help to distinguish between them and shows the importance of the extraction of the kinematic dependence. Note that first lattice calculations [Göc03] for the first coefficient $d_1^Q$ of the D–term (see equation 2.32) predict an about four times smaller value than the one used here which was derived [Kiv01a] based on the calculations of GPDs in the chiral quark soliton model [Pet98]. Although the lattice calculation has large systematic uncertainties, it points in the same direction as the finding of this analysis. For completeness it should be mentioned that the preliminary integrated result has been compared to two further model calculations not based on double distributions (not shown) which show either good [Fre03a, Fre03b] or fairly good agreement [Can03].

The $\sin\phi$ moments of the beam–spin asymmetry are displayed in the right panels of figure 9.3. The differences between the models A/B and C/D are small in all kinematic variables. Their shape is similar to the one of the data in all three panels but they slightly undershoot the measured values. It is interesting to note that the largest differences between the results from the model calculations and the data are observed in the first $x_B$ bin and in the first two $Q^2$ bins, which are the only ones with an average $Q^2$ value below 2 GeV$^2$ (see table A.2). The smaller measured asymmetry value with respect to the prediction may thus be due to a partial cancellation of the leading twist asymmetry by higher twist effects not taken into account in the model calculations. A possible candidate is the genuine twist–3 contribution (see section 3.3.3). The interplay between its $\sin 2\phi$ modulation and the lepton propagators can

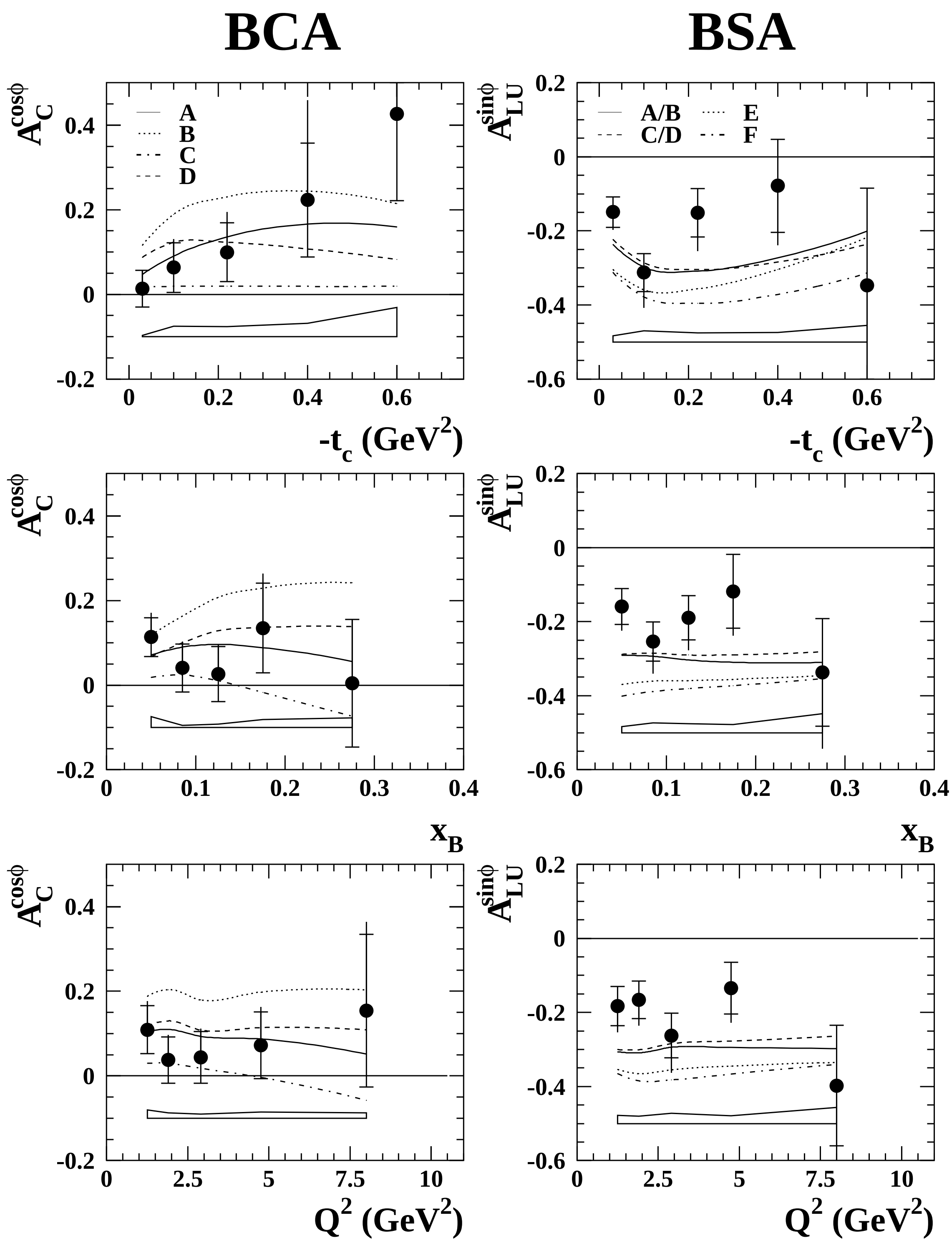


**Figure 9.3:** Model calculations and experimental results for the $\cos\phi$ moment of the beam–charge asymmetry (left panels) and the $\sin\phi$ moment of the beam–spin asymmetry (right panels) as functions of $-t_c$, $x_B$ and $Q^2$. See text for details.

lead to a $\sin\phi$ contribution which is suppressed by $\mathcal{O}(1/Q^2)$ compared to the leading twist $\sin\phi$ contribution. This is not necessarily a negligible effect at $Q^2$ values below 2 GeV$^2$. The question whether or not the genuine twist–3 contribution is at all sizeable is discussed below in the context of the $\sin 2\phi$ moment. In any case, the observed low–$Q^2$ behavior seen here may ultimately be the reason why the already published integrated values of the $\sin\phi$ moments from HERMES and CLAS show a smaller absolute value than most of the model predictions based on the double distribution formalism (see e.g. [Kiv01a, Bel02a, Fre02]) which were calculated at the respective average kinematics only. Another solution is to use different models which have approximately the same good [Fre03a, Fre03b] or not too good [Can03] level of agreement with the published data as in the case of the preliminary value for the first moment of the beam–charge asymmetry. Model E and F are strongly disfavored by the data. Taking into account that increasing $b_{val}$ in both models does essentially not change the prediction, one might conclude that $b_{sea}$ should be always set to a large value as it was done for the models A/B and C/D.

The second moments of the beam–charge and the beam–spin asymmetry are shown in figure 9.4. They are expected to be smaller than the first moments since they are related to the DVCS amplitudes with the virtual photon being longitudinal (see section 3.3.3). Their integrated values (see table 8.1) are indeed both reduced to about 1/3 with respect to their first moments. The comparison of the models to the $\cos 2\phi$ moment of the beam–charge asymmetry in the left panels of figure 9.4 shows that all models predict correspondingly small asymmetries. They all agree with the data. This is good on the one hand, but on the other hand means that there hardly is a possibility to distinguish between models since their differences are small compared to the present statistical error of the data. This holds true for the $\sin 2\phi$ moment of the beam–spin asymmetry as well, where the models A/B, C/D, E and F even predict basically the same value which is about 1/3 of that of the predicted $\sin\phi$ moment. The same ratio is observed between the measured second and first moments as already mentioned above. Consequently the models undershoot the $\sin 2\phi$ data as well, although there is no significant disagreement given the big systematic uncertainty of this particular moment. Considering the statistical error only, three data points are not in agreement with the model calculations, namely the first bin in $x_B$ and the first two bins in $Q^2$, i.e., the same low–$Q^2$ bins as in the case of the $\sin\phi$ moment. Since genuine twist–3 contributions have a $\sin 2\phi$ modulation and are not included in the model, they could account for this effect if they are positive and sizeable at small values of $Q^2$. It is striking that a sizeable positive genuine twist–3 contribution would have the potential to explain at the same time the discrepancies between data and model in the $\sin\phi$ moment. The only available information from theory [Kip02] is that the genuine twist–3 contribution should be

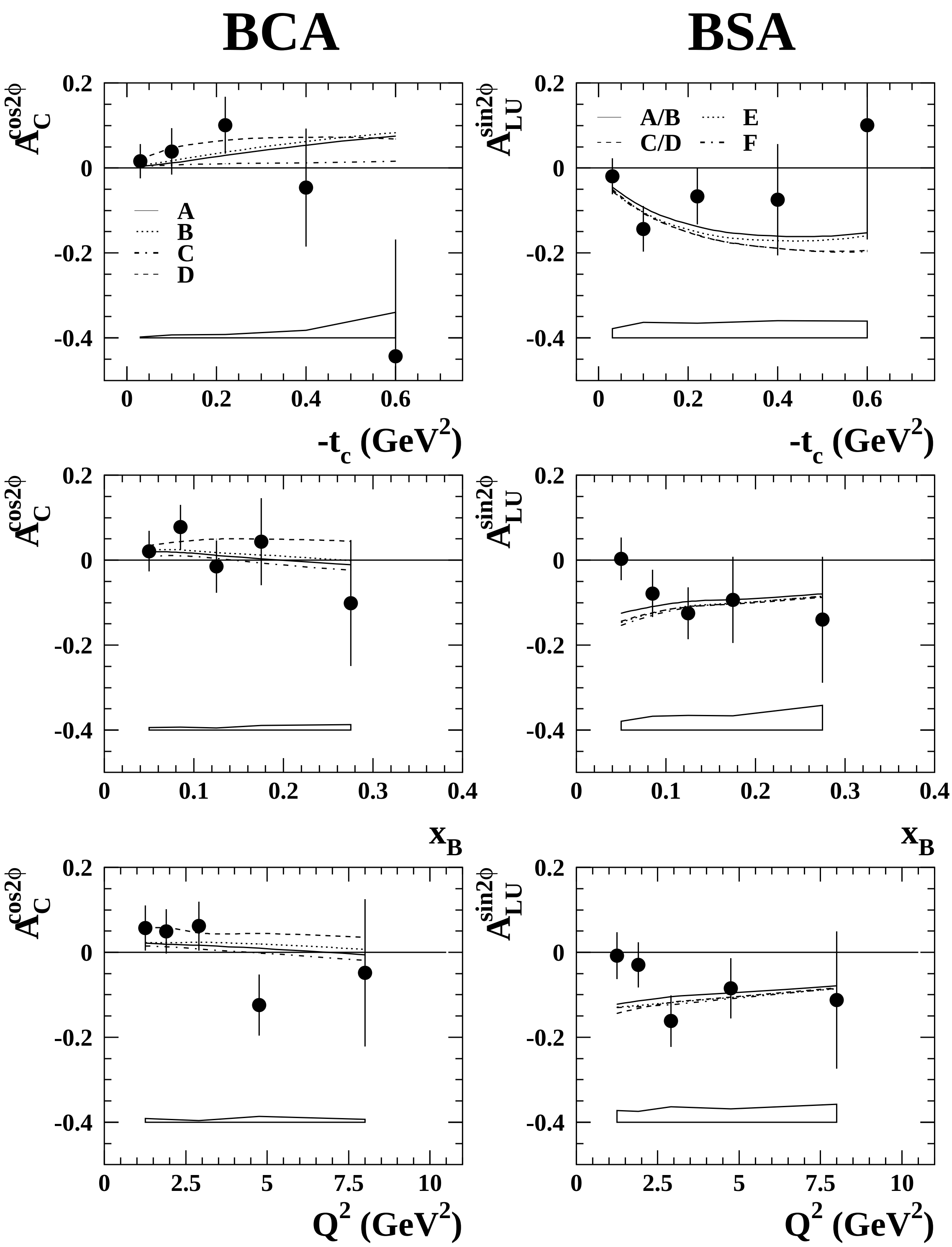


**Figure 9.4:** Model calculations and experimental results for the $\cos 2\phi$ moment of the beam–charge asymmetry (left panels) and the $\sin 2\phi$ moment of the beam–spin asymmetry (right panels) as functions of $-t_c$, $x_B$ and $Q^2$. See text for details.

suppressed compared to the one from the kinematic twist–3.

The third moment of the beam–charge asymmetry is expected to be small since the virtual photon is transverse but has an opposite helicity compared to the real one, i.e., two units of angular momentum have to be compensated (see section 3.3.3). In contrast to the predictions shown in the left panels of figure 9.5, which indeed are close to zero for all kinematic distributions, the measured $\cos 3\phi$ moment shows a sizeable integrated asymmetry (see table 8.1). This might be due to the fact that the $\cos 3\phi$ moment in these calculations arises purely from the interplay between the first two moments of the beam–charge asymmetry and the lepton propagators. Neither the helicity–flip gluon GPDs, i.e., the leading twist–2 contribution to this photon–helicity–flip DVCS amplitude, nor the kinematic twist–4 quark GPDs are included in the model calculations. Since the first two moments of the beam–charge asymmetry are well described by the models, their $\cos 3\phi$ contribution via the interplay with the lepton propagators should also be well described. Thus, the question arises whether the gluons or the quarks may be responsible for the measured asymmetry. Although the helicity–flip gluon GPDs contribute at the leading twist–2 level suppressed by $\alpha_s/\pi$, the fact that the non–zero $\cos 3\phi$ moment is mostly located in the three bins with the lowest average $Q^2$ value, i.e., the first bin in $x_B$ and the first two bins in $Q^2$ (see table A.5), points to a contribution of the kinematic twist–4 quark GPDs.

The $\phi$–independent but charge–dependent constant part of the interference term, related to the same twist–2 GPDs as the first moment of the beam–charge asymmetry but kinematically suppressed (see section 3.3.3), is predicted to be positive but almost negligible by all models and thus agrees with the measurement.

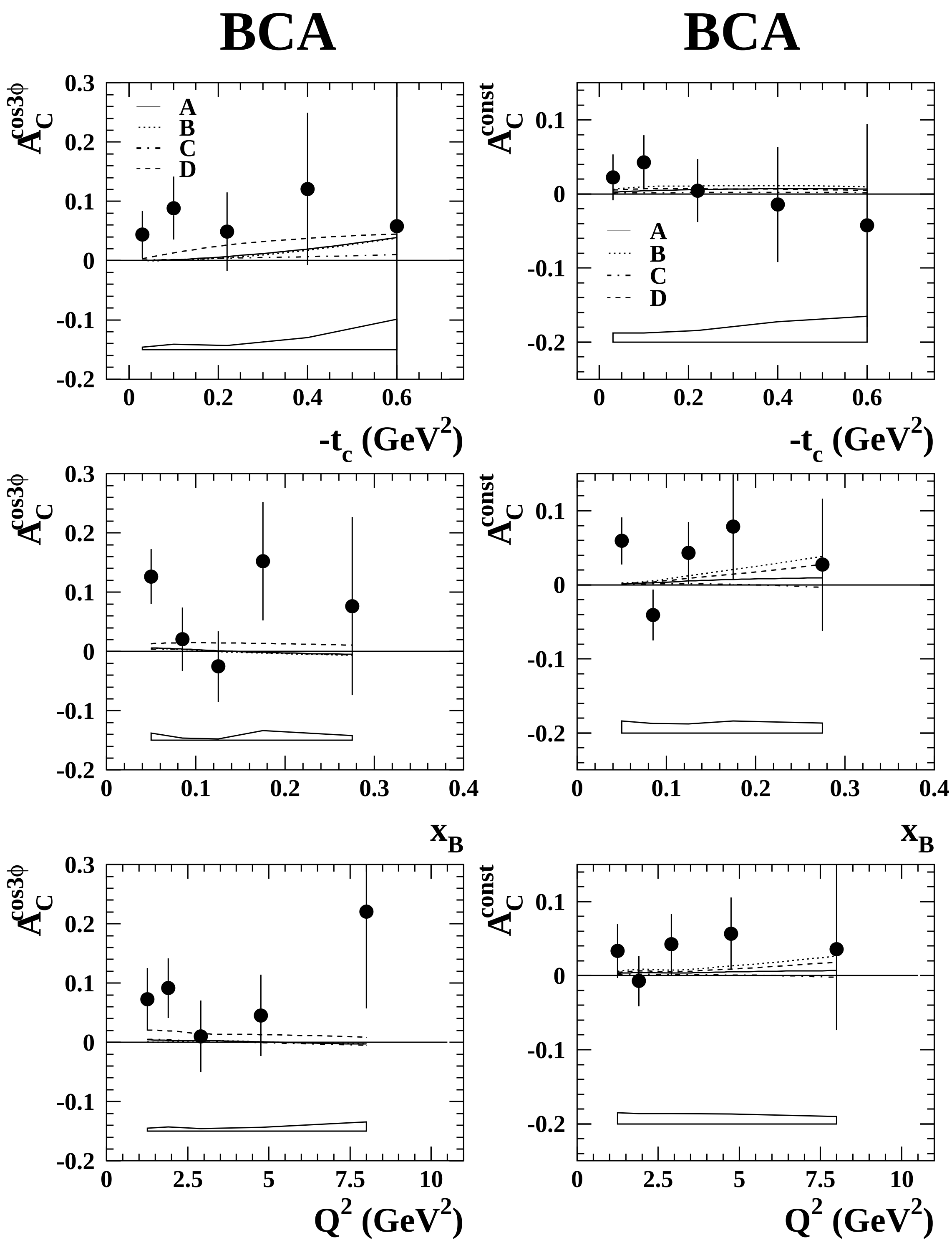


**Figure 9.5:** Model calculations and experimental results for the $\cos 3\phi$ moment of the beam–charge asymmetry (left panels) and its $\phi$–independent part (right panels) as functions of $-t_c$, $x_B$ and $Q^2$. See text for details.

# Chapter 10

# Summary and Outlook

The main goal of the HERMES experiment is the investigation of the spin structure of the nucleon. The contribution of the quark spin to the nucleon spin is known to be smaller than 30%. The remaining part should be made up by unknown contributions from the orbital angular momentum of the quarks and from the total angular momentum of the gluons. The only known way to access the size of those contributions is to determine the total angular momentum of the quarks in the framework of generalized parton distributions. This new theoretical formalism describes the quark–gluon structure of the nucleon including its spin degrees of freedom. It contains the ordinary parton distribution functions and the form factors as limiting cases and moments, respectively. Moreover, it may provide a three–dimensional description of the nucleon structure at the parton level.

Experimental access to generalized parton distributions is possible via hard exclusive reactions. Among these, the theoretically cleanest process appears to be the leptoproduction of real photons, i.e., **D**eeply–**V**irtual **C**ompton **S**cattering (DVCS). The interference term between this process and the Bethe–Heitler process provides direct access to the DVCS amplitudes. Azimuthal asymmetries with respect to the charge and the spin of the incoming lepton are the tool to isolate those parts of the interference term which are directly proportional to the real and the imaginary part of the DVCS amplitudes, respectively.

The extraction of all relevant leading and non–leading moments of these asymmetries as functions of $x_B$, $Q^2$ and $-t_c$ has been performed for the first time. It is described in detail in this thesis. The data set used was collected by the HERMES Collaboration on an unpolarized hydrogen target. The measurement of the beam–charge asymmetry is based on data taken with a (polarized) electron beam in 1998 and a (polarized) positron beam in 2000. It represents the only existing measurement of this quantity. The measurement of the beam–spin asymmetry is based on the data set from 2000 only. The integrated value of the first moment of the latter asymmetry is in agreement with the published results from HERMES and CLAS.

Summarizing the results on the various moments of the beam–charge asymmetry, it was found that the measured values for the first two moments and the constant part agree in sign and size with the model calculations carried out for every kinematic bin. While for the second moment and the constant part the differences in the predictions from different models are small compared to the statistical error of this measurement, the measurement on the first moment is already able to discriminate between models. Especially the ongoing debate concerning the size of the D–term can profit from this data. In this work it is shown that independently of the used values for the parameters $b_{val}$ and $b_{sea}$ the Regge ansätze for the $t$–dependence which include the D–term contribution are almost ruled out, while the same ansätze without the D–term contribution yield the best agreement with the data. The ansätze with a factorized $t$–dependence and with or without the D–term contribution are still possible but less favored. The latter statement is again essentially independent of the values for the $b$–parameters. The finding that an only small contribution from the D–term is favored agrees with the result from a very recent lattice QCD calculation, where the leading coefficient in the D–term was found to be about four times smaller than the one used here which has been calculated based on the chiral quark–soliton model. The third moment of the beam–charge asymmetry is found to be non–zero. This unexpected result might be a first sign for the contribution of either twist–2 helicity–flip gluon GPDs, or kinematic twist–4 quark GPDs, the latter one being possibly more likely.

Summarizing the results on the first two moments of the beam–spin asymmetry, it was found that the measured values agree in sign and approximately in size if $b_{sea} \to \infty$ is chosen for the model calculations. The predictions undershoot both moments in bins with an average $Q^2$ value below 2 GeV$^2$. A possible reason is that the genuine twist–3 contribution is not included in present models. If it has a sizeable positive $\sin 2\phi$ contribution at low $Q^2$ it can be responsible for the disagreement in the first and second moment at the same time. In any case, the observed low–$Q^2$ behavior seen here may ultimately be the reason why the already published integrated values of the $\sin\phi$ moments from HERMES and CLAS show a smaller absolute value than most of the theoretical predictions which were calculated at the respective average kinematics only.

In the near future it will be interesting to see how this data set will be interpreted, especially if genuine twist–3 and kinematic twist–4 GPDs can be included in the present models. The modeling of gluon GPDs probably needs more time. Concerning theoretical progress it is encouraging that first calculations of GPDs on the lattice are available [Häg03, Göc03].

There still exists HERMES data that has not been analyzed yet. The hydrogen data from 1996 and 1997 used for the published integrated result is currently being reprocessed. Including the data into this analysis will decrease the statistical error of the beam–spin asymmetry by about 25%. Since part of the data is taken on a longitudinally polarized hydrogen target, the target–spin asymmetry can be measured which is sensitive to the GPD $\tilde{H}$. Measurements of the DVCS process are not restricted to hydrogen targets. The first measurement of the beam–spin asymmetry on nuclear targets has been performed by the HERMES collaboration on deuterium and neon [Ell02c]. The preliminary values are on the same order as the result on the proton. This result triggered the first theoretical calculations for DVCS on heavier nuclei [Guz03, Kir03, Fre03c], while a few calculations on the deuteron had already been performed beforehand [Ber01, Kir02, Can02].

HERMES continues measurements on transversely polarized and unpolarized hydrogen targets. The former have sensitivity to the GPD $E$. The latter access mainly the GPD $H$ and would greatly benefit from data taken with an electron beam, since the model predictions evaluated in this thesis showed substantial differences for the first moment of the beam–charge asymmetry. The exclusivity of the DVCS process will be improved by the use of a recoil detector currently under construction [HER02]. By this upgrade the associated DVCS processes can be suppressed by an order of magnitude, i.e., the remaining contribution of about 10% associated processes in this analysis decreases to about 1%. The statistics accumulated in one year are expected to allow for the first extraction of the GPD $H^q(\xi, \xi, t)$ [Kor02b]. It was initially assumed that the detection of the recoiling proton will also improve the $t$–resolution. However, when exclusivity is ensured or only assumed, as in this analysis, the resolution is found to be about 0.01 GeV$^2$ and thus better than that of the recoil measurement. A possibly interesting new application for the recoil detector is to actually measure the associated pion production in the DVCS process instead of rejecting these events, although it is under debate whether [Gui03] or not [Che03] the $ep \to eN\pi\gamma$ processes are directly related to the GPDs of the nucleon. Based on numbers given in the technical design report for the recoil detector [HER02] and in this thesis, it is estimated that the data accumulated in one year will contain 1500 events of the reaction $ep \to ep\pi^0\gamma$ where at most one photon from the $\pi^0$ decay remains undetected in the final state. Note that this number is a lower limit and can possibly be increased by up to a factor of 2, since the constraints in this analysis were optimized in order to reduce the associated processes. Thus, the envisaged two years of data taking with the recoil detector would yield sufficient statistics for the first measurement of an associated DVCS process.

Two dedicated DVCS experiments [Sab02] at 6 GeV beam energy are planned in Hall A and Hall B at Jefferson Lab for the years 2003 and 2004, respectively. They aim at the extraction of the beam–spin asymmetry as a function of the kinematic variables as performed in this thesis. However, their kinematic region is located at larger average values of $x_B$ and thus has little overlap with the one from HERMES. In addition, the CLAS collaboration in Hall B is designing a forward calorimeter in order to detect the real photon and thus accomplishing a fully exclusive measurement as well. On a longer time scale the envisaged upgrade of their beam energy to 12 GeV would allow for a larger kinematic coverage. The collider experiments H1 and ZEUS at DESY continue their measurements with longitudinally polarized lepton beams facilitated by the recent installation of spin rotators. This will allow for measurements of the beam–spin asymmetry in addition to measurements of the beam–charge asymmetry and of the cross section [Fav02].

The COMPASS experiment at CERN is carrying out feasibility studies for DVCS measurements and first design studies for a recoil detector [d'Ho02]. Like the experiments at HERA, the COMPASS collaboration has the advantage that lepton (muon) beams of both charges are available. The high beam energies of 100 or 190 GeV would fill the gap between the low–energy fixed–target and the collider experiments. However, in order to eventually map out GPDs a high–luminosity eN facility dedicated to the study of hard exclusive reactions like ELFE [Ans01] or the low energy version of TESLA-N [TES01, Ell01a, Now02] are needed.

# Appendix A

# Tables of Results

| $-t_c$ bin (GeV$^2$) | $\langle -t_c \rangle$ (GeV$^2$) | $\langle x_B \rangle$ | $\langle Q^2 \rangle$ (GeV$^2$) | $A_C^{\cos\phi} \pm$ stat. $\pm$ sys. |
|---|---|---|---|---|
| 0.00 – 0.06 | 0.03 | 0.08 | 2.0 | 0.014 ± 0.043 ± 0.003 |
| 0.06 – 0.14 | 0.09 | 0.10 | 2.5 | 0.063 ± 0.059 ± 0.024 |
| 0.14 – 0.30 | 0.20 | 0.11 | 3.0 | 0.100 ± 0.070 ± 0.023 |
| 0.30 – 0.50 | 0.37 | 0.12 | 3.6 | 0.223 ± 0.135 ± 0.032 |
| 0.50 – 0.70 | 0.57 | 0.12 | 3.9 | 0.426 ± 0.205 ± 0.069 |

| $x_B$ bin | $\langle x_B \rangle$ | $\langle -t_c \rangle$ (GeV$^2$) | $\langle Q^2 \rangle$ (GeV$^2$) | $A_C^{\cos\phi} \pm$ stat. $\pm$ sys. |
|---|---|---|---|---|
| 0.03 – 0.07 | 0.05 | 0.08 | 1.4 | 0.114 ± 0.046 ± 0.025 |
| 0.07 – 0.10 | 0.08 | 0.10 | 2.2 | 0.041 ± 0.057 ± 0.005 |
| 0.10 – 0.15 | 0.12 | 0.12 | 3.1 | 0.026 ± 0.065 ± 0.008 |
| 0.15 – 0.20 | 0.17 | 0.17 | 4.5 | 0.135 ± 0.106 ± 0.019 |
| 0.20 – 0.35 | 0.24 | 0.22 | 6.1 | 0.005 ± 0.151 ± 0.023 |

| $Q^2$ bin (GeV$^2$) | $\langle Q^2 \rangle$ (GeV$^2$) | $\langle -t_c \rangle$ (GeV$^2$) | $\langle x_B \rangle$ | $A_C^{\cos\phi} \pm$ stat. $\pm$ sys. |
|---|---|---|---|---|
| 1.0 – 1.5 | 1.2 | 0.07 | 0.06 | 0.109 ± 0.057 ± 0.020 |
| 1.5 – 2.3 | 1.8 | 0.09 | 0.08 | 0.038 ± 0.055 ± 0.013 |
| 2.3 – 3.5 | 2.8 | 0.12 | 0.10 | 0.044 ± 0.061 ± 0.009 |
| 3.5 – 6.0 | 4.4 | 0.17 | 0.15 | 0.072 ± 0.078 ± 0.015 |
| 6.0 – 10.0 | 7.1 | 0.24 | 0.24 | 0.154 ± 0.180 ± 0.013 |

**Table A.1:** The $\cos\phi$ moment of the beam–charge asymmetry per kinematic bin in $-t_c$, $x_B$ and $Q^2$ at the respective average kinematic values.

| $-t_c$ bin (GeV$^2$) | $\langle -t_c \rangle$ (GeV$^2$) | $\langle x_B \rangle$ | $\langle Q^2 \rangle$ (GeV$^2$) | $A_{LU}^{\sin\phi} \pm$ stat. $\pm$ sys. |
|---|---|---|---|---|
| 0.00 – 0.06 | 0.03 | 0.08 | 2.0 | -0.149 $\pm$ 0.041 $\pm$ 0.016 |
| 0.06 – 0.14 | 0.09 | 0.10 | 2.5 | -0.313 $\pm$ 0.052 $\pm$ 0.030 |
| 0.14 – 0.30 | 0.20 | 0.11 | 3.0 | -0.151 $\pm$ 0.066 $\pm$ 0.025 |
| 0.30 – 0.50 | 0.37 | 0.12 | 3.6 | -0.078 $\pm$ 0.126 $\pm$ 0.025 |
| 0.50 – 0.70 | 0.57 | 0.12 | 3.9 | -0.347 $\pm$ 0.263 $\pm$ 0.045 |

| $x_B$ bin | $\langle x_B \rangle$ | $\langle -t_c \rangle$ (GeV$^2$) | $\langle Q^2 \rangle$ (GeV$^2$) | $A_{LU}^{\sin\phi} \pm$ stat. $\pm$ sys. |
|---|---|---|---|---|
| 0.03 – 0.07 | 0.05 | 0.08 | 1.4 | -0.159 $\pm$ 0.048 $\pm$ 0.016 |
| 0.07 – 0.10 | 0.08 | 0.10 | 2.2 | -0.254 $\pm$ 0.053 $\pm$ 0.027 |
| 0.10 – 0.15 | 0.12 | 0.12 | 3.1 | -0.190 $\pm$ 0.060 $\pm$ 0.024 |
| 0.15 – 0.20 | 0.17 | 0.17 | 4.5 | -0.118 $\pm$ 0.099 $\pm$ 0.022 |
| 0.20 – 0.35 | 0.24 | 0.22 | 6.1 | -0.337 $\pm$ 0.145 $\pm$ 0.052 |

| $Q^2$ bin (GeV$^2$) | $\langle Q^2 \rangle$ (GeV$^2$) | $\langle -t_c \rangle$ (GeV$^2$) | $\langle x_B \rangle$ | $A_{LU}^{\sin\phi} \pm$ stat. $\pm$ sys. |
|---|---|---|---|---|
| 1.0 – 1.5 | 1.2 | 0.07 | 0.06 | -0.183 $\pm$ 0.053 $\pm$ 0.022 |
| 1.5 – 2.3 | 1.8 | 0.09 | 0.08 | -0.166 $\pm$ 0.050 $\pm$ 0.019 |
| 2.3 – 3.5 | 2.8 | 0.12 | 0.10 | -0.262 $\pm$ 0.061 $\pm$ 0.027 |
| 3.5 – 6.0 | 4.4 | 0.17 | 0.15 | -0.135 $\pm$ 0.070 $\pm$ 0.021 |
| 6.0 – 10.0 | 7.1 | 0.24 | 0.24 | -0.398 $\pm$ 0.163 $\pm$ 0.043 |

**Table A.2:** The $\sin\phi$ moment of the beam–spin asymmetry per kinematic bin in $-t_c$, $x_B$ and $Q^2$ at the respective average kinematic values.

| $-t_c$ bin (GeV$^2$) | $\langle -t_c \rangle$ (GeV$^2$) | $\langle x_B \rangle$ | $\langle Q^2 \rangle$ (GeV$^2$) | $A_C^{\cos 2\phi}$ ± stat. ± sys. |
|---|---|---|---|---|
| 0.00 – 0.06 | 0.03 | 0.08 | 2.0 | 0.016 ± 0.040 ± 0.002 |
| 0.06 – 0.14 | 0.09 | 0.10 | 2.5 | 0.039 ± 0.054 ± 0.007 |
| 0.14 – 0.30 | 0.20 | 0.11 | 3.0 | 0.101 ± 0.067 ± 0.008 |
| 0.30 – 0.50 | 0.37 | 0.12 | 3.6 | -0.046 ± 0.139 ± 0.018 |
| 0.50 – 0.70 | 0.57 | 0.12 | 3.9 | -0.443 ± 0.275 ± 0.060 |

| $x_B$ bin | $\langle x_B \rangle$ | $\langle -t_c \rangle$ (GeV$^2$) | $\langle Q^2 \rangle$ (GeV$^2$) | $A_C^{\cos 2\phi}$ ± stat. ± sys. |
|---|---|---|---|---|
| 0.03 – 0.07 | 0.05 | 0.08 | 1.4 | 0.021 ± 0.048 ± 0.006 |
| 0.07 – 0.10 | 0.08 | 0.10 | 2.2 | 0.078 ± 0.053 ± 0.006 |
| 0.10 – 0.15 | 0.12 | 0.12 | 3.1 | -0.015 ± 0.062 ± 0.005 |
| 0.15 – 0.20 | 0.17 | 0.17 | 4.5 | 0.044 ± 0.103 ± 0.011 |
| 0.20 – 0.35 | 0.24 | 0.22 | 6.1 | -0.101 ± 0.149 ± 0.013 |

| $Q^2$ bin (GeV$^2$) | $\langle Q^2 \rangle$ (GeV$^2$) | $\langle -t_c \rangle$ (GeV$^2$) | $\langle x_B \rangle$ | $A_C^{\cos 2\phi}$ ± stat. ± sys. |
|---|---|---|---|---|
| 1.0 – 1.5 | 1.2 | 0.07 | 0.06 | 0.057 ± 0.054 ± 0.009 |
| 1.5 – 2.3 | 1.8 | 0.09 | 0.08 | 0.049 ± 0.052 ± 0.007 |
| 2.3 – 3.5 | 2.8 | 0.12 | 0.10 | 0.062 ± 0.058 ± 0.004 |
| 3.5 – 6.0 | 4.4 | 0.17 | 0.15 | -0.124 ± 0.072 ± 0.014 |
| 6.0 – 10.0 | 7.1 | 0.24 | 0.24 | -0.048 ± 0.174 ± 0.007 |

**Table A.3:** The $\cos 2\phi$ moment of the beam–charge asymmetry per kinematic bin in $-t_c$, $x_B$ and $Q^2$ at the respective average kinematic values.

| $-t_c$ bin (GeV$^2$) | $\langle -t_c \rangle$ (GeV$^2$) | $\langle x_B \rangle$ | $\langle Q^2 \rangle$ (GeV$^2$) | $A_{LU}^{\sin 2\phi} \pm$ stat. $\pm$ sys. |
|---|---|---|---|---|
| 0.00 – 0.06 | 0.03 | 0.08 | 2.0 | -0.019 $\pm$ 0.043 $\pm$ 0.022 |
| 0.06 – 0.14 | 0.09 | 0.10 | 2.5 | -0.144 $\pm$ 0.054 $\pm$ 0.036 |
| 0.14 – 0.30 | 0.20 | 0.11 | 3.0 | -0.067 $\pm$ 0.066 $\pm$ 0.035 |
| 0.30 – 0.50 | 0.37 | 0.12 | 3.6 | -0.075 $\pm$ 0.131 $\pm$ 0.041 |
| 0.50 – 0.70 | 0.57 | 0.12 | 3.9 | 0.101 $\pm$ 0.269 $\pm$ 0.039 |

| $x_B$ bin | $\langle x_B \rangle$ | $\langle -t_c \rangle$ (GeV$^2$) | $\langle Q^2 \rangle$ (GeV$^2$) | $A_{LU}^{\sin 2\phi} \pm$ stat. $\pm$ sys. |
|---|---|---|---|---|
| 0.03 – 0.07 | 0.05 | 0.08 | 1.4 | 0.003 $\pm$ 0.050 $\pm$ 0.021 |
| 0.07 – 0.10 | 0.08 | 0.10 | 2.2 | -0.078 $\pm$ 0.055 $\pm$ 0.032 |
| 0.10 – 0.15 | 0.12 | 0.12 | 3.1 | -0.125 $\pm$ 0.061 $\pm$ 0.035 |
| 0.15 – 0.20 | 0.17 | 0.17 | 4.5 | -0.094 $\pm$ 0.102 $\pm$ 0.034 |
| 0.20 – 0.35 | 0.24 | 0.22 | 6.1 | -0.140 $\pm$ 0.149 $\pm$ 0.058 |

| $Q^2$ bin (GeV$^2$) | $\langle Q^2 \rangle$ (GeV$^2$) | $\langle -t_c \rangle$ (GeV$^2$) | $\langle x_B \rangle$ | $A_{LU}^{\sin 2\phi} \pm$ stat. $\pm$ sys. |
|---|---|---|---|---|
| 1.0 – 1.5 | 1.2 | 0.07 | 0.06 | -0.008 $\pm$ 0.055 $\pm$ 0.028 |
| 1.5 – 2.3 | 1.8 | 0.09 | 0.08 | -0.029 $\pm$ 0.053 $\pm$ 0.025 |
| 2.3 – 3.5 | 2.8 | 0.12 | 0.10 | -0.162 $\pm$ 0.061 $\pm$ 0.036 |
| 3.5 – 6.0 | 4.4 | 0.17 | 0.15 | -0.085 $\pm$ 0.071 $\pm$ 0.032 |
| 6.0 – 10.0 | 7.1 | 0.24 | 0.24 | -0.112 $\pm$ 0.162 $\pm$ 0.042 |

**Table A.4:** The $\sin 2\phi$ moment of the beam–spin asymmetry per kinematic bin in $-t_c$, $x_B$ and $Q^2$ at the respective average kinematic values.

| $-t_c$ bin (GeV$^2$) | $\langle -t_c \rangle$ (GeV$^2$) | $\langle x_B \rangle$ | $\langle Q^2 \rangle$ (GeV$^2$) | $A_C^{\cos 3\phi} \pm$ stat. $\pm$ sys. |
|---|---|---|---|---|
| 0.00 – 0.06 | 0.03 | 0.08 | 2.0 | 0.044 ± 0.040 ± 0.004 |
| 0.06 – 0.14 | 0.09 | 0.10 | 2.5 | 0.089 ± 0.053 ± 0.009 |
| 0.14 – 0.30 | 0.20 | 0.11 | 3.0 | 0.049 ± 0.066 ± 0.006 |
| 0.30 – 0.50 | 0.37 | 0.12 | 3.6 | 0.121 ± 0.129 ± 0.020 |
| 0.50 – 0.70 | 0.57 | 0.12 | 3.9 | 0.058 ± 0.269 ± 0.051 |

| $x_B$ bin | $\langle x_B \rangle$ | $\langle -t_c \rangle$ (GeV$^2$) | $\langle Q^2 \rangle$ (GeV$^2$) | $A_C^{\cos 3\phi} \pm$ stat. $\pm$ sys. |
|---|---|---|---|---|
| 0.03 – 0.07 | 0.05 | 0.08 | 1.4 | 0.126 ± 0.046 ± 0.012 |
| 0.07 – 0.10 | 0.08 | 0.10 | 2.2 | 0.021 ± 0.053 ± 0.004 |
| 0.10 – 0.15 | 0.12 | 0.12 | 3.1 | -0.025 ± 0.059 ± 0.002 |
| 0.15 – 0.20 | 0.17 | 0.17 | 4.5 | 0.152 ± 0.100 ± 0.016 |
| 0.20 – 0.35 | 0.24 | 0.22 | 6.1 | 0.077 ± 0.150 ± 0.008 |

| $Q^2$ bin (GeV$^2$) | $\langle Q^2 \rangle$ (GeV$^2$) | $\langle -t_c \rangle$ (GeV$^2$) | $\langle x_B \rangle$ | $A_C^{\cos 3\phi} \pm$ stat. $\pm$ sys. |
|---|---|---|---|---|
| 1.0 – 1.5 | 1.2 | 0.07 | 0.06 | 0.073 ± 0.053 ± 0.005 |
| 1.5 – 2.3 | 1.8 | 0.09 | 0.08 | 0.091 ± 0.050 ± 0.007 |
| 2.3 – 3.5 | 2.8 | 0.12 | 0.10 | 0.010 ± 0.060 ± 0.004 |
| 3.5 – 6.0 | 4.4 | 0.17 | 0.15 | 0.046 ± 0.069 ± 0.007 |
| 6.0 – 10.0 | 7.1 | 0.24 | 0.24 | 0.220 ± 0.163 ± 0.016 |

**Table A.5:** The $\cos 3\phi$ moment of the beam–charge asymmetry per kinematic bin in $-t_c$, $x_B$ and $Q^2$ at the respective average kinematic values.

| $-t_c$ bin (GeV$^2$) | $\langle -t_c \rangle$ (GeV$^2$) | $\langle x_B \rangle$ | $\langle Q^2 \rangle$ (GeV$^2$) | $A_C^{const} \pm$ stat. $\pm$ sys. |
|---|---|---|---|---|
| 0.00 – 0.06 | 0.03 | 0.08 | 2.0 | 0.034 $\pm$ 0.029 $\pm$ 0.012 |
| 0.06 – 0.14 | 0.09 | 0.10 | 2.5 | 0.044 $\pm$ 0.037 $\pm$ 0.012 |
| 0.14 – 0.30 | 0.20 | 0.11 | 3.0 | 0.004 $\pm$ 0.043 $\pm$ 0.015 |
| 0.30 – 0.50 | 0.37 | 0.12 | 3.6 | -0.014 $\pm$ 0.078 $\pm$ 0.028 |
| 0.50 – 0.70 | 0.57 | 0.12 | 3.9 | -0.043 $\pm$ 0.137 $\pm$ 0.035 |

| $x_B$ bin | $\langle x_B \rangle$ | $\langle -t_c \rangle$ (GeV$^2$) | $\langle Q^2 \rangle$ (GeV$^2$) | $A_C^{const} \pm$ stat. $\pm$ sys. |
|---|---|---|---|---|
| 0.03 – 0.07 | 0.05 | 0.08 | 1.4 | 0.059 $\pm$ 0.032 $\pm$ 0.016 |
| 0.07 – 0.10 | 0.08 | 0.10 | 2.2 | -0.041 $\pm$ 0.035 $\pm$ 0.013 |
| 0.10 – 0.15 | 0.12 | 0.12 | 3.1 | 0.043 $\pm$ 0.042 $\pm$ 0.012 |
| 0.15 – 0.20 | 0.17 | 0.17 | 4.5 | 0.079 $\pm$ 0.070 $\pm$ 0.016 |
| 0.20 – 0.35 | 0.24 | 0.22 | 6.1 | 0.027 $\pm$ 0.089 $\pm$ 0.013 |

| $Q^2$ bin (GeV$^2$) | $\langle Q^2 \rangle$ (GeV$^2$) | $\langle -t_c \rangle$ (GeV$^2$) | $\langle x_B \rangle$ | $A_C^{const} \pm$ stat. $\pm$ sys. |
|---|---|---|---|---|
| 1.0 – 1.5 | 1.2 | 0.07 | 0.06 | 0.033 $\pm$ 0.036 $\pm$ 0.015 |
| 1.5 – 2.3 | 1.8 | 0.09 | 0.08 | -0.007 $\pm$ 0.034 $\pm$ 0.014 |
| 2.3 – 3.5 | 2.8 | 0.12 | 0.10 | 0.042 $\pm$ 0.041 $\pm$ 0.014 |
| 3.5 – 6.0 | 4.4 | 0.17 | 0.15 | 0.057 $\pm$ 0.049 $\pm$ 0.013 |
| 6.0 – 10.0 | 7.1 | 0.24 | 0.24 | 0.036 $\pm$ 0.109 $\pm$ 0.010 |

**Table A.6:** The $\phi$ independent term of the beam–charge asymmetry per kinematic bin in $-t_c$, $x_B$ and $Q^2$ at the respective average kinematic values.

# Appendix B

# Tables of Acceptance Moments

| $t_c$ bin | $A_1$ | $A_2$ | $A_3$ | $A_4$ | $A_5$ | $A_6$ |
|---|---|---|---|---|---|---|
| 1 | -0.179 | -0.022 | 0.005 | -0.002 | 0.002 | 0.001 |
| 2 | -0.226 | 0.012 | -0.001 | 0.012 | -0.008 | 0.007 |
| 3 | -0.324 | 0.036 | -0.008 | -0.009 | 0.008 | 0.003 |
| 4 | -0.440 | 0.050 | 0.011 | -0.017 | 0.010 | -0.001 |
| 5 | -0.490 | -0.002 | 0.049 | 0.020 | -0.006 | -0.052 |
| $x_B$ bin | $A_1$ | $A_2$ | $A_3$ | $A_4$ | $A_5$ | $A_6$ |
| 1 | -0.405 | 0.034 | 0.002 | 0.002 | -0.008 | 0.005 |
| 2 | -0.186 | -0.030 | 0.004 | -0.001 | 0.009 | -0.007 |
| 3 | -0.071 | -0.021 | -0.005 | -0.003 | 0.005 | 0.009 |
| 4 | -0.011 | -0.001 | 0.008 | 0.001 | 0.008 | -0.013 |
| 5 | 0.073 | 0.019 | 0.003 | -0.001 | -0.012 | 0.010 |
| $Q^2$ bin | $A_1$ | $A_2$ | $A_3$ | $A_4$ | $A_5$ | $A_6$ |
| 1 | -0.312 | 0.014 | 0.011 | -0.003 | 0.001 | -0.001 |
| 2 | -0.267 | 0.014 | -0.012 | 0.008 | -0.006 | 0.011 |
| 3 | -0.195 | -0.009 | 0.006 | -0.003 | -0.003 | -0.007 |
| 4 | -0.118 | -0.020 | 0.005 | -0.004 | 0.020 | 0.003 |
| 5 | -0.046 | -0.008 | -0.010 | -0.009 | -0.014 | 0.002 |

**Table B.1:** The first six cosine ($A_1$–$A_6$) moments of the HERMES detector acceptance for each kinematic bin in $-t_c$, $x_B$ and $Q^2$. The bin size and the average kinematics per bin are given in appendix A. The statistical error per acceptance moment is 0.001.

| $t_c$ bin | $B_1$ | $B_2$ | $B_3$ | $B_4$ | $B_5$ | $B_6$ |
|---|---|---|---|---|---|---|
| 1 | 0.012 | -0.007 | 0.007 | -0.013 | -0.010 | 0.003 |
| 2 | -0.013 | 0.004 | 0.004 | -0.011 | 0.002 | -0.019 |
| 3 | 0.008 | 0.003 | -0.002 | -0.011 | 0.012 | -0.005 |
| 4 | 0.012 | 0.001 | 0.005 | -0.016 | 0.015 | -0.006 |
| 5 | 0.007 | 0.004 | -0.020 | 0.013 | 0.018 | -0.060 |
| $x_B$ bin | $B_1$ | $B_2$ | $B_3$ | $B_4$ | $B_5$ | $B_6$ |
| 1 | 0.022 | -0.012 | 0.020 | -0.014 | 0.004 | -0.014 |
| 2 | -0.003 | 0.013 | -0.009 | -0.017 | -0.008 | 0.000 |
| 3 | -0.025 | 0.004 | -0.012 | -0.006 | -0.003 | 0.002 |
| 4 | 0.001 | -0.003 | -0.004 | -0.001 | 0.011 | -0.016 |
| 5 | -0.003 | -0.005 | -0.002 | 0.002 | -0.012 | -0.003 |
| $Q^2$ bin | $B_1$ | $B_2$ | $B_3$ | $B_4$ | $B_5$ | $B_6$ |
| 1 | 0.029 | -0.023 | 0.032 | -0.019 | -0.001 | -0.015 |
| 2 | 0.003 | 0.017 | -0.011 | -0.012 | 0.012 | -0.012 |
| 3 | -0.016 | -0.001 | -0.005 | -0.013 | -0.017 | 0.014 |
| 4 | -0.019 | 0.007 | -0.012 | 0.006 | 0.001 | -0.010 |
| 5 | 0.011 | -0.005 | -0.004 | -0.011 | -0.008 | 0.000 |

**Table B.2:** The first six sine ($B_1$–$B_6$) moments of the HERMES detector acceptance for each kinematic bin in $-t_c$, $x_B$ and $Q^2$. The bin size and the average kinematics per bin are given in appendix A. The statistical error per acceptance moment is 0.001.

# Bibliography


[Ack98] K. Ackerstaff et al., *The HERMES Spectrometer*, Nucl. Instr. and Meth. **A417** (1998) 230

[Adl01] C. Adloff et al., *Measurement of deeply virtual Compton scattering at HERA*, Phys. Lett. **B517** (2001) 47

[Air01] A. Airapetian et al., *Measurement of the Beam–Spin Azimuthal Asymmetry Associated with Deeply–Virtual Compton Scattering*, Phys. Rev. Lett. **87** (2001) 182001

[Air03a] A. Airapetian et al., *Flavor Decomposition of the Sea Quark Helicity Distributions in the Nucleon from Semi–inclusive Deep–inelastic Scattering*, submitted to Phys. Rev. Lett., hep–ex/0307064

[Air03b] A. Airapetian et al., *Quark helicity distributions in the nucleon for up–, down–, and strange–quarks from semi–inclusive deep–inelastic scattering*, in preparation

[Ako02] N. Akopov et al., *The HERMES Dual-Radiator Ring Imaging Čerenkov Detector*, Nucl. Instr. and Meth. **A479** (2002) 511

[Aku99] I. Akushevich, H. Böttcher and D. Ryckbosch, *RADGEN 1.0: Monte Carlo Generator for Radiative Events in DIS on Polarized and Unpolarized Targets*, hep–ph/9906408

[And83] B. Andersson, G. Gustafson, G. Ingelman and T. Sjöstrand, *Parton Fragmentation and String Dynamics*, Phys. Rept. **97** (1983) 31

[Ans01] M. Anselmino et al, *ELFE: The Electron Laboratory for Europe*, TESLA Technical Design Report, DESY 2001–011, Part VI, Chapter 4, ed.s E. DeSanctis, J.–M. Laget and K. Rith

[Ash88] J. Ashman et al., *A measurement of the spin asymmetry and determination of the structure function $g_1$ in deep inelastic muon–proton scattering*, Phys. Lett. **B206** (1988) 364

[Bar93] D. P. Barber et al., *The HERA polarimeter and the first observation of electron spin polarization at HERA*, Nucl. Instr. and Meth. **A329** (1993) 79

[Bar94] D. P. Barber et al., *High spin polarization at the HERA electron storage ring*, Nucl. Instr. and Meth. **A338** (1994) 166

[Bau02] C. Baumgarten et al., *An atomic beam polarimeter to measure the nuclear polarization in the HERMES gaseous polarized hydrogen and deuterium target*, Nucl. Instr. and Meth. **A482** (2002) 606

[Bau03a] C. Baumgarten et al., *The Storage Cell of the Polarized H/D Internal Gas Target of the HERMES Experiment at HERA*, Nucl. Instr. and Meth. **A496** (2003) 277

[Bau03b] C. Baumgarten et al., *A Gas Analyzer for the Internal Polarized Target of the HERMES Experiment*, Nucl. Instr. and Meth. **A508** (2003) 265

[Bec02] M. Beckmann et al., *The Longitudinal Polarimeter at HERA*, Nucl. Instr. and Meth. **A479** (2002) 334

[Bel98] A.V. Belitsky and D. Müller, *Predictions from conformal algebra for the deeply virtual Compton scattering*, Phys. Lett **B417** (1998) 129

[Bel99] A.V. Belitsky and D. Müller, *Broken conformal invariance and spectrum of anomalous dimensions in QCD*, Nucl. Phys. **B537** (1999) 397

[Bel00a] A.V. Belitsky, A. Freund and D. Müller, *Evolution kernels of skewed parton distributions: Method and two–loop results*, Nucl. Phys. **B574** (2000) 347

[Bel00b] A.V. Belitsky and D. Müller, *Off–forward gluonometry*, Phys. Lett **B486** (2000) 369

[Bel02a] A.V. Belitsky, D. Müller and A. Kirchner, *Theory of deeply virtual Compton scattering on the nucleon*, Nucl. Phys. **B629** (2002) 323

[Bel02b] A.V. Belitsky and D. Müller, *Nucleon hologram with exclusive leptoproduction*, Nucl. Phys. **A711** (2002) 118

[Ben01] T. Benisch et al., *The luminosity monitor of the HERMES experiment at DESY*, Nucl. Instr. and Meth. **A471** (2001) 314

[Ber01] E.R. Berger et al., *Generalized parton distributions in the deuteron*, Phys. Rev. Lett. **87** (2001) 142302

[Ber02] E.R. Berger, M. Diehl and B. Pire, *Timelike Compton scattering: exclusive photoproduction of lepton pairs*, Eur. Phys. J. **C23** (2002) 675

[Bes79] D. Besset et al., *A Set of efficient Estimators for Polarization Measurements*, Nucl. Instr. and Meth. **166** (1979) 515

[Blü99] J. Blümlein, B. Geyer and D. Robaschik, *The Virtual Compton Amplitude in the Generalized Bjorken Region: Twist–2 Contributions*, Nucl. Phys. **B560** (1999) 283

[Bra76] F.W. Brasse et al., *Parametrization of the $q^2$ Dependence of $\gamma_v p$ Total Cross Sections in the Resonance Region*, Nucl. Phys. **B110** (1976) 413

[Bro72] S.J. Brodsky, F.E. Close and J.F. Gunion, *Phenomenology of Photon Processes, Vector Dominance, and Crucial Tests for Parton Models*, Phys. Rev. **D6** (1972) 177

[Buo86] J. Buon and K. Steffen, *HERA variable–energy "Mini" Spin Rotator and head–on ep collision scheme with choice of electron helicity*, Nucl. Instr. and Meth. **A245** (1986) 248

[Bur00] M. Burkardt, *Impact parameter dependent parton distributions and off–forward parton distributions for $\zeta \to 0$*, Phys. Rev. **D62** (2000) 071503; Erratum–ibid. **D 66** (2002) 119903

[Bur03] M. Burkardt, *Impact parameter space interpretation for generalized parton distributions*, Int. J. Mod. Phys. **A18** (2003) 173

[Can02] F. Cano and B. Pire, *Deeply Virtual Compton Scattering on the Deuteron*, Nucl. Phys. **A711** (2002) 133

[Can03] F. Cano and J.–M. Laget, *Real and Virtual Compton Scattering in a Regge Approach*, Phys. Lett **B551** (2003) 317; Erratum–ibid. **B571** (2003) 250

[Car99] P.W. Carter, *The HERMES Experiment: I. Analyzing Powers in Pion Electroproduction, II. The Aerogel Radiator of the HERMES RICH*, PhD thesis, California Institute of Technology (1999)

[Cer93] CERN-Computing and Networks Division, *GEANT: Detector Description and Simulation Tool*, CERN Program Library Long Writeup W5013

[Che03] J–W. Chen and M.J. Savage, *Soft Pion Emission in DVCS*, nucl–th/0308033

[Col97] J.C. Collins, L. Frankfurt and M. Strikman, *Factorization of hard exclusive electroproduction of mesons in QCD*, Phys. Rev. **D56** (1997) 2982

[Col99] J.C. Collins and A. Freund, *Proof of factorization for deeply virtual Compton scattering in QCD*, Phys. Rev. **D59** (1999) 074009

[Com23] A.H. Compton, *A Quantum Theory of the Scattering of X–Ray by light Elements*, Phys. Rev. **21** (1923) 483;
*The Spectrum of Scattered X–Rays*, Phys. Rev. **22** (1923) 409

[DeN01] L. De Nardo, *Trigger Efficiencies for 98 and 99 Data*, HERMES Internal Report, 01-005 (2001)

[d'Ho02] N. d'Hose et al., *Feasibility Study of Deeply Virtual Compton Scattering using COMPASS*, Nucl. Phys. **A711** (2002) 160

[Die97] M. Diehl, T. Gousset, B. Pire and J.P. Ralston, *Testing the handbag contribution to exclusive virtual Compton scattering*, Phys. Lett. **B411** (1997) 193

[Die01] M. Diehl, *Generalized parton distributions with helicity flip*, Eur. Phys. J. **C19** (2001) 485

[Die02] M. Diehl, *Generalized parton distributions in impact parameter space*, Eur. Phys. J. **C25** (2002) 223

[Dit88] F.M. Dittes et al., *The Altarelli–Parisi Kernel as Asymptotic Limit of an extended Brodsky–Lepage Kernel*, Phys. Lett. **B209** (1988) 325

[Don01] A. Donnachie and H.G. Dosch, *Diffractive Exclusive Photon Production in Deep Inelastic Scattering*, Phys. Lett. **B502** (2001) 74

[Ell01a] F. Ellinghaus for the TESLA–N Study Group, *Polarized electron–nucleon scattering at TESLA*, Czech. J. Phys. **51** (2001) Suppl. A, A65

[Ell01b] F. Ellinghaus, *Do we understand the energy calibration of photons?* Analysis Meeting Minutes, November 15, 2001

[Ell02a] F. Ellinghaus, D. Gaskell and R. Shanidze, *Beam–Charge and Beam–Spin Asymmetries from Deeply–Virtual Compton Scattering*, HERMES Release Report, February 2002

[Ell02b] F. Ellinghaus for the HERMES Collaboration, *Beam–Charge Asymmetry associated with DVCS at HERMES*, Nucl. Phys. **A711** (2002) 171

[Ell02c] F. Ellinghaus for the HERMES Collaboration, *Deeply–Virtual Compton Scattering on Deuterium and Neon at HERMES*, Proc. of the 15th International Spin Physics Symposium "Spin 2002", eds. Y.I. Makdisi, A.U. Luccio and W.W. MacKay, Upton, New York, AIP Conf. Proc. **675** (2002) 303, also in F. Ellinghaus, R. Shanidze and J. Volmer for the HERMES Collaboration, hep–ex/0212019

[Els02] U. Elschenbroich, *Analysis of Luminosity Data for Different Years*, HERMES Internal Report, 02-013 (2002)

[Els03] U. Elschenbroich, *Single Spin Azimuthal Asymmetry in Exclusive Electroproduction of $\rho^0$ Mesons*, HERMES Release Report, February 2003

[Ely01] J. Ely, *HERMES Calorimeter Position Reconstruction Study*, HERMES Internal Report, 01-056 (2001)

[Ely02a] J. Ely, *Measurement of the single spin azimuthal asymmetry in the predominantly exclusive electroproduction of photons from the proton*, PhD thesis, University of Colorado (2002)

[Ely02b] J. Ely, *DVCS Single–Spin Asymmetry: Kinematic dependences*, HERMES Release Report, February 2002

[Fav02] L. Favart, *Deeply Virtual Compton Scattering at H1 and ZEUS*, Nucl. Phys. **A711** (2002) 165

[Fra98] L.L. Frankfurt, A. Freund and M. Strikman, *Diffractive Exclusive Photon Production in DIS at HERA*, Phys. Rev. **D58** (1998) 114001; Erratum–ibid. Phys. Rev. **D59** (1999) 119901

[Fre02] A. Freund and M. McDermott, *A detailed next–to–leading order QCD analysis of deeply virtual Compton scattering observables*, Eur. Phys. J. **C23** (2002) 651

[Fre03a] A. Freund, M. McDermott and M. Strikman, *Modeling generalized parton distributions to describe deeply virtual Compton scattering data*, Phys. Rev. **D67** (2003) 036001

[Fre03b] A. Freund, *A detailed QCD analysis of twist–3 effects in DVCS observables*, hep–ph/0306012

[Fre03c] A. Freund and M. Strikman *DVCS on nuclei: Observability and Consequences*, hep–ph/0309065

[Göc03] M. Göckeler et al., *Generalized Parton Distributions from Lattice QCD*, hep-ph/0304249

[Goe01] K. Goeke, M.V. Polyakov and M. Vanderhaeghen, *Hard Exclusive Reactions and the Structure of Hadrons* Prog. Part. Nucl. Phys. **47** (2001) 401

[GPD01] Website of the 267. WE-HERAEUS–Seminar on Generalized Parton Distributions, Nov 19 –21, 2001, Scientific organizers: P. Kroll and A. Schäfer, http://www.theorie.physik.uni-wuppertal.de/∼wwwkroll/badhonnef/

[Gui03] P.A.M. Guichon, L. Mossé and M. Vanderhaeghen, *Pion production in deeply virtual Compton scattering*, hep–ph/0305231

[Guz03] V. Guzey and M. Strikman, *DVCS on spinless nuclear targets in impulse approximation*, Phys. Rev. **C68** (2003) 015204

[Hae85] W. Haeberli, *Nuclear Physics with Stored Cooled Beams*, New York, AIP Conf. Proc 128 (1985) 251

[Häg03] Ph. Hägler et al., *Moments of Nucleon Generalized Parton Distributions in Lattice QCD*, hep-lat/0304018

[HER02] HERMES Collaboration, *The HERMES Recoil Detector*, DESY PRC 02–01, 2002

[Hil03] A. Hillenbrand, *Tuning of the LUND Model for Fragmentation Functions and Purities*, to be published in the Proceedings of the 11th International Workshop on Deep–Inelastic Scattering, St. Petersburg, Russia, April 2003

[Hof55] R. Hofstadter and R.W. McAllister, *Electron Scattering from the Proton*, Phys. Rev. **98** (1955) 217

[Hoo98] P. Hoodbhoy and X. Ji, *Helicity–Flip Off–Forward Parton Distributions of the Nucleon*, Phys. Rev. **D58** (1998) 054006

[Ing97] G. Ingelmann, A. Edin and J. Rathsman, *LEPTO 6.5 – A Monte Carlo Generator for Deep Inelastic Lepton–Nucleon Scattering*, Comput. Phys. Commun. **101** (1997) 108

[Jaf96] R.L. Jaffe, *Spin, Twist and Hadron Structure in Deep Inelastic Processes*, hep–ph/9602236

[Ji97a] X. Ji, *Gauge Invariant Decomposition of Nucleon Spin*, Phys. Rev. Lett. **78** (1997) 610

[Ji97b] X. Ji, *Deeply virtual Compton scattering*, Phys. Rev. **D55** (1997) 7114

[Ji97c] X. Ji, W. Melnitchouk and X. Song, *Study of off–forward parton distributions*, Phys. Rev. **D56** (1997) 5511

[Ji98a] X. Ji and J. Osborne, *One–Loop Corrections and All Order Factorization In Deeply Virtual Compton Scattering*, Phys. Rev. **D58** (1998) 094018

[Ji98b] X. Ji, *Off–forward parton distributions*, J. Phys. **G24** (1998) 1181

[Kip02] D.V. Kiptily and M.V. Polyakov, *Genuine twist–3 contributions to the generalized parton distributions from instantons*, hep–ph/0212372

[Kir02] A. Kirchner and D. Müller, *Predictions for deeply virtual Compton scattering on a spin–one target*, hep–ph/0202279

[Kir03] A. Kirchner and D. Müller, *Deeply virtual Compton scattering off nuclei*, hep–ph/0302007

[Kiv01a] N. Kivel, M.V. Polyakov and M. Vanderhaeghen, *Deeply virtual Compton scattering on the nucleon: Study of the twist–3 effects*, Phys. Rev. **D63** (2001) 114014

[Kiv01b] N. Kivel and L. Mankiewicz, *Twist–4 photon helicity–flip amplitude in DVCS on a nucleon in the Wandzura-Wilczek approximation*, Eur. Phys. J. **C21** (2001) 621

[Kor02a] V.A. Korotkov and W.-D. Nowak, *Future measurements of deeply virtual Compton scattering*, Eur. Phys. J. **C23** (2002) 455

[Kor02b] V.A. Korotkov and W.-D. Nowak, *Extraction of the Generalized Parton Distribution $H(\xi,\xi,t)$ from DVCS*, Nucl. Phys. **A711** (2002) 175

[Kro96] P. Kroll, M. Schürmann and P.A.M. Guichon, *Virtual Compton Scattering off Protons at Moderately Large Momentum Transfer*, Nucl. Phys. **A598** (1996) 435

[Man98a] L. Mankiewicz, G. Piller and T. Weigl, *Hard exclusive meson production and nonforward parton distributions*, Eur. Phys. J. **C5** (1998) 119

[Man98b] L. Mankiewicz et al., *NLO corrections to deeply–virtual Compton scattering*, Phys. Lett **B425** (1998) 186

[Mar98] A.D. Martin, R.G. Roberts, W.G. Stirling and R.S. Thorne *Parton distributions: a new global analysis*, Eur. Phys. J. **C4** (1998) 463

[Mo69] L.W. Mo and Y.S. Tsai, *Radiative Corrections to Elastic and Inelastic ep and $\mu p$ Scattering*, Rev. Mod. Phys. **41** (1969) 205

[Mül94] D. Müller et al., *Wave Functions, Evolution Equations and Evolution Kernels from Light–Ray Operators of QCD*, Fortschr. Phys. **42** (1994) 101

[Nas03] A. Nass et al., *The HERMES Polarized Atomic Beam Source*, Nucl. Instr. and Meth. **A505** (2003) 633

[Now02] W.-D. Nowak, *European Perspectives for Electron–Nucleon Scattering at the Luminosity Frontier*, Nucl. Phys. Proc. Suppl. **105** (2002) 171

[Pet98] V.Y. Petrov et al., *Off–forward quark distributions of the nucleon in the large $N_C$ limit*, Phys. Rev. **D57** (1998) 4325

[Pol99] M.V. Polyakov and C. Weiss, *Skewed and double distributions in the pion and the nucleon*, Phys. Rev. **D60** (1999) 114017

[Pol02] M.V. Polyakov and A.G. Shuvaev, *On "dual" parametrizations of generalized parton distributions*, hep–ph/0207153

[Pol03] M.V. Polyakov, *Generalized parton distributions and strong forces inside nucleons and nuclei*, Phys. Lett. **B555** (2003) 57

[Rad96a] A.V. Radyushkin, *Scaling Limit of Deeply Virtual Compton Scattering*, Phys. Lett. **B380** (1996) 417

[Rad96b] A.V. Radyushkin, *Asymmetric Gluon Distributions and Hard Diffractive Electroproduction*, Phys. Lett. **B385** (1996) 333

[Rad97] A.V. Radyushkin, *Nonforward Parton Distributions*, Phys. Rev. **D56** (1997) 5524

[Rad98] A.V. Radyushkin, *Nonforward Parton Densities and Soft Mechanism for Form Factors and Wide–Angle Compton Scattering in QCD*, Phys. Rev. **D58** (1998) 114008

[Rad99a] A.V. Radyushkin, *Double distributions and evolution equations*, Phys. Rev. **D59** (1999) 014030

[Rad99b] A.V. Radyushkin, *Symmetries and structure of skewed and double distributions*, Phys. Lett. **B449** (1999) 81

[Rad01] A.V. Radyushkin, *Generalized parton distributions, in: At the frontier of particle physics*, ed. M. Shifman, World Scientific, Singapore (2001) vol. 2, 1037, hep–ph/0101225

[Ral02] J.P. Ralston and B. Pire, *Femto–Photography of Protons to Nuclei with Deeply Virtual Compton Scattering*, Phys. Rev. **D66** (2002) 111501

[Sab02] F. Sabatié, *The Generalized Parton Distributions Program at Jefferson Lab*, hep–ex/0207016

[Sau01] P.R.B. Saull for the H1 and ZEUS Collaborations, *Deeply virtual Compton scattering*, Proceedings of the International Europhysics Conference on High–Energy Physics (HEP2001), Budapest, Hungary, July 2001

[Sjö94] T. Sjöstrand, *High–Energy Physics Event Generation with PYTHIA 5.7 and JETSET 7.4*, Comput. Phys. Commun. **82** (1994) 74

[Sok64] A. A. Sokolov and I. M. Ternov, *On polarization and spin effects in the theory of synchrotron radiation*, Sov. Phys. Doklady **8** (1964) 1203

[Ste01] S. Stepanyan et al., *Observation of Exclusive Deeply Virtual Compton Scattering in Polarized Electron Beam Asymmetry Measurements*, Phys. Rev. Lett. **87** (2001) 182002

[TES01] TESLA–N Study Group, *TESLA–N: Electron Scattering with Polarized Targets at TESLA*, TESLA Technical Design Report, DESY 2001–011, Part VI, Chapter 3, ed.s R. Kaiser and W.–D. Nowak; also in: M. Anselmino et al., hep–ph/0011299

[Van99] M. Vanderhaeghen, P.A.M. Guichon and M. Guidal, *Deeply virtual electroproduction of photons and mesons on the nucleon: Leading order amplitudes and power corrections*, Phys. Rev. **D60** (1999) 094017

[Van00] M. Vanderhaeghen et al., *QED radiative corrections to virtual Compton scattering*, Phys. Rev. **C62** (2000) 025501

[Van01] M. Vanderhaeghen, P.A.M. Guichon and M. Guidal, Computer code for the calculation of DVCS and BH processes in the reaction $e\,p \to e\,p\,\gamma$, Private Communication, 2001

[Van02] M. Vanderhaeghen, *Overview on All Reactions Linked to GPDs*, Nucl. Phys. **A711** (2002) 109

[Van03] M. Vanderhaeghen, P.A.M. Guichon and L. Mossé, Computer Code for the calculation of DVCS and BH processes in the reaction $e\,p \to e\,\pi\,N\,\gamma$, Private Communication, 2003

[Wan96] W. Wander, *Reconstruction of High Energy Scattering Events in the HERMES Experiment*, PhD thesis, Friedrich–Alexander Universität Erlangen–Nürnberg, Germany (1996)

# Acknowledgements

First and foremost, I would like to thank my advisor Dr. Wolf–Dieter Nowak for his valuable support. He gave me the opportunity to work on the HERMES experiment and managed to provide me with the ideal mixture of guidance and freedom to follow my own intuition. I would also like to thank Prof. Thomas Lohse for taking over the role as my official advisor at the Humboldt–University in Berlin.

I owe thanks to Matthias Hartig for his proposal to visit the HERMES experiment and to Andy Miller, who, by showing me the FQS, got me right away interested in working with him on this exciting piece of hardware. Without these two, I probably would have never joined the HERMES Collaboration and experienced the friendly working atmosphere.

Concerning the DVCS analysis I want to express my gratitude to Moskov Amarian for all the discussions we had and for his essential suggestion to give the beam–charge asymmetry a try. Thanks to James Ely who helped me to get started in the early phase of the DVCS analysis and to all other DVCS enthusiasts, especially to Dave Gaskell, Slava Korotkov, Bernhard Krauss, Rezo Shanidze and in particular to Jochen Volmer. Outside the DVCS group I benefited from discussions with Elke Aschenauer, Uta Stößlein and my office mate Patricia Liebing. Outside the HERMES Collaboration I am grateful to the theoreticians, especially to Markus Diehl and Andreas Freund, for many enlightening discussions and to Marc Vanderhaeghen for handing out the DVCS codes. Finally, I am indebted to Wolf–Dieter Nowak and Jochen Volmer for proofreading the thesis and to Ed Kinney for providing the analysis with the time it needed to mature.

I would like to thank all members of the HERMES-Zeuthen group who made work and life in Zeuthen/Berlin and Hamburg so enjoyable, especially Moskov Amarian, Elke Aschenauer, Helmut Böttcher, Markus Ehrenfried, Yvo Gärber, Peter Jung, Ralf Kaiser, Patricia Liebing, Katerina Lipka, Falk Meissner, Wolf–Dieter Nowak, Gunnar Schnell, Jim Stewart, Uta Stößlein and Jochen Volmer.

Greetings to all the other people I enjoyed the time in Hamburg with, be it Offsite, soccer, squash or even at work: Achim, Andreas, Antje, Beni, Bino, Caro, Delia, Dirk, Eduard, Ines, Jürgen, Lara, Larry, Maf, Marc, Manuella, Martin, Matthias, Maurice, Naomi, Phil, Philipp, Ralf, Soerne, Uli ... to be continued ...

I would like to thank my parents for their unconditional support and understanding. Julia, a trouble shared is a trouble halved, thanks for all the late–night calls.

**Erklärung**

Hiermit erkläre ich, die Dissertation selbständig und ohne unerlaubte Hilfe angefertigt zu haben. Ich habe mich anderwärts nicht um einen Doktorgrad beworben und besitze einen entsprechenden Doktorgrad nicht. Ich erkläre die Kenntnisnahme der dem Verfahren zugrunde liegenden Promotionsordnung der Mathematisch–Naturwissenschaftlichen Fakultät I der Humboldt–Universität zu Berlin.

Hamburg, den 7. November 2003 ......................................

# Lebenslauf

**Persönliche Daten:**

| | |
|---|---|
| Name | Frank Ellinghaus |
| Geburtsdatum | 15. Juni 1973 |
| Geburtsort | Borghorst |
| Staatsangehörigkeit | deutsch |

| | |
|---|---|
| Aug. 1979 – Juli 1983 | St. Johannes Grundschule Altenberge |
| Aug. 1983 – Juni 1992 | Gymnasium Paulinum Münster |
| Juli 1992 – Juni 1993 | Grundwehrdienst |
| Okt. 1993 – Okt. 1997 | Studium der Physik an der Westfälischen Wilhelms–Universität Münster |
| Nov. 1997 – Sep. 1999 | Dimplomarbeit am Institut für Kernphysik der Westfälischen Wilhelms–Universität Münster, Abschluß: Diplom |
| Jan. 2000 – Juli 2003 | Wissenschaftliche Hilfskraft am Forschungsinstitut DESY Zeuthen |
| seit Aug. 2003 | University of Colorado, USA |

Hamburg, den 7. November 2003 ......................................

# Publikationen


1. **A new wire chamber front–end system, based on the ASD–8 B chip**,
B.A.M. Krüsemann et al., Nucl. Instr. and Meth. **A431** (1999) 459

2. **A DSP–based readout and online processing system for a new focal–plane polarimeter at AGOR**,
M. Hagemann et al., Nucl. Instr. and Meth. **A437** (1999) 236

3. **Polarized electron–nucleon scattering at TESLA**,
F. Ellinghaus for the TESLA–N Study Group, Czech. J. Phys. **51** (2001) Suppl. A, A65

4. **TESLA–N: Future Polarized Electron–Nucleon Scattering at DESY**,
F. Ellinghaus for the TESLA–N Study Group, Proc. of the 16th Lake Louise Winter Institute "Fundamental Interactions", eds. A. Astbury, B.A. Campbell, F.C. Khanna and M.G. Vincter, Lake Louise, Canada, Feb. 2001, World Scientific, p. 192

5. **Single–spin azimuthal asymmetries in electroproduction of neutral pions in semi–inclusive deep–inelastic scattering**,
A. Airapetian et al., Phys. Rev. **D64** (2001) 097101

6. **Measurement of the Beam–Spin Azimuthal Asymmetry Associated with Deeply–Virtual Compton Scattering**,
A. Airapetian et al., Phys. Rev. Lett. **87** (2001) 182001

7. **Measuring the (d,$^2$He) reaction with the focal–plane detection system of the BBS magnetic spectrometer at AGOR**,
S. Rakers et al., Nucl. Instr. and Meth. **A481** (2002) 253

8. **Beam–Charge Asymmetry associated with DVCS at HERMES**,
F. Ellinghaus for the HERMES Collaboration, Nucl. Phys. **A711** (2002) 171

9. **Single–spin azimuthal asymmetries in exclusive electroproduction of $\pi^+$ mesons**,
A. Airapetian et al., Phys. Lett. **B535** (2002) 85

10. **Deeply–Virtual Compton Scattering on Deuterium and Neon at HERMES**,
F. Ellinghaus for the HERMES Collaboration, Proc. of the 15th International Spin Physics Symposium "Spin 2002", eds. Y.I. Makdisi, A.U. Luccio and W.W. MacKay, Upton, New York, AIP Conf. Proc. **675** (2002) 303,
also in F. Ellinghaus et al. for the HERMES Collaboration, hep–ex/0212019

11. **$Q^2$ Dependence of Nuclear Transparency for Exclusive $\rho^0$ Production**,
A. Airapetian et al., Phys. Rev. Lett. **90** (2003) 052501

12. **The $Q^2$–dependence of the generalised Gerasimov–Drell–Hearn integral for the deuteron, proton and neutron**,
A. Airapetian et al., Eur. Phys. Jour. **C26** (2003) 527

13. **On the determination of polarization observables in proton–induced reactions using large–acceptance magnetic spectrometers**,
V.M. Hannen et al., Nucl. Instr. and Meth. **A500** (2003) 68

14. **Evidence for Quark–Hadron Duality in the Proton Spin Asymmetry $A_1$**,
A. Airapetian et al., Phys. Rev. Lett. **90** (2003) 092002

15. **Erratum to: "Nuclear effects on $R = \sigma_L/\sigma_T$ in deep–inelastic scattering", [K. Ackerstaff et al., Phys. Lett. B475 (2000) 386]**,
A. Airapetian et al., Phys. Lett. **B567** (2003) 339

16. **Double–spin asymmetries in the cross section of $\rho^0$ and $\phi$ production at intermediate energies**,
A. Airapetian et al., Eur. Phys. J. **C29** (2003) 171

17. **Measurement and microscopic analysis of the $^{11}$B($\vec{p}$, $\vec{p}$) reaction at $E_p$ = 150 MeV. I. Inelastic scattering**,
V.M. Hannen et al., Phys. Rev. **C67** (2003) 054320

18. **Measurement and microscopic analysis of the $^{11}$B($\vec{p}$, $\vec{p}$) reaction at $E_p$ = 150 MeV. II. Depolarization in elastic scattering from odd–A nuclei**,
V.M. Hannen et al., Phys. Rev. **C67** (2003) 054321

19. **Measurement of Single–spin Azimuthal Asymmetries in Semi–inclusive Electroproduction of Pions and Kaons on a Longitudinally Polarized Deuterium Target**,
A. Airapetian et al., Phys. Lett. **B562** (2003) 182

20. **Quark Fragmentation to $\pi^{\pm}$, $\pi^0$, $K^{\pm}$, $p$ and $\bar{p}$ in the Nuclear Environment**,
A. Airapetian et al., accepted for publication by Phys. Lett. B, hep–ex/0307023

21. **Flavor Decomposition of the Sea Quark Helicity Distributions in the Nucleon from Semi–inclusive Deep–inelastic Scattering**,
A. Airapetian et al., submitted to Phys. Rev. Lett., hep–ex/0307064